JEANINE CLAUDIA PICHLER BSC

COMPARISON OF A SPUTTER PROCESS OF TI- AND AL-THIN FILMS. HOW DOES THE SIMULATION WITH THE SOFTWARE "OPERA" FIT WITH THE EXPERIMENT?

MASTER'S THESIS

TO ACHIEVE THE UNIVERSITY DEGREE OF

DIPLOM-INGENEURIN

SUBMITTED TO

GRAZ UNIVERSITY OF TECHNOLOGY

SUPERVISOR

AO. UNIV.-PROF. DIPL.-ING. DR.TECH KLAUS REICHMANN

INSTITUTE FOR CHEMISTRY AND TECHNOLOGY OF MATERIALS

SECOND SUPERVISOR

PRIV. DOZ. MAG. DR. REINHARD KAINDL

JOANNEUM RESEARCH MATERIALS

GRAZ, DEC.2014

AFFIDAVIT

I declare that I have authored this thesis independently, that I have not used other than the declared sources/resources, and that I have explicitly indicated all material which has been quoted either literally or by content from the sources used. The text document uploaded to TUGRAZ online is identical to the present master's thesis dissertation.

Date Signature

1 Abstract

Keywords: Magnetron sputtering, Ti- and Al- thin films, TOSCA, SCALA, thickness distribution, "Opera" simulation

In the last few years, magnetron sputtering has become a very important industrial process for coatings. These coatings can be hard, wear-resistant, corrosion resistant, or low friction coatings. Coatings with specific electrical and optical properties are also possible. The purpose of this master's thesis was to investigate a magnetron sputter process for the deposition of Ti- and Al- films in reality and to simulate the process with the Software "Opera". To compare the results of the simulation and the experiment, parameters like the magnetic flux density and the thickness distribution on the substrate have been calculated and measured. The results of this thesis show that the magnetic measurements are comparable with the simulations. The thickness distribution differs between simulation and experiment by a factor of 2. Therefore, at this time it is not possible to confirm that the simulated sputter process is comparable with the real experiment.

2 Content

3 Introduction

Thin films in the range of a few nanometers to a few micrometers on metals, alloys and polymers can improve the properties of a certain device. In the last years the thin film deposition was getting more and more important in science and technology. (1) The reason for this development is that many properties of a large device can be improved by depositing a thin film of another material on it. It is possible to deposit metal thin films, resistant thin films (nitride, oxide, carbide), diamond like carbon thin films and films similar to graphene. Those thin films are important for metals, alloys, polymers and composite materials to gain better resistance, hardening, less corrosion, bio-compatibility, electrical properties and tribological qualities.

There are different vapor deposition techniques to deposit thin films onto various substrates. To deposit such materials, knowledge about the process itself is very important. Many of the vapor deposition techniques are assisted by plasma. Therefore, the generation and control of plasma is very essential. Plasma assisted processes have been known for a long time. The first sputtered thin film was deposited more than 100 years ago. One of the first patents for plasma assisted gold sputtering was filed by Thomas Edison in 1902. (2)

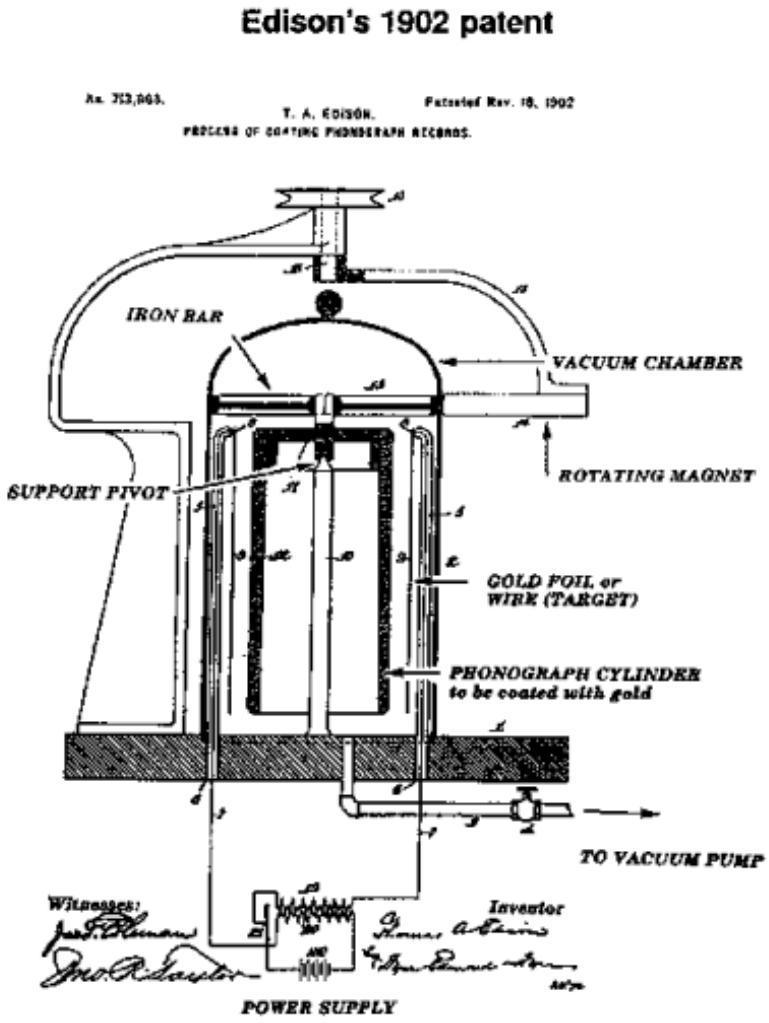

Figure 1: Edison's 1902 patent of a plasma assisted gold sputtering apparatus (2)

This application in Figure 1 shows how a thin gold film is sputtered on a phonograph cylinder made out of wax. The main parts of this apparatus are the same as nowadays, a vacuum chamber, target, substrate and a source which produces an electrical discharge. The target in this case is a gold wire or gold foil strip. The master cylinder is suspended on a pivot and is rotating with the help of magnets to gain uniformity of the coating. The target sputters a thin gold film on the outer surface of the cylinder in the presence of plasma. After the sputtering process the wax cylinder gets electroplated to form a master mold from which cylindrical phonograph records were made. This method was used for almost 20 years, but then the requirements like the dimension and thickness of the tools changed and this method could not

achieve them anymore. However, it was the forerunner of the compact disc which is covered by sputtered aluminum thin films. (2) Plasma assisted sputter processes have been researched and developed since then. One of the methods used nowadays is magnetron sputtering. Principals and applications of this method have been researched a lot in the last decade and therefore, became a very important industrial process for hard coatings. The driving force in this case is the demand of high-quality functional films and thicker magnetron sputtered films with the same functionality. (1) The fundamentals of the process have been known for a long time, but are still not fully understood. In the 1970s the modification of the magnetic field "balanced magnetron" was introduced to overcome some limitations of the sputtering process. (3) (4) The next steps were the introducing of unbalanced magnetrons during the 1980s and finally the closed field systems in the early 1990s. (5) (6) (7) (8) The terms "balanced and unbalanced magnetrons" indicate the use of the variation of the magnetic field to enhance the sputtering yield. The closed field systems improved the quality of the film. The deposition rates increased, the film had a better adhesion and could be deposited on a wide range of materials. The next step after introducing all those new technologies was the pulsed magnetron sputtering. (9) In these entire physical vapor depositing techniques the ion bombardment is the critical factor which influences structure and properties of the growing film. (10) (11)

In this master's thesis magnetron sputtering was used to deposit Al- and Ti- thin films which were characterized afterwards with respect to physical dimensions. The aim of this thesis is the comparison of deposition of Al- and Ti-thin films, calculated by the program "Opera", with deposition experiments in the lab site of JOANNEUM RESEARCH - MATERIALS. To understand the background of the magnetron sputter process, some theoretical concepts will be discussed. These topics include the plasma process itself, generation of the plasma process, different vapor deposition techniques and an introduction into finite element analysis. The methods used to investigate and to compare the simulation of a plasma process with the experiment are described in the experimental part of this thesis. The last part of this thesis compares the magnetic flux densities and the film thickness distribution of the simulation with the experiment.

4 Theoretical background

4.1 Gas Phase Deposition Processes

There are many different deposition processes from vapor phase. They can be divided into two main groups: Chemical Vapor Deposition (CVD) and Physical Vapor Deposition (PVD) (12) (13). The later one is going to be the topic in following chapters.

The term Thermal Chemical Vapor Deposition describes the deposition of atoms or molecules by high temperature reduction or decomposition of precursor species. It is also possible that the evaporated material is reacting with a gaseous species like nitrogen, oxygen etc. and produces oxides and nitrides. There are different kinds of CVD, e.g. the Low Pressure CVD (LPCVD) with pressure below ambient, and Vapor Phase Epitaxy, where single crystal films are deposited. It is also possible to combine the CVD process with plasma, which is used to activate and decompose the precursor species and the polarization of polymers. The plasma is mostly generated from radio frequency techniques. Another possibility to classify CVD is to differ between processes for compounds and pure metals. For metals the standard and the Thermal CVD process can be used. For compounds, Plasma-assisted, Radio Frequency Excitation, Microwave and Photon Excitation are applied (14) (15).

Physical Vapor Deposition can be divided into two main categories: evaporation and sputtering, referring to the mechanism of the condensed species in the vapor phase. This will be discussed later on.

Table 1: Characteristics of basic PVD and CVD Processes (15)

	Evaporation	Sputtering	Chemical Vapor Deposition
Mechanisms of production of depositing species	thermal Energy	momentum transfer	chemical reaction
Deposition rate	can be very high (up to 750000 Å/min)	low except for pure metals	moderate (200-2500 Å/min)
Depositing species	atoms and ions	atoms and ions	atoms and ions
Throwing power	poor line-of-sight coverage except gas scattering	good, but non-uniform thickness distribution	good
Metal deposition	Yes	Yes	Yes
Alloy Deposition	Yes	Yes	Yes
Refractory compound deposition	Yes	Yes	Yes
Energy of deposited species	Low (0.1-0.5eV)	can be high (1-100eV)	can be high with plasma-aided CVD
Bombardement of substrate/deposit	Not normally	Yes	possible
Growth interface pertubation	Not normally	Yes	Yes (by rubbing)
Substrate heating (by external means)	Yes, normally	not generally	Yes

Table 1 shows some characteristics of the basic PVD and CVD processes. With both processes it is possible to deposit metals, alloys or even refractory compounds. The energy of the deposited species differs from 0.1 eV with evaporation to 100 eV with sputtering or plasma-aided CVD. The deposited species for most PVD and CVD processes are dominantly atoms, only in High Power Impulse Magnetron Sputtering (HIPIMS) ions play a major role. The

deposition rate varies also widely depending on the process and chemical properties. This thesis mainly deals with the physical vapor deposition.

4.1.1 PVD processes

First of all there are three main steps to understand various vapor deposition processes: (15) (16) (17)

- Step 1: Creation of the vapor phase species
- Step 2: Transport from source to substrate
- Step 3: Film growth on the substrate

In Step 1 there are various possibilities. The material can be transferred into the vapor phase by sputtering, laser ablation, evaporation, gases etc. In Step 2 the species are transported from the source to the substrate, forced by collisions between atoms and molecules. It is also possible that the species get ionized by plasma in this space. In Step 3 the nucleation and growth on the substrate begins and can be influenced by the bombardment of the ionic species. Ions and neutrals cause some effects during these film formations. On the one hand the condensed species are thermally and chemically activated and the impurity atoms are desorbed, and on the other hand impurity atoms or deposited film species are implanted. These three steps occur during all physical and chemical vapor depositions. A process is mostly flexible when all three steps can be controlled independently. This flexibility leads to controllable properties, structure and deposition rate.

Physical vapor deposition can be divided into two main categories: sputtering and evaporation. Both terms describe the mechanism of the condensed species in the vapor phase. The bombardment of the growing film by energetic species from adjacent plasma is very important for the process. Therefore, the generation of the plasma and the ion energies play a major role. For this task the main focus lies on the sputtering process. In the following some background knowledge about the plasma itself, the sputtering process and the particle reactions that occur are discussed. A classification of PVD processes, according to generation of the vapor species in the presence of or without plasma and bias, is given by (18):

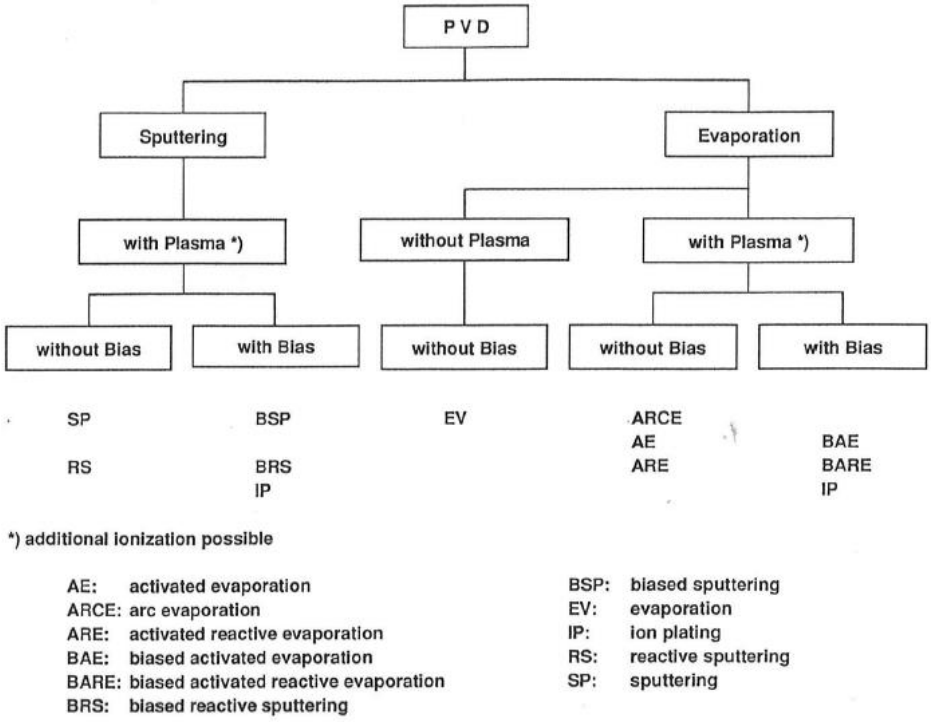

Figure 2: Classification of PVD Processes (18)

The target is made of a solid material in different shapes, depending on the used cathode. There are different evaporation processes to transform the target material into the vapor phase. Some of them are arc-, activated-, and biased evaporation as shown in Figure 2. The second way is to deliver kinetic energy which is also called sputtering. One of the big differences between evaporation and sputtering is the energy of the condensed particles, which is around 1 eV for the former one and 5-50 eV for the latter. Another difference is the low pressure necessary for plasma generation in sputtering whereas for evaporation it is not necessary. It is also possible to predetermine a bias voltage between the wall of the recipient (vacuum chamber) and the substrate. In this case the negative bias voltage is used to accelerate the positive ions into the direction of the substrate. (19) With this procedure it is possible to influence the structure, durability, adhesion and purity of the deposited film. (20) (21)

During sputtering, a momentum transfer from an incident particle to the target results in the ejection of surface atoms or molecules. These atoms or molecules are accelerated into the direction of the substrate and begin to grow a thin film. The pressure during these processes ranges from 20 to 150 mtorr. The relation between target erosion R and the sputtering yield S is called target erosion rate and is given by: (15)

$$R = 62.3\frac{JSM_A}{\varrho} = \ [\frac{\text{Å}}{min}]$$

J…ion current density [mA/cm²]

S…sputtering yield

MA…atomic weight [g]

ϱ…[g/cm³]

The sputtering yield S for assuming ion incidence onto a target consisting, of a random array of atoms, is given by: (15)

$S = constant * \frac{M_i M_t E_i}{(M_i + M_t)U}$ = [atom/ion]

Mi…mass of incident atom

Mt…mass of target atom

Ei…kinetic energy of the incident ion

U…heat of sublimation of the target material

With these two formulas the sputter target erosion rate and the sputtering yield can be determined. The problem in a real coating plant is that for the calculation of these values the plasma has to be investigated. Plasma generation is described in the next part.

Table 2: Sputtering yield and deposition rate of various metals relative to copper in an argon plasma (2)

target material	500eV Ar+ sputtering yield	DC plasma magnetron deposition rate
Copper	1	1
Aluminum	0,45	0,52
Titanium	0,22	0,27

Table 2 shows the sputtering yield and the deposition rate for aluminum and titanium relative to copper, bombarded with Ar^+ ions accelerated to 500 eV and compared to a direct current magnetron deposition. It shows that the sputtering yield and the deposition rate of aluminum are twice as high as of titanium. This means that it is easier to eject an aluminum atom from the surface than a titanium atom. A sputtered thin film of Al at 2-10 mtorr and 500 V normally has a polycrystalline fcc structure whereas a sputtered Ti or $TiAl_3$ film under the same conditions has a hcp structure. The TiAl thin film under the same conditions shows a nanocrystalline structure, but this structure is only visible if the thin film has a range of thickness of 8000-1000 Å. (22)

In this work magnetron sputtering was used for the deposition of thin films. Another important factor influencing the deposition is the magnetic field of the magnetron cathode. For the process of thin film deposition the generation and understanding of the assisting plasma is very important.

4.1.2 Generation of the plasma

Plasma is an energetic environment in which a lot of chemical processes can occur. Mostly these processes are caused by electron-atom collisions. To form stable plasma, electrons are accelerated in an electric field. There are three different sources of electrons: (14)

- Ionizing collision where an atom loses an electron
- Electrons from a hot thermoelectron emitting source
- Secondary electrons from an ion or electron bombarded surface

Plasma is a quasi-neutral mixture with electrons, ions and neutral particles which interact with each other. Normally low pressure plasmas < 100 Pa are used for deposition techniques. In order to generate such low pressure plasma it is necessary to ionize gaseous species of a vapor by a glow discharge. The glow discharge is triggered via external energy sources, which can deliver up to 30 kW and frequencies from 50 Hz (direct current, d. c.) over 5-10 kHz (pulsed d. c.) to radio and microwave frequency (MHz-GHz). (19) There are different methods for coupling such a power supply to a vacuum chamber which operates with argon in a pressure between 0.01-100 Pa. Figure 3 shows some examples.

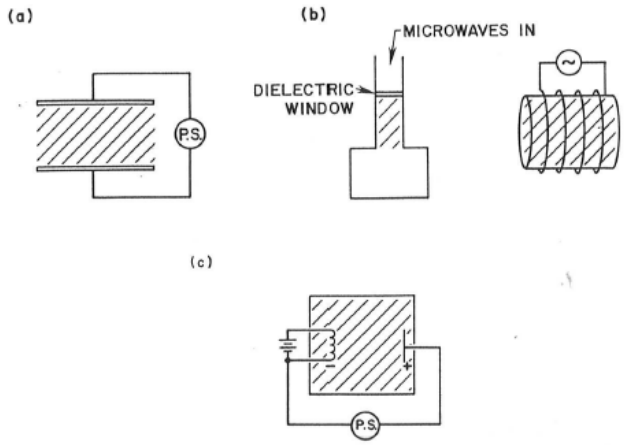

Figure 3: Methods for plasma generation for low pressure deposition techniques: a) plasma excitation of a diode-array with cold electrodes b) plasma excitation with an electric or electromagnetic field coupled with an specified window into the non-conductive recipient wall c) plasma excitation from an thermal electrode and accelerated electrons because of an electric field (23)

The first method shown in Figure 3 a) is used in direct current and radio frequency mode for magnetron and plasma etch processes. The electrons in this method are generated by ion bombing of the cold and negatively charged cathode. The same electron generation is used during magnetron sputtering. In the second method b) the electrons are accelerated in the plasma itself and the generation of free electrons is caused by ionization. In method c) the electrons are generated by a thermal electrode and are accelerated in the direction of the anode. For this thesis the relevant method is the first one, because it is also used in magnetron sputtering.

The magnetron itself serves as cathode with a target material. The cathode is negatively charged and above the cathode the magnetic field traps electrons and increases efficiency of the process. For the generation of a magnetic field permanent magnet alloys like NdFeB, Al-Ni-Co and Co-

Sm are used, which have a magnetic field strength B in the range of $2*10^{\wedge-2}$ to $5*10^{\wedge-2}$ Tesla. (24) The cathode itself consists of three main parts, the permanent magnets, the target which is cooled by water and the dark current shielding. There are several different magnetron setups like cylindrical or planar.

In the case of magnetron sputtering the magnetron enhances the sputtering process and matches the cold cathode diode setup. The magnetic field of the magnetron can be divided into two main categories, balanced and unbalanced, as shown in Figure 4.

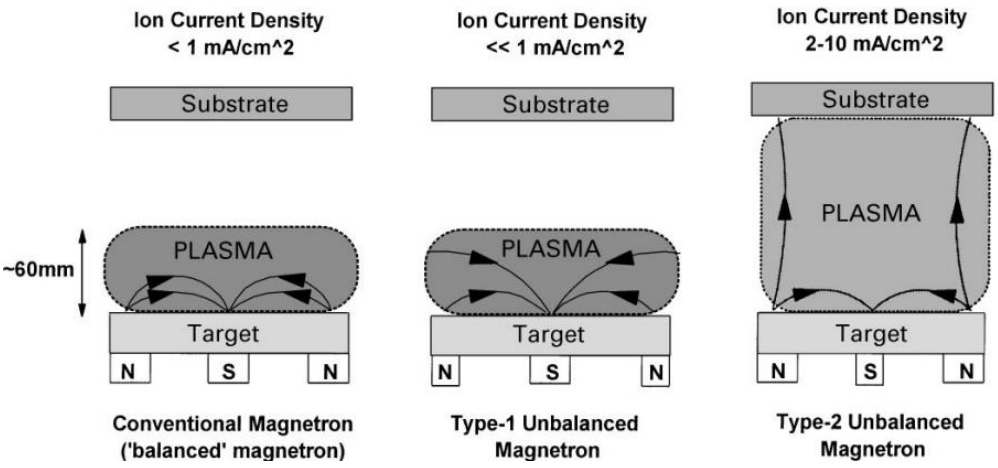

Figure 4: Balanced and unbalanced magnetic field configurations of magnetrons.

In a balanced magnetron the magnetic field lines are closed between the inner and outer magnets whereas in unbalanced configuration the lines are partly opened in the direction of the substrate. This causes the plasma to expand towards the substrate.

Ionization of inert gas species happens because of collisions. The substrate is charged with a negatively bias-voltage. The film quality can be enhanced due bias-voltage and the magnetic field. (25) The magnetic field is a very important part of the magnetron sputtering process. Depending upon the type of the magnetron cathode it can be fixed or in larger cathodes it can be manipulated by changing the number and strength of permanent magnets. Some models even allow field manipulation by manual or motor-driven distance changes of the magnets. So the strength of the magnetic field should be the same during the sputtering. There are some important definitions for the magnetic field: hysteresis and ferromagnetism. The physical mechanism of a material forming a permanent magnetic field is called ferromagnetism. It is a material property, not only caused by the chemical composition but also by the crystal structure.

Magnetic hysteresis occurs when an external magnetic field is applied to a ferromagnetic material. The dipoles in the material align depending on the external magnetic field. After removing the magnetic field the material is still magnetized.

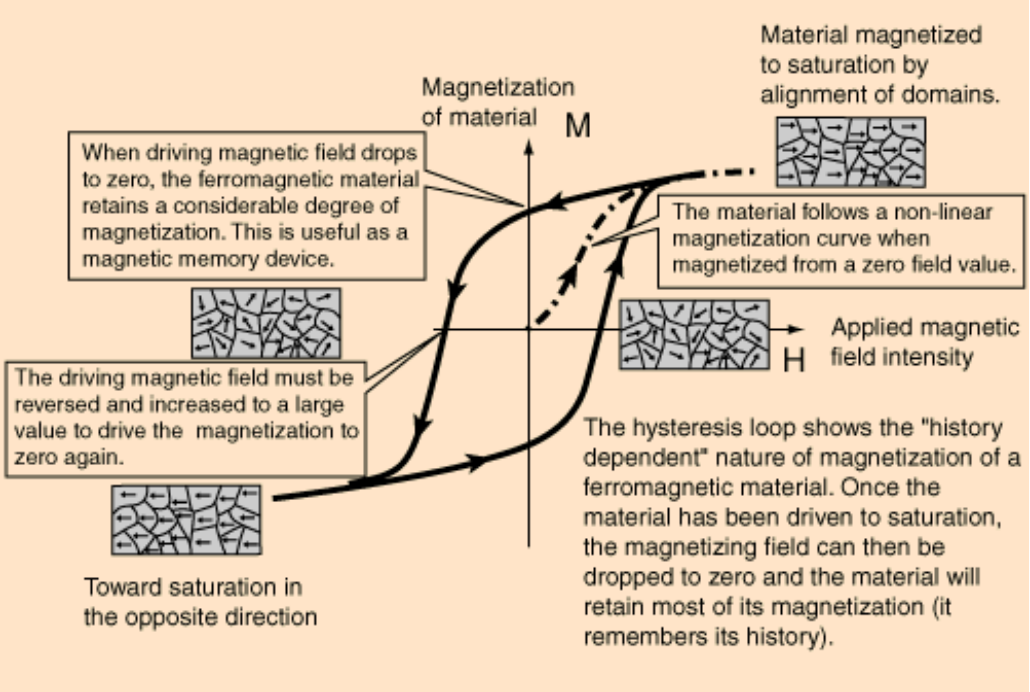

Figure 5: Hysteresis Loop of a magnetized material (26)

Figure 5 shows the hysteresis loop of a magnetized material. A ferromagnetic material is magnetized by an external field in one direction, after removing the field the material does not relax to zero. When an alternative magnetic field is applied on the material it follows the hysteresis loop. After the material is magnetized to saturation, the domains have a magnetic memory and it will not relax to zero. The ferromagnetic material becomes a permanent magnet which can be used in a magnetron cathode. During this process the magnetic flux density B or M and the magnetic field strength H are monitored, which is then plotted in a so called B/H curve. This B/H curve is a very important property of the permanent magnet and it is necessary for calculations and simulations of the magnetic field, and strongly influences thin film properties. The characterization and variation of these properties is the topic of the next chapter.

4.1.3 Characterization of thin films

Thin films have totally different properties than thick films or bulk materials. In the last decade a new sidekick of science became more and more important, the nanotechnology. The prefix "nano" stems from the Greek word "nanos" for dwarf and denotes 10^{-9}. The main reason behind this development is that a material shows different properties in the macroscopic state or as a thin film which is only a few nanometers thick. So the properties change with the scaling of the particles. This was an important finding that opened a new market for thin films. There are many important characteristics of thin films which include composition, thickness, density, electrical resistivity, magnetic properties, internal stress and emissivity of the film. For sputtered films also the morphology, film density, corrosion resistance, adhesion and film density are important. The definition for the boundary between thin and thick film varies in literature. In this thesis a thin film is defined to be thinner than 10µm. Thin films for microelectronics are between 0.2 µm and 10 µm thick. Different factors influence the morphology of a thin film, including the topography, coverage and crystallography. High quality thin films should have a constant thickness, uniformity and no defects. The composition of thin films is highly variable depending upon the target materials. Extensive knowledge is necessary in order to get a thin film with all required properties on a substrate. (2)

The properties of a thin film depend on the application. For the fabrication of microelectronic chips electrical conductivity is important whereas for applications in cars and architecture reflective and antireflective might be required. Optical and magnetic properties are key factors for recording media applications. Other applications are protection of tools against abrasion and corrosion or for biomedical products where the body should not interact with the used material. Thin films are also used for the food industry, for example the oxygen barrier coating in a Tetra Pak. There are many other applications of thin films; in most cases the requirements are very high. It is therefore important to investigate and to optimize the deposition procedures.

4.2 Finite Element Analysis

The finite element analysis (FEM) is a numerical method to find approximate solution for partial-differential equations. Many different commercial software suites were developed since the 1980s. The first FEM-software was MANI, developed by Nicolae Marinescu in the 1980s.

(27) After that various softwares came on the market, including "Opera" which was used within this thesis (Cobham plc., sold by Thomatronik GmbH).

4.2.1 What's the idea?

The main idea behind the finite element analysis is that for some equations a correct mathematical solution cannot be found. So, therefore, a numerical method was developed to approximately solve these problems. To get a solution of the partial-differential equations, a model consisting of a triangles mesh is created, generating a finite number of points to be solved. (27)

For this thesis only some parts of the Sofware package "Opera" were used. These two parts are the magnetostatic solver TOSCA which is able to model magnetic fields and to calculate the magnetic flux density and field intensity B and H. To simulate a sputter process the solver SCALA is used for calculation of particle orbits, particle distribution and target erosion, using the calculated magnetic field from TOSCA as an input parameter.

4.2.2 Magnetostatic solver (Tosca) and space charge

For an approximate solution a model has to be built and some parameters have to be set. During these steps the model will be reduced.

The different models are:

- Physical Model: real measurements, specification, geometry, materials (steel, copper, silicon, air etc.)
- Electromagnetic Model: the physical model will be reduced to its electromagnetically active parts
- Mathematical Model: symmetry, governing equations, boundary conditions
- Numerical Model: discretization (Finite Element Method)
- Algebraic Model: solve matrix equation to obtain potentials

In the magnetostatic solver TOSCA the conditions applied for the potential are shown in Table 3.

Table 3: The two potential applied for the solution of the magnetic field (28)

No Source Currents $I_s=0$	Biot-Savart Conductors (Source Currents) exist $I_s\neq0$
$\mu\geq1$ (iron regions)	$\mu=1$ (free space)
ψ	ϕ
Total (Scalar)	Reduced (Scalar)

There are some important definitions for the solution of a magnetostatic problem. These are:

The total electric scalar potential V, which is used for TOSCA and SCALA, is defined by: (28)

$$E = -\nabla V$$

The total magnetic scalar potential φ (TOSCA) is given by: (28)

$$H = -\nabla\varphi$$

The value of H must be set for magnetic materials like permanent magnets. For the regions where source currents like coils exist, another formula for H is used: (28)

$$H = -\nabla\varphi + H_s$$

To calculate the electrostatic fields in SCALA the Poisson equation has to be solved: (28)

$$\nabla * \varepsilon\nabla V(x,y,z) = -\rho(x,y,z)$$

- Initially solved with $\rho(x,y,z) = 0$

Other important background equations:

-current in particle track: (28)

$$I_{track} = J_0\delta A$$

J_0...current density at emitter surface

δA...area of emitter represented by track

The emitter settings of SCALA depend on the used emitter type. A large variety of equations, stored in a databank, is available (29)

In this thesis the magnetostatic calculation was done first and after that included into the approximate solution of the space charge calculations, from which film deposition distribution, particle tracks and many other properties can be derived.

5 Experimental

5.1 General

For the experiments and simulations a number of devices were used, which are described in the following.

For magnetic measurements two Gaussmeter were compared, in order to verify that the results are correct. For the measurements at Joanneum Research the Gaussmeter GM08 from the company HIRST Magnetic Instruments Ltd. was used.

Figure 6: Gaussmeter GM 08 for 3D scanning and direct measurements

Figure 6 shows the Gaussmeter GM08. For all measurements with the Gaussmeter GM08 the DC mode was used. The accuracy of the equipment is better than ±1% and the reproducibility is better than 0.5%, as given by the manufacturer.

For comparison of the result the same measurements were repeated at the Montanuniversität Leoben with the Gaussmeter 410 which is shown in Figure 7 (LakeShore Measurement and Control Technologies)

Figure 7: Gaussmeter 410 from the company LakeShore

In the further chapters the abbreviations GM08 and GM410 are used.

The deposition processes have been carried out in the laboratories of JOANNEUM RESEARCH – MATERIALS in Niklasdorf. The deposition plant is a strongly modified PL-600 (Pfeiffer Wien) .

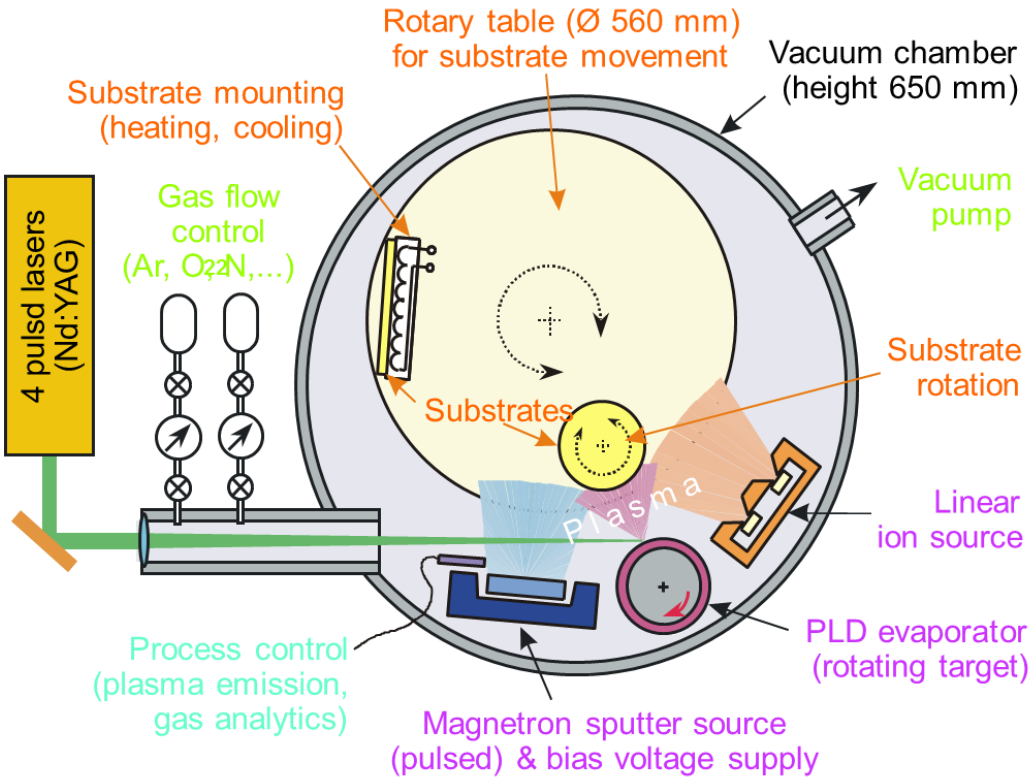

Figure 8: PL 600 schematic setup

Figure 8 shows the schematic setup of the sputter-construction. The main parts of this site are a vacuum chamber and a vacuum pumping system, the gas supply, the target, the substrate holder, the linear anode layer source (ALS) and the magnetron sputter source. For this experiment a Torus 2" cathode, produced by the company Kurt J. Lesker, was used. The experiments were performed by a technical employee of JOANNEUM RESEARCH.

For the film thickness and the thickness distribution measurements across 3" silicon wafer a Profilometer Dektak 150 from the company Vecco was used. The software for evaluation of the normal and the 3D scans was Dektak and Dektak Visions.

A Leitz Aristomet, Type: 020-504.030 microscope was used to acquire pictures at 2.5x, 5x, 10x and 20x magnification.

5.2 Description of Hardware components

5.2.1 Setup

In this chapter the setup of the permanent magnets and the cathode in the PL-600 is discussed as well as the important material parts.

5.2.1.1 Magnets

To compare the simulation with the experimental data of the magnetic flux density B on the cathode, only the magnets on the ferromagnetic steel plate were investigated.

A simplified input model for the TOSCA solver consists of a steel plate, two cylindrical permanent magnets in the middle, surrounded by 16 permanent magnets (2 on top of each other) in a circle. The used material information is further described in the chapter *Material properties*.

Figure 9: Configuration of permanent magnets on a ferromagnetic steel plate in the cathode.

As shown in Figure 9, the permanent magnets are mounted together with glue. The inner magnets are round and the outer magnets are building blocks. The outer magnets have the physical dimensions of 0.5 x 0.5 x 0.5 cm. The inner magnets have a diameter of 1.9 cm and a height of 0.4 cm. All permanent magnets are made of the same material, Neodymium-Iron-Boron or abbreviated NdFeB or N45M.

5.2.2 Cathode

First of all the real dimensions of the cathode were measured with a caliper and pictures were taken.

Figure 10: Torus 2" cathode

Figure 11: Disassembled Torus 2" cathode

In Figure 10 and Figure 11 the whole cathode, assembled and disassembled, is shown, respectively.

5.2.2.1 Material properties

All main parts of the cathode are made of stainless steel 304L. For the copper plate Alloy 101 and for the steel plate, where the permanent magnets are fixed, stainless steel 416 was used. The Nd-Fe-B permanent magnets are named N45M in the database.

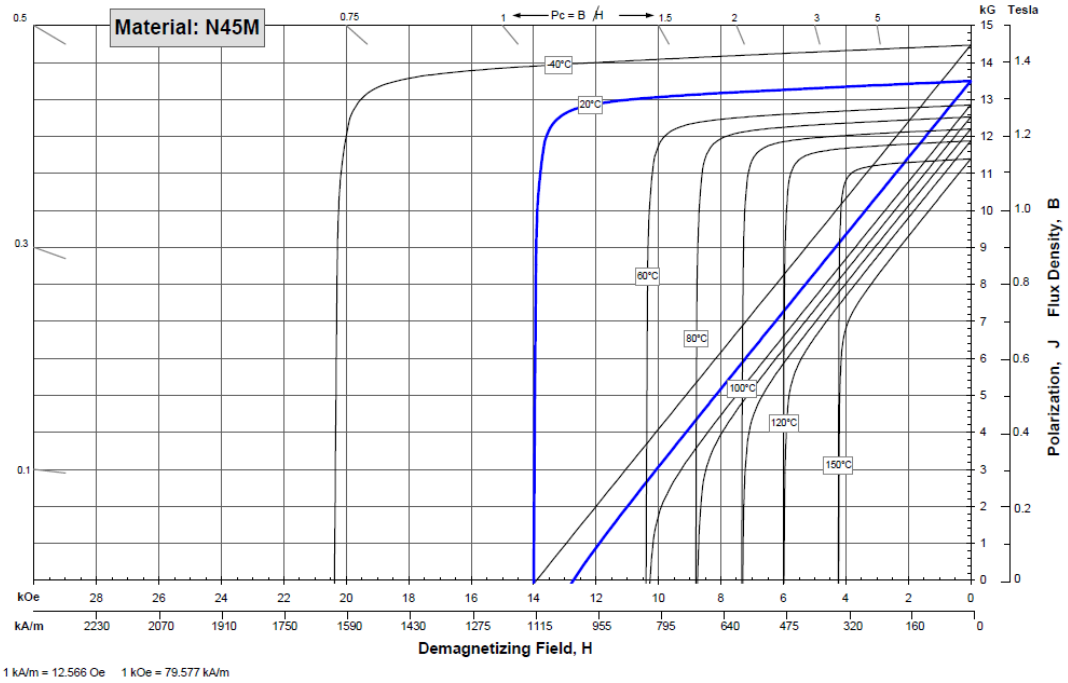

Figure 12: Demagnetization curve of N45M permanent magnets

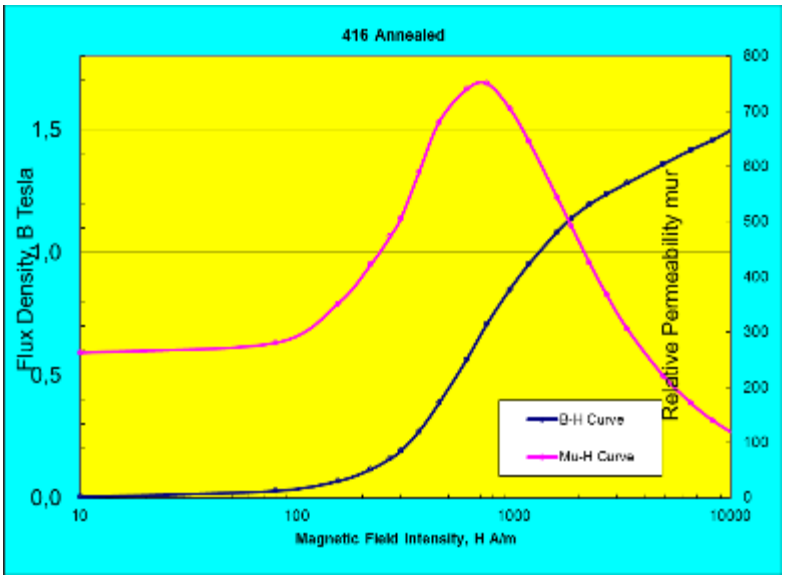

Figure 13: B/H curve of the annealed stainless steel 416

Figure 12 and Figure 13 show the magnetic data for the permanent magnets and the ferromagnetic steel plate.

5.2.3 Process parameter

In total 11 deposition experiments in the coating plant were performed. Pure titanium and aluminum 2" discs with a thickness of 0.65 cm were used as targets. The considered parameters for the sputter process in this work are:

- Gas flow of argon in [sccm]
- Power in [W]
- Relative target-substrate distance [cm]
- Negative Bias Voltage [V]

The ALS etching is a cleaning and activation process of the substrate surface prior to deposition (Table 4).During the process the exact voltage, current and pressure is recorded. Table 5 shows the defined sputter parameters.

Table 4: Parameter for ALS etching for substrate cleaning and activation prior to sputter deposition

ALS etching			
[V]	[sccm]	VAT	[min..]
1000	20 Ar	750	0,5
1000	20 Ar	750	0,5

Table 5: Overview of the deposition parameter of sputter experiments

run No.	film	power [W]	gas flow [sccm]	relative target-substrate distance [cm]	Bias Voltage [V]
B343_4	pre-exp.Ti	200	60 Ar	5	-60
B343_5	Ti	200	60 Ar	5	-60
B343_6	Ti	200	60 Ar	7	-60
B343_7	Ti	300	60 Ar	5	-60
B343_8	pre-exp. Al	200	70 Ar	5	-60
B343_9	Al	200	70 Ar	5	-60
B343_10	Ti	200	70 Ar	5	-60
B343_11	Ti	200	90 Ar	5	-60

In order to evaluate the influence of different deposition parameters, the power was increased from 200 W to 300 W. The substrate-target distance was also increased from 5 to 7 cm. To compare aluminum with titanium coatings, two experiments with the same set of parameters were performed (B343_9 and B343_10). The last parameter to be changed was the argon gas-flow (resulting in increased pressure) in experiment B343_10 from 60 sccm to 90 sccm in B343_11.

5.2.4 Measured parameters

5.2.4.1 Measurement of the magnetic field

To compare the simulation with reality, the magnetic field of the permanent magnets was measured. First the permanent magnets on the ferromagnetic steel plate were measured directly. Then an X/B profile across the cathode and after that the 3-dimensional field intensities along point grids in planes at different distances, parallel to the copper plate of the Torus 2"cathode, were measured.

5.2.4.1.1 3D magnetic field intensity

In Figure 14 and Figure 15 the setup for the 3D magnetic field intensity measurements are shown. The first measurement took place on the surface of the copper plate of the Torus 2" cathode. An axial probe head was placed onto a plexiglas plate with 19 times 21 boreholes at a distance of 1 centimeter in the diameter of the hall probe. For the determination of the magnetic flux density B the GM08 Gaussmeter was used.

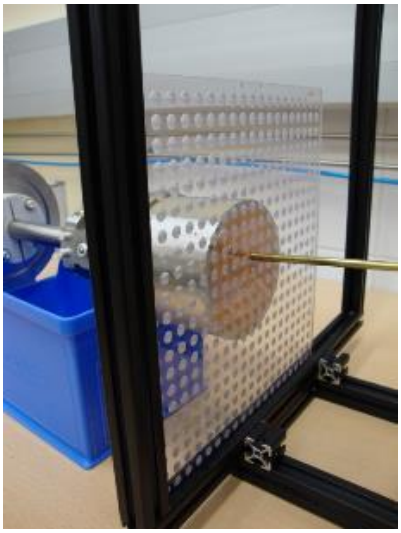

Figure 14: Setup of the 3D magnetic field intensity measurements.

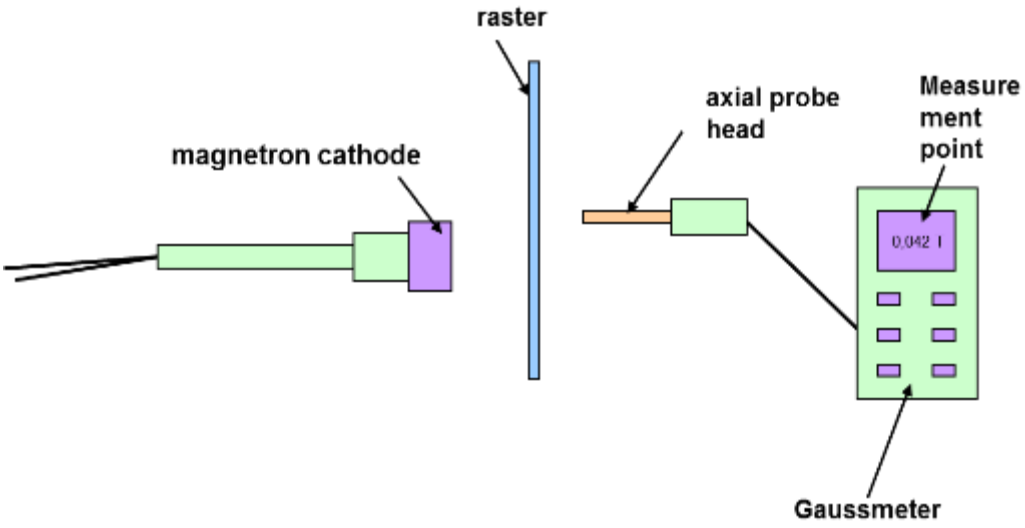

Figure 15: Scheme of magnetic measurement setup

5.2.4.1.2 Direct magnetic measurements

First of all, the inner and the outer magnets of the cathode were measured with the Gaussmeter GM08. The setup is shown in Figure 16.

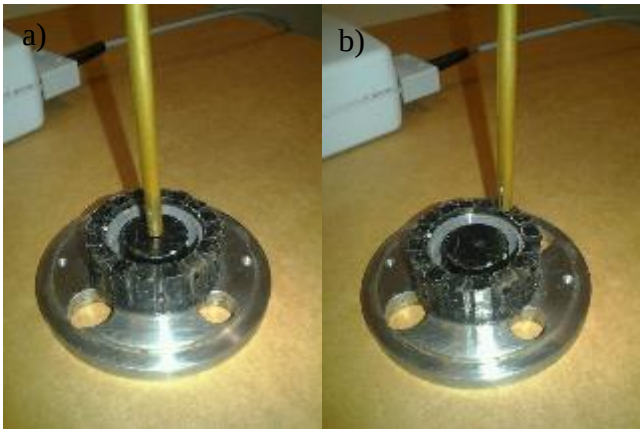

Figure 16: a) Measurement of the inner magnet and b) measurement of the outer magnet with an axial hall-probe head

The second direct measurement of an X/B profile of the flux density B was done by the aim of a ruler, marked with the different measurement points (setup shown in Figure 17). The ruler has a thickness of 0.245 cm and the inner magnets are smaller than the outer ones, resulting in a

distance from the inner magnets to the surface of the ruler of 0.445 cm, which is important for comparison with the simulation data.

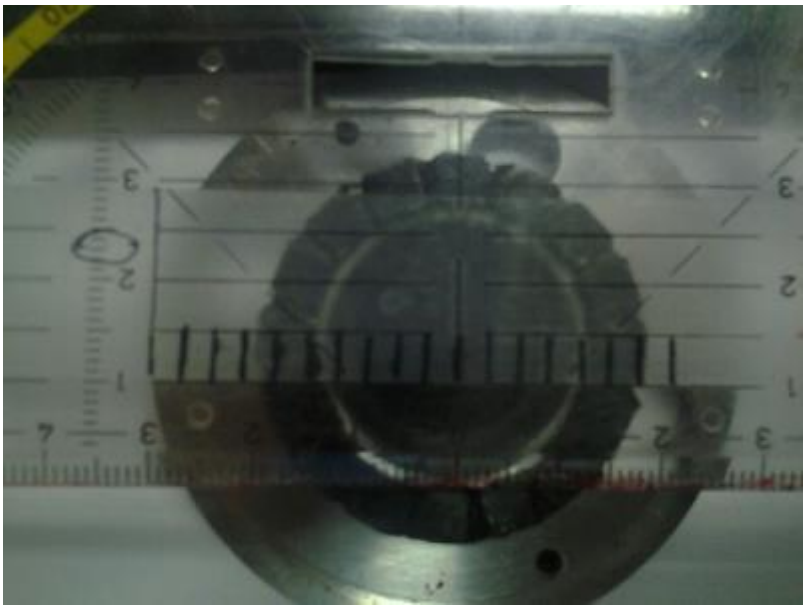

Figure 17: Setup for X/B profile measurements

Along a distance of 5.1 cm every 0.3 cm a measurement was made. The direct measurements were performed with both Gaussmeter GM08 and GM410 for verification of the results.

5.2.4.2 Measurement of thickness

A 3" silicon wafer (100) was used as substrate for the deposition of thin films. The wafer has been masked with Kapton tape to enable measurements of the film thickness on different places over the wafer. Prior to masking, the wafer was cleaned with ethanol and acetone.

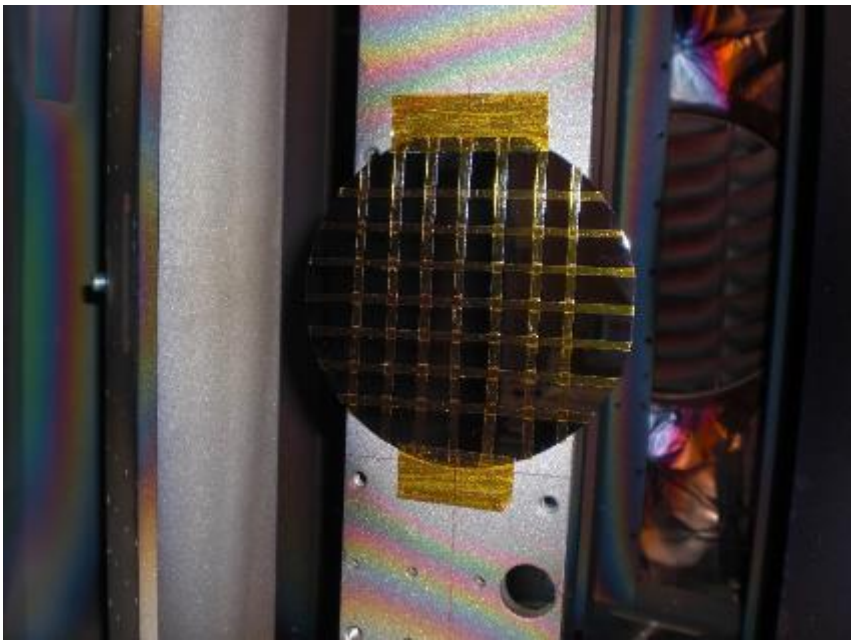

Figure 18: Masking of the substrate prior to thin film deposition

Figure 18 shows how the substrate was masked before the experiment. For the preliminary tests of the Titanium and Aluminum sputter processes only 3 small pieces of the silicon wafer were used.

The thickness along all masked areas, shown in Figure 19, was measured with a profilometer. The film thickness was determined along each profile as shown in Figure 20, and a 3D-model of the surface was generated. Every profile was measured three times to calculate an average value and a standard deviation.

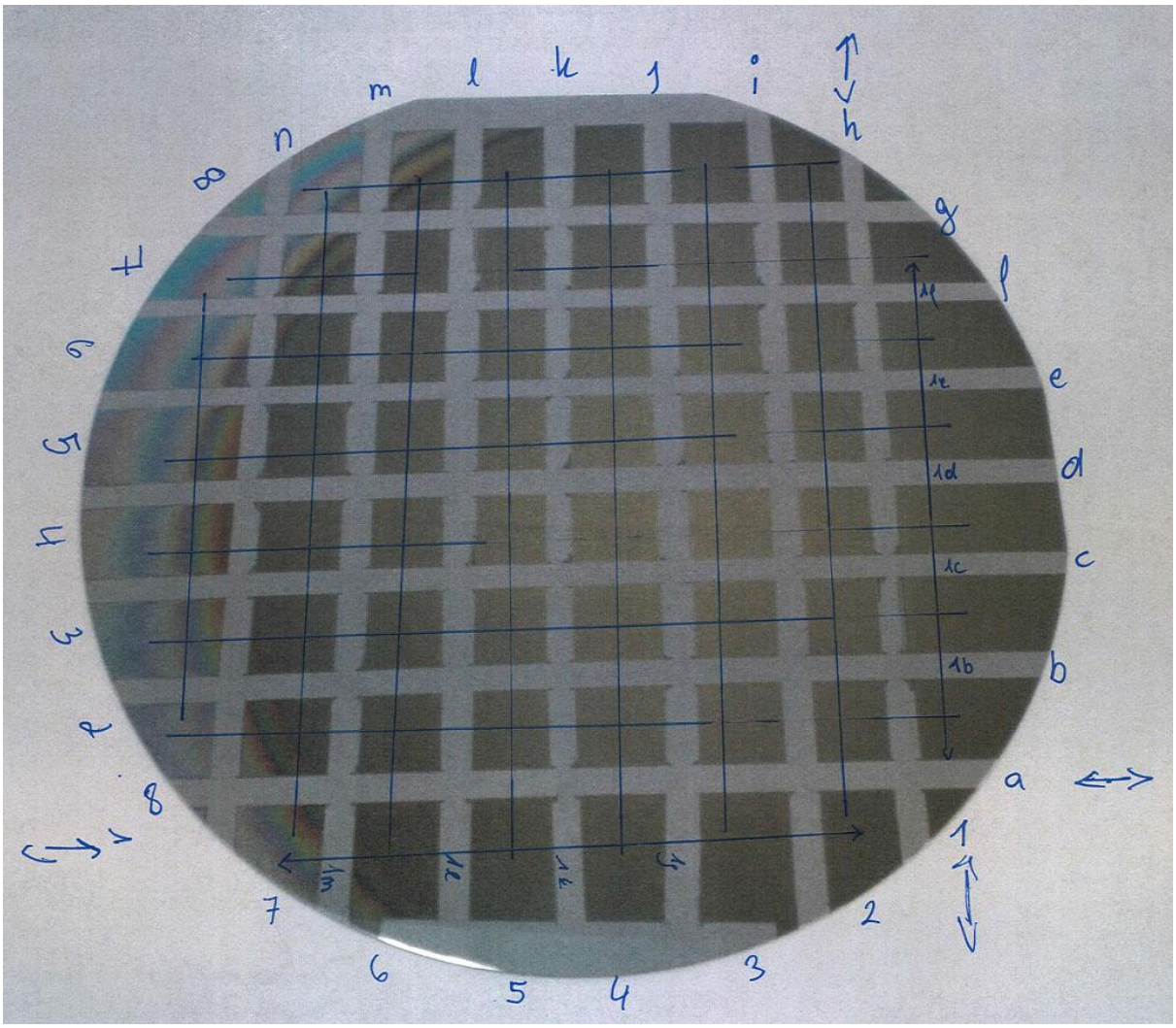

Figure 19: Overview of film thickness measurements of the 3" silicon wafer coated in deposition run B343_2.

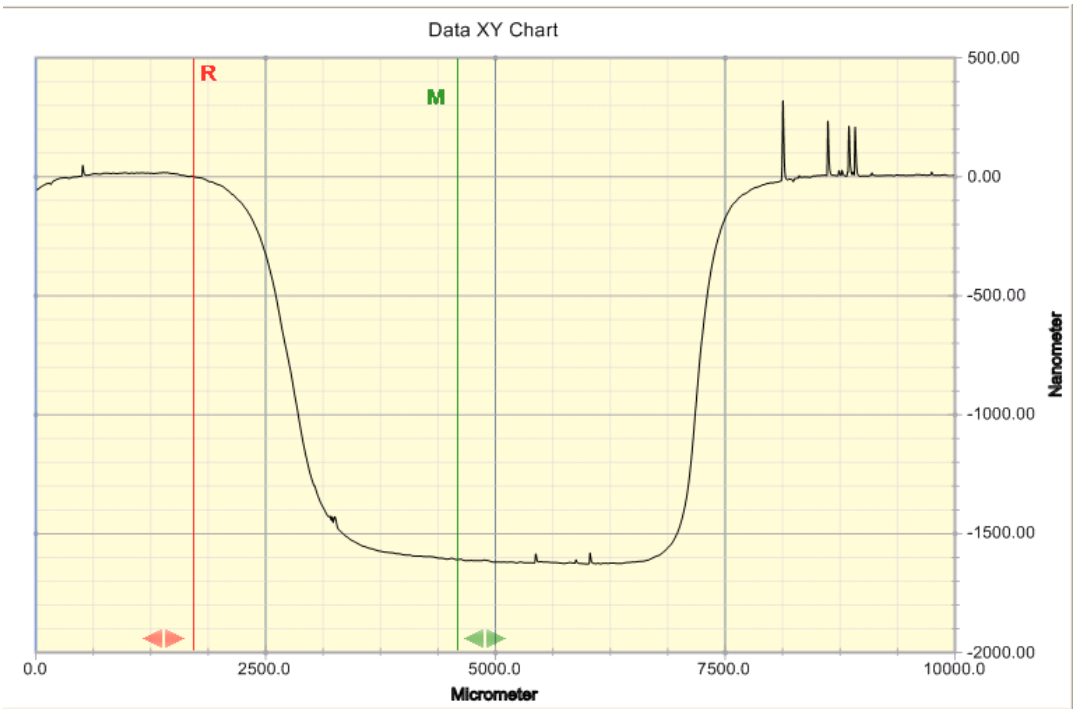

Figure 20: Thickness profile across a masked area in order to determine the film thickness.

In Figure 20 the thickness profile across one masked area is shown. The height difference is measured along the red and the green cursor lines and repeated 3 times for every masked area, in order to get an average film thickness.

The second result, which was obtained from the profilometer, is the 3D mapping. Therefore, the setup to display one thickness profile was to measure 500 times a line profile and the length of it is 6 cm and then get the 3 D map. The results are displayed in the Appendix B.

5.3 Software

For the simulation the Software package "Opera" from Cobham has been used. Included in this software package and used were the solvers TOSCA and SCALA. TOSCA was used for the calculation of the magnetic field and the solver SCALA was used for the particle trajectories. First the dimensions of the real cathode were measured with a caliper and after that the parts which are important for the calculation were included into the modeler of the software. The main focus of the simulation and experimental work was on the Torus 2"cathode. Therefore, this cathode was used to deposit real thin films to compare to the calculated results from the simulation.

5.3.1 Magnetostatic solver (TOSCA)

The magnetostatic solver TOSCA was used to calculate the magnetic field B. The creation of a Computer-aided design (CAD) model was done in the modeler part of the software. After the calculation by the TOSCA solver the solution was analyzed in the post processor of the Opera package. To compare experiment with simulation, the magnetic field along a line and one plane directly at the surface of the cathode was plotted.

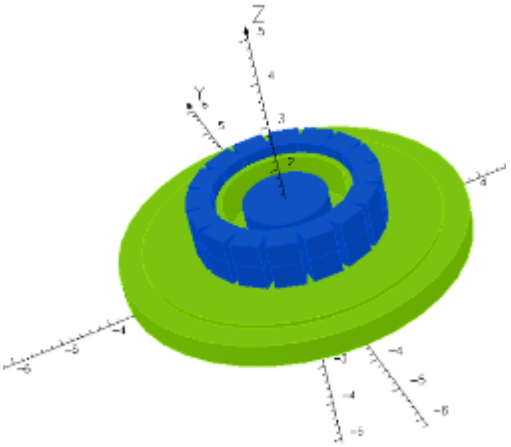

Figure 21: Magnetostatic model of the 2" TORUS magnetron cathode

Figure 21 shows the model of the permanent magnets constructed in the software.

5.3.2 Space charge solver (SCALA)

For the SCALA simulation the copper plate and the steel ring, used for water cooling of the cathode, were not taken into account because these parts do not influence the process.

To create a SCALA model, some physical and process parameters are necessary. For the physical model the parameters depend upon the used materials, which, in this case, were steel, copper, ferromagnetic steel and Neodymium-Iron-Boron. The material data will be discussed later. The dimensions of the cathode are also important for the physical model.

The model for the SCALA simulation is constructed after the magnetostatic simulation with TOSCA, using the existing model of the ferromagnetic steel plate with the NeoFeB magnets as input parameter. In Figure 22 and Figure 23 the labels and the dimensions of the model are shown.

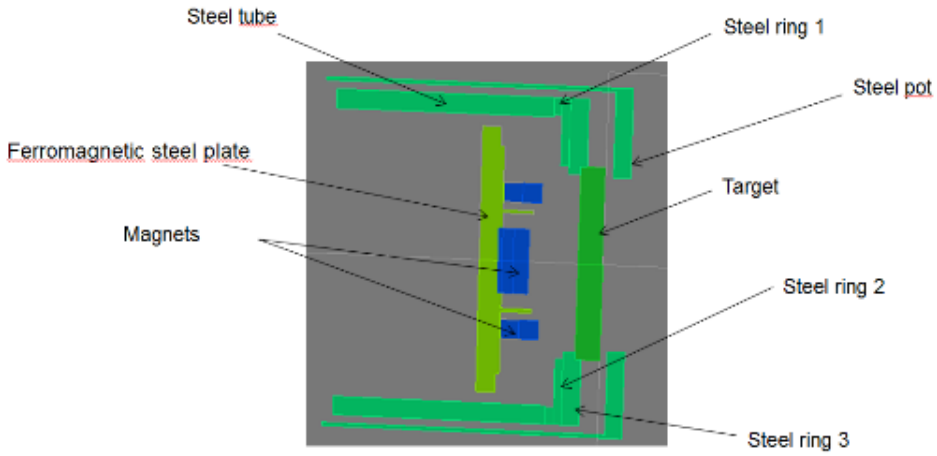

Figure 22: SCALA model of the 2"torus cathode with used labels

In Figure 22 different parts of the SCALA model are shown. This part of the model was identical for every SCALA calculation in this thesis, only the input parameters were changed. As visible in Figure 22, the main part consists of the NeoFeB magnets and the ferromagnetic steel plate, surrounded by different steel tubes or steel rings which keep the target in its place. The steel pot is in contact with the chamber walls and, therefore, on a different potential than the other steel parts. In the following only differences between the steel pot and all the other steel parts inside of it are made.

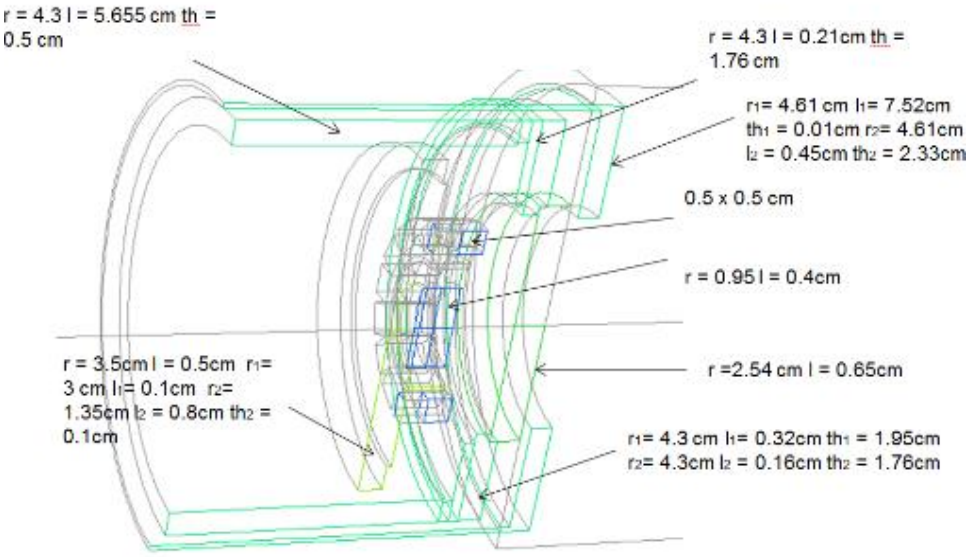

Figure 23: Dimension of the 2"Torus cathode SCALA model

Figure 23 shows the dimension of the different parts of the 2"Torus cathode. The material of the target in each simulation is different but the dimensions remain identical.

5.3.3 Input parameters

The input parameters for TOSCA are:

- Relative permittivity
- Electrical conductivity
- Hysteresis curve for the permanent magnets and the ferromagnetic steel

The relative permittivity and electrical conductivity values are shown in Table 6. Silicon was used as substrate, and aluminum and titanium as targets. For the experiments the electrical conductivity and relative permittivity is only given for the aluminum. The values which are not mentioned in Table 6 were set to the default settings of the program.

Table 6: Material properties used for the simulation of the thin films (30) (31) (32)

Element	atomic weight[u]	ionization energy [eV]	ϱ[g/cm³]	rel. permittivity	electr.conduct. [S/m]
Silicon	28,09	10,36	2,33	11,68	
Aluminum	26,98	5,99	2,70	1,60	3,54E+07
Titanium	47,87	6,82	4,50		

After the material data the different boundary conditions were defined. The potential of the chamber walls and the steel pot were set to 0 V. The target and the inner steel parts were set to variable negative voltages regarding each experiment and the substrate was held constant at a negative bias voltage of -60 V.

To complete the simulation, emitter were defined on the target surface. For the emitter settings many different parameters, like gas type, number of secondary electrons and sputtered particles describing the particle reactions, are needed. For a correct implementation of these plasma functions into Opera a sound knowledge about the plasma is necessary. There are three different emitter types: true secondary emission, plasma emitter and backscattered emission. The parameters, yield, mean energy, number of particles and incident particles have to be defined for the secondary emission type. For the backscattered emission type the parameters are yield

and the energy loss factor, and for the plasma emitter ionization energy, ionization as fraction of losses, electron temperature, total plasma current and incident particle type must be defined. As these parameters could not be obtained by direct measurements in the coating planta set out of the ALADIN database in Opera was suggested by the support. (29) Some parameters were set to match the deposition experiments in the coating plant. The calculation can take very long. So therefore, it is wise to try to use the symmetry of your model. So divide the model into smaller parts, but everything in it must be symmetric.

Input parameters of SCALA:

- Temperature in [°C] = 23°
- Pressure in [mtorr]
- Voltage difference between target and steel pot [V]
- Operating current in [A] divided by 16, because solving is necessary only for 1/16 of the centrosymmetric model, which saves a lot of computing time
- Target-substrate distance [cm]

The input parameters for each experiment are shown in Table 7.

Table 7: Input parameters and overview over all simulated experiments

name	target	power [W]	pressure [mtorr]	distance[cm]	voltage [V]	current [A]	Bias [V]	mode	Wafer	simulated mode
B343_5	Ti	200	10,50	5	-375	0,47	-60	DC	3zoll	DC
B343_6	Ti	200	10,50	7	-367	0,52	-60	DC	3zoll	DC
B343_7	Ti	300	10,50	5	-432	0,66	-60	DC	3zoll	DC
B343_8	Al	200	12,75	5	-473	0,43	-60	DC	3zoll	DC
B343_10	Ti	200	12,00	5	-316	0,62	-60	DC	3zoll	DC
B343_11	Ti	200	14,25	5	-294	0,64	-60	DC	3zoll	DC

Using these parameters the program solves the model by calculating 41 iterations. After that the program stops even if the convergence is not reached.

5.3.4 Output parameters

The solved calculations were analyzed with the post processor of Opera.

The output parameters of TOSCA used in this thesis are:

- X/B profile on the magnets – with X being the distance from the outer edge of the magnet and B being the magnetic flux density – see chapter "Direct magnetic measurement"
- 3D distribution of the flux density B [T] in various distances to the copper plate
- Illustration of the orientation of the magnetic field

The output parameters of SCALA are:

- Monitoring of particle tracks
- Power density along a plane
- Particle distribution on the substrate
- Particle distribution on the target
- Particle distribution along selected planes between target and substrate

The main interests of the TOSCA output within this thesis were the B and the X/B profiles of the SCALA module the particle distribution on the substrate. To compare the simulation result with the experiment, conversion is necessary. In the post processor a 6x6 cm plane with 32 points at the surface of the substrate was generated. On this plane at each point the beam density particles per area and second are displayed. The values were exported to excel and converted into an illustration of the film thickness.

5.3.5 Calculations to compare the experiments with the simulations

The Opera software cannot calculate the film thickness or distribution in nanometer. In order to compare the simulations with the experiments, the beam density was converted to film thickness by the following formulas, assuming identical density of bulk and deposited Ti and Al-films. It is possible that the true film thickness is even higher.

$$mass_{1\ Atom}\ [g] = \frac{molar\ mass\left[\frac{g}{mol}\right]}{N_A\left[\frac{particle}{mol}\right]} \qquad (1)$$

$$M\left[\frac{\mathrm{g}}{\mathrm{s}}\right] = \mathrm{mass}_{1\mathrm{atom}}[\mathrm{g}] * \mathrm{N}\left[\frac{\mathrm{particle}}{\mathrm{s}}\right] \quad (2)$$

$$deposition\ rate\ \left[\frac{cm}{s}\right] = \frac{M\left[\frac{g}{s}\right]}{A\ [cm^2] * \varrho\ [\frac{g}{cm^3}]} \quad (3)$$

$$film\ thickness\ [nm] = deposition\ rate\ \left[\frac{cm}{s}\right] * \mathrm{t}\ [\mathrm{s}] * 10^7 \quad (4)$$

Ti: ϱ = 4,5 g/cm³ molar mass = 47,867 g/mol

Al: ϱ = 2,7 g/cm³ molar mass = 26,98 g/mol

N_A = 6,022*10^23 particle/mol

N_A…avogadro constant

Molar mass…molar mass of Ti or Al

ϱ… density of Al or Ti

M… mass of Ti or Al particles

$Mass_{1atom}$… the mass of one Ti or Al atom

Deposition rate…the rate of the area which gets deposited during a time period

Film thickness…the thickness of Ti or Al-film at this point

The thickness was calculated for all 32x32 points of the beam density, which are the points of the calculated plane on the substrate surface.

6 Results and Discussion

The first part of this chapter shows the results from the magnetic simulations and the magnetic measurements. Identical distances between magnets and measurement points in the simulation and in reality were chosen. The comparison should demonstrate an eventually coherence. The second part discusses the coherences in film thickness, derived from simulation and experiment.

6.1 Magnetic field determinations and comparison

6.1.1 Comparison between Gaussmeter GM08 and 410

Figure 24: X/B-profiles measured by GM08 and GM410

Figure 24 shows a comparison of measurements with the Gaussmeter GM08 of JOANNEUM RESEARCH and the Gaussmeter 410 of the Montanuniversität Leoben. The measurement setup is described in section 5.2.4.1.2. Both measurements yielded almost identical results: Between 0 and 1 and 3,5 to 5 cm B varies between 0 and -0.196 T, in between it increases to a maximum of 0,312 T The minima are located in the area of the outer ring whereas the maximum is at the position of the inner permanent magnets. Table 8 shows the direct comparison of the minima and the maximum of the measurements with both Gaussmeters.

Table 8: Comparison of minima and maxima of both Gaussmeter

Gaussmeter	left min. [T]	max. [T]	right min. [T]	stand. Deviation
GM08	-0,196	0,312	-0,185	0,009
GM410	-0,167	0,301	-0,166	0,00823

For the rest of the magnetic measurements only the Gaussmeter GM08 of JOANNEUM RESEARCH was used.

6.1.2 3D magnetic field distribution

The 3D distribution of the magnetic flux density B was calculated and measured on the copper plate of the Torus 2"cathode. To compare the simulation with the experiment, the magnetic fields in a plane directly on the copper plate and in a distance of 2 cm are displayed.

6.1.2.1 Simulation results

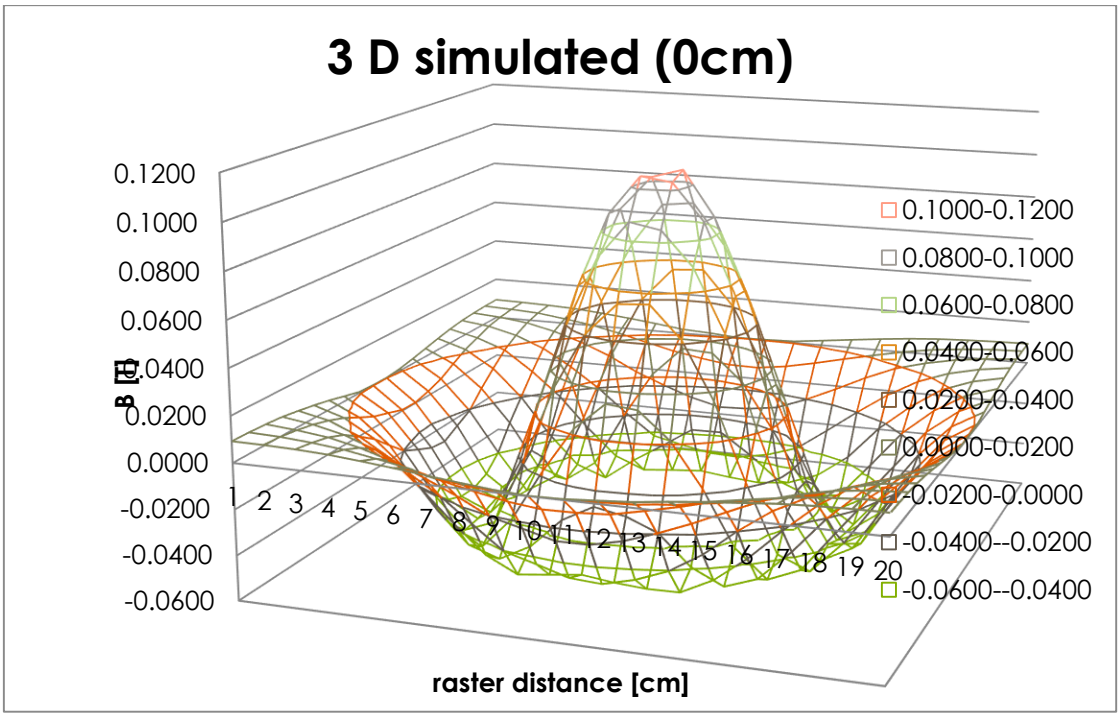

Figure 25: 3D simulated distribution of B[T] at 0 cm distance

Figure 25 shows the simulated magnetic field in a plane directly in front of the 2" Torus cathode at 0 cm distance. The plane in the simulation consists of 19x21 points. The shape of the magnetic flux density is negative (between -0.06 and -0.02 Tesla) and forms a symmetric cone above the inner magnets with values between -0.06 T and 0.12 T.

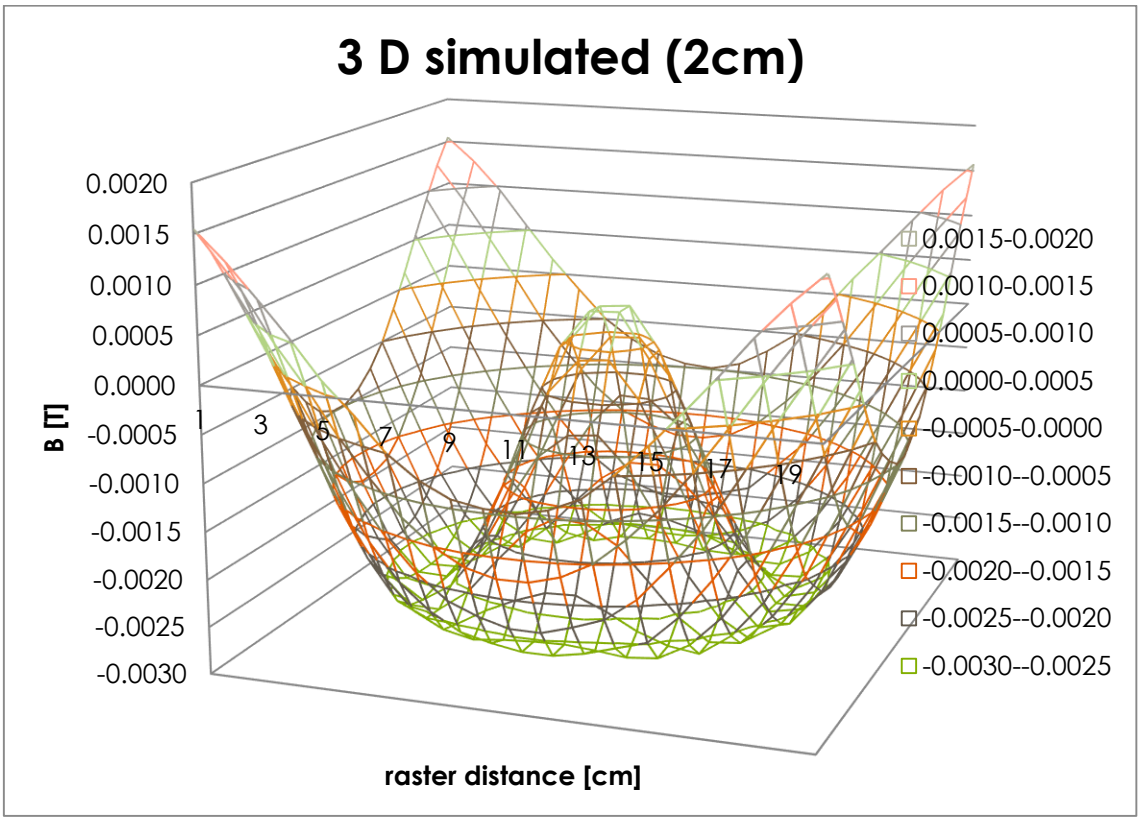

Figure 26: 3D simulated distribution of B[T] at 2cm distance

The magnetic flux density B decreases with increasing distance from the magnets. Figure 26 shows the magnetic field in a plane at 2 cm distance from the front plate of the 2"Torus cathode. The magnetic flux density decreases rapidly and varies only between -0.0025 and 0.0020 T. The shape of the magnetic field remains approximately the same.

The simulation results show that the B generated by the NdFeB permanent magnets is symmetric and decreases with distance from the magnets. It also shows that the width of the cone is about 5-7 cm and the shape of the cone does not change significantly with distance.

6.1.2.2 Experimental Results

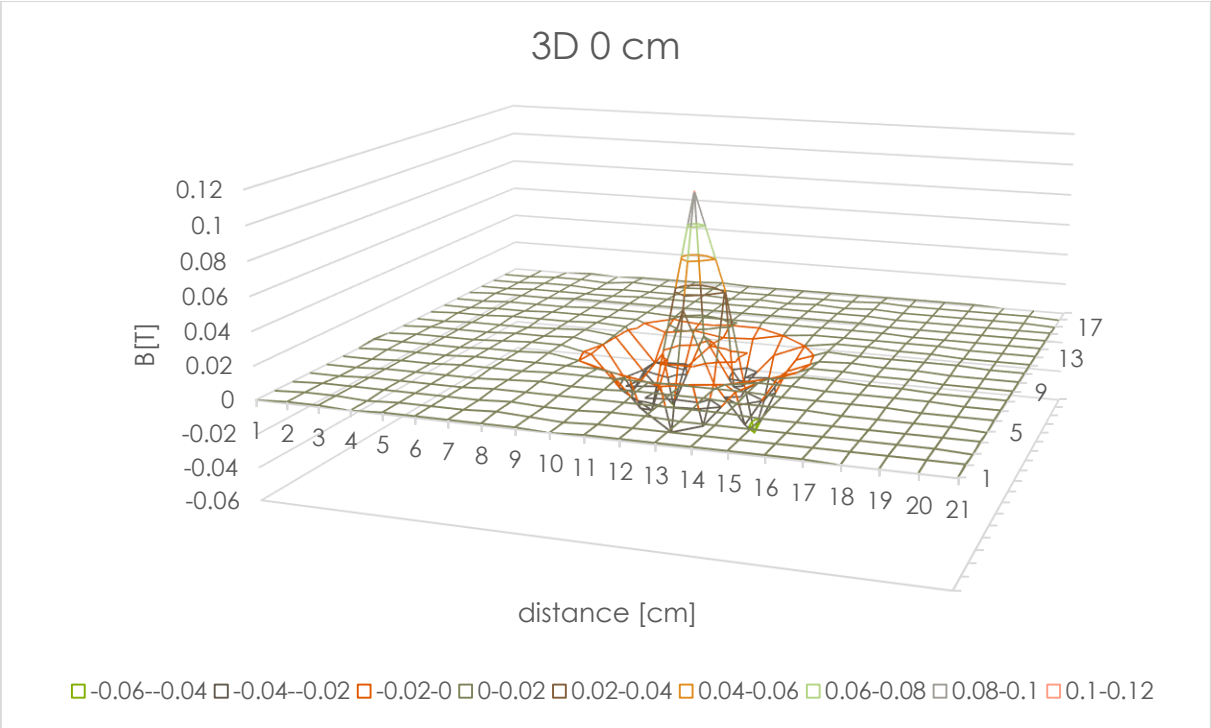

Figure 27: Measured 3D distribution of B [T] at 0 cm

Figure 27 shows the 3D distribution of the measured magnetic flux density B at 0 cm distance. B was measured in a 19x21 point grid with a distance of 1 cm between individual points. The shape of the B-filed is comparable to the simulated results with a decrease above the outer ring of the magnets and a cone shaped increase above the center. The values vary between -0.06 to 0.12T. The width of the cone in the simulation was 5-7 cm, which corresponds with the width of the outer magnet ring. It can be concluded that the simulation overestimates the expansion of the real magnetic field.

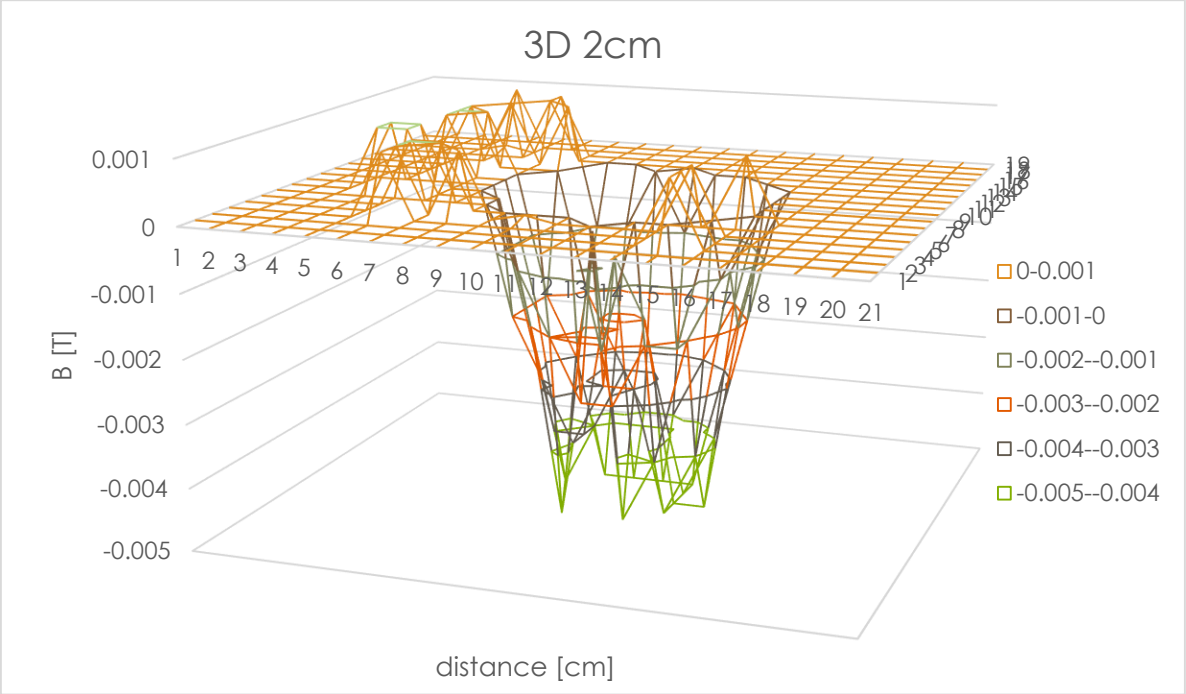

Figure 28: 3D distribution of B[T] at 2cm distance

Figure 28 shows the measured magnetic field B in 2 cm distance to the 2"Torus cathode. The magnetic field at this distance varies only from -0.005 to 0.002 T, which is in the range of the uncertainty of the measurement of the GM08. In a distance of 2 cm the Gaussmeter does not deliver reliable results anymore.

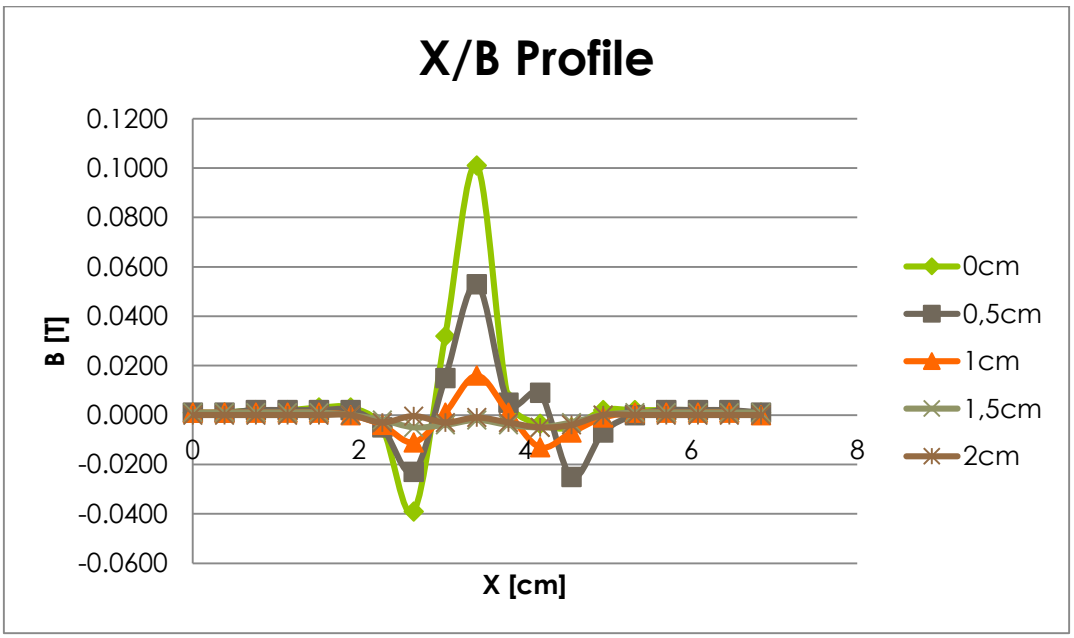

Figure 29: Measured X/B-Profile at different distances from the copper plate of the Torus 2"cathode

Figure 29 shows a profile of the magnetic flux density at different distances from the copper plate of the Torus 2" cathode. As expected, the magnetic flux density decreases with increasing distance. Also the profile at 0 cm and 0.5 cm is not symmetric due to the absence of a negative part at around X = 5 cm. This might be caused by the relatively large distance between measuring points of 1 cm, resulting in a maximum between two measuring points. So it is not excluded that the curve is symmetric at 0 and 0.5 cm distance, but could have been obscured by too less measurement point density.

6.1.3 Measurement of individual magnets

The inner permanent magnets on the ferromagnetic steel plate were measured by the Gaussmeter GM08 Table 9 shows the magnetic flux density of the cylindrical inner permanent magnets.

Table 9: magnetic flux density B of the inner magnets

	B[T]
1	0.642
2	0.651
3	0.626
arithmetic mean	0.640
standard deviation	0.010

The inner Neodymium-Iron-Boron magnet has a magnetic flux density of 0.640 T ±0.01T. The 2*16 magnets of the outer magnetic ring were also measured as shown in Table 10.

Table 10: Measured magnetic flux density B of the outer magnets

	B [T]
1	-0.516
2	-0.533
3	-0.555
4	-0.545
5	-0.534
6	-0.549
7	-0.524
8	-0.528
9	-0.541
10	-0.542
11	-0.543
12	-0.537
13	-0.528
14	-0.538
15	-0.532
16	-0.532
arithmetic mean	-0.536
standard deviation	0.009

The arithmetic mean B of the 16 permanent magnets is -0.536T ± 0.009T. The outer magnets have only 84% of the magnetic flux density of the inner magnets.

6.1.4 Comparison of measured and simulated X/B profile

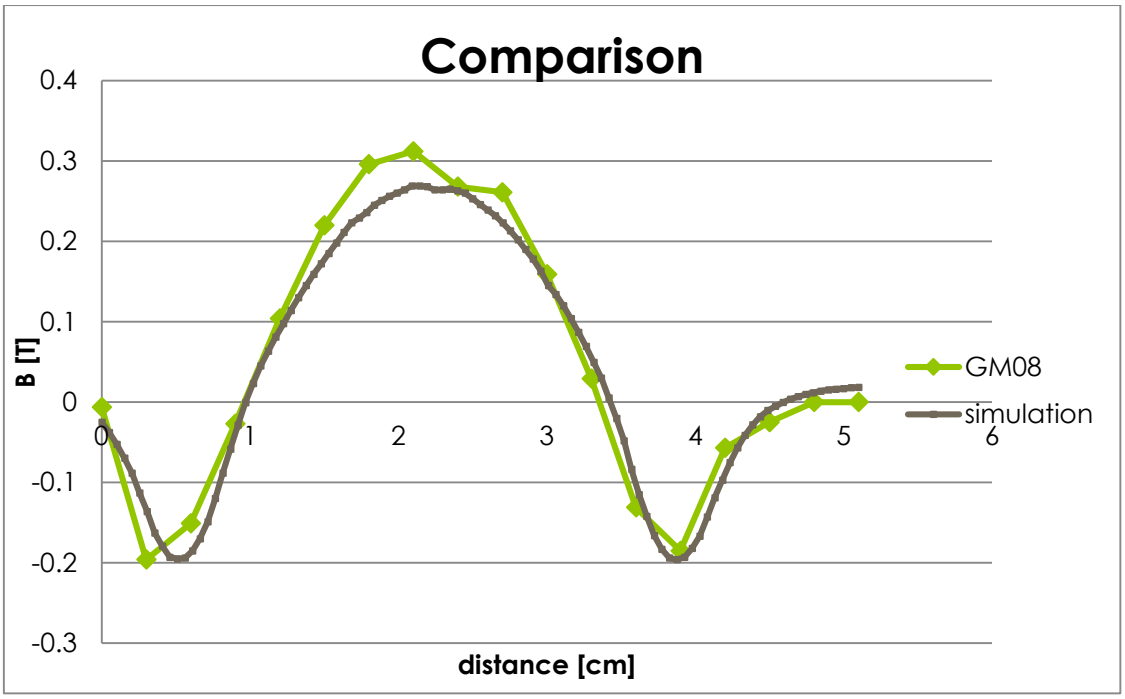

Figure 30: Comparison of measured and simulated data of the magnetic field directly on the permanent magnets

Figure 30 shows the comparison of the simulated and measured X/B profile directly on the permanent magnets. The shape is identical in the simulation and in the experiment. The maxima and minima of the 2 curves are shown in Table 11. The maximum derived from the simulation is 0.269 T, which is 86% of the maximum of the measurement with the GM08. The minimum of the simulation is exactly the same as the minimum of the measurement with the GM08, 0.196 T. This shows that there is good agreement of the magnetic fields derived from the simulation and the experiment.

Table 11: Comparison of the max. and min. B-values

	GM08	**simulation**
max.[T]	0,312	0,269
min.[T]	-0,196	-0,196
std. deviation	0,009	

The measured trend of the magnetic field along a line in different distances from the copper plate is shown in the next diagrams:

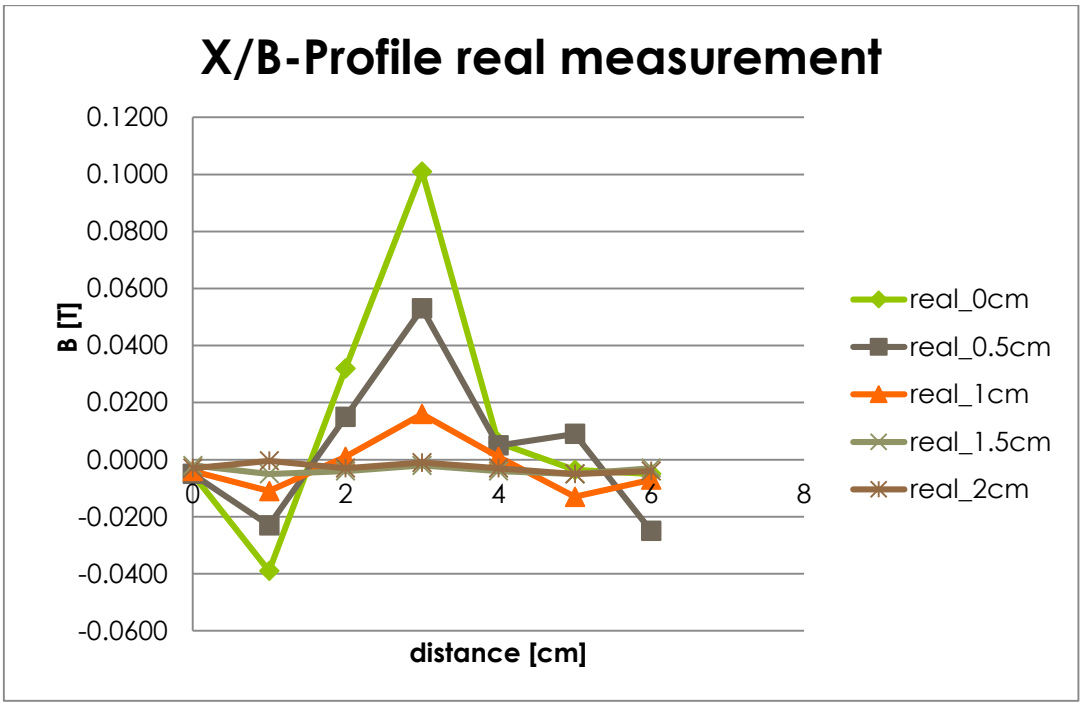

Figure 31: X/B-Profile measured along lines in different distances on top of the cathode (GM08)

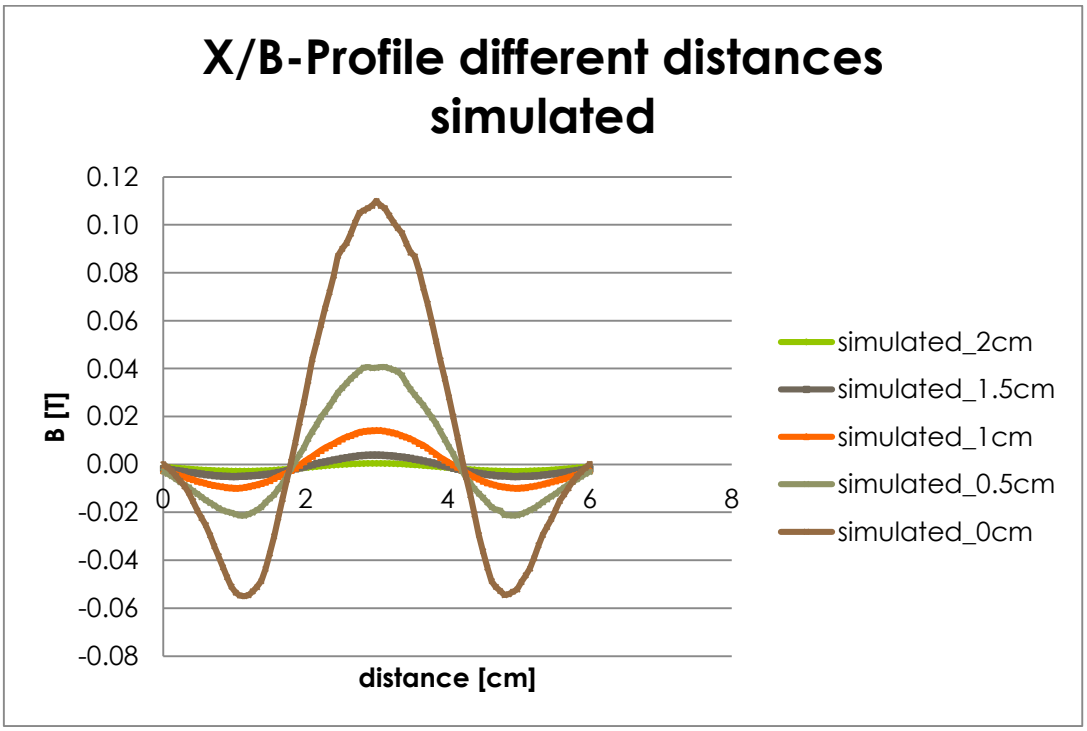

Figure 32: X/B-Profile at different distances on top of the cathode simulated with Opera

In Figure 31 and Figure 32 the simulated and measured X/B-profiles at different distances on top of the cathode are shown. The simulated profiles are more symmetric and smoother because a larger number of points were calculated than measured. The deviation between experiment

and simulation is probably caused by this too low number of measurement points and the rather large distance between 2 points of 1 cm. The trends in simulation and experiment are comparable. The maximum and minimum of both curves at 0 cm is about 0.1 and 0.05 T and at 2 cm close to 0 T. As expected, the magnetic flux density B decreases with distance.

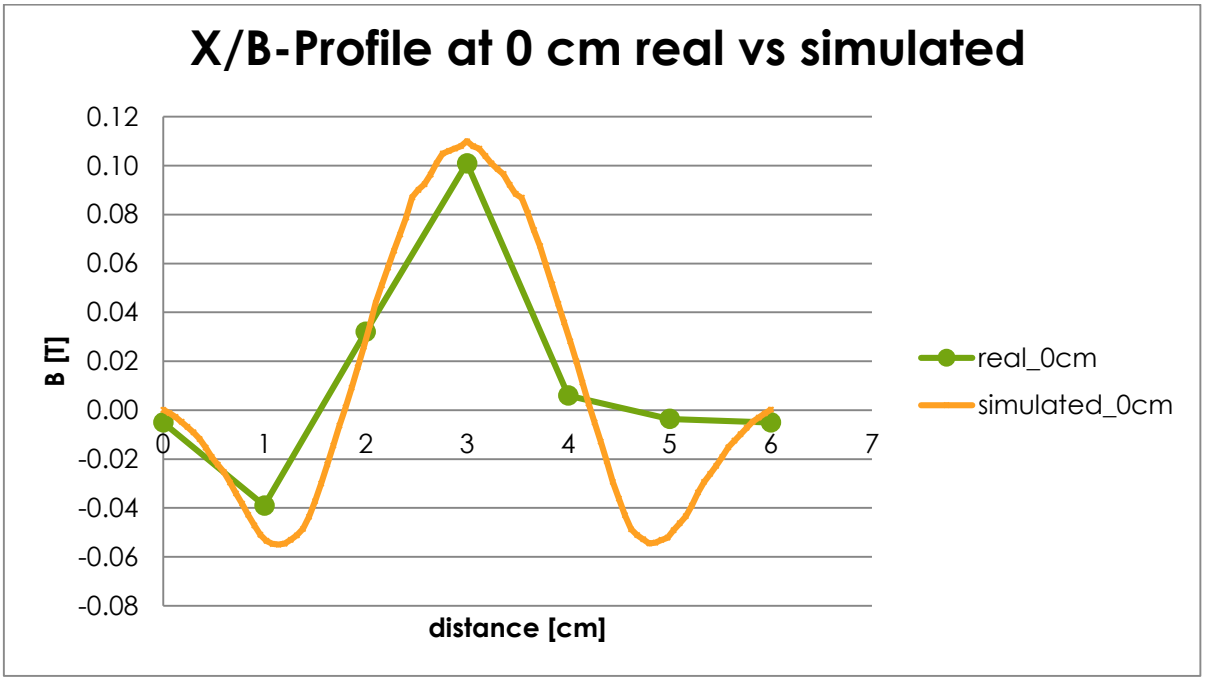

Figure 33: Comparison of the simulated and measured X/B profile at 0 cm

In Figure 33 the comparison of the simulated and measured X/B profile directly on top of the copper plate at 0 cm distance is shown. In the simulation, B is calculated at much higher number of points than it was measured. Therefore, the simulated negative branch of the profile around 5 cm distance was either not measured in the experiment or the magnets partly lost their nominal magnetic strength. This might be caused by overstepping their Curie temperature during cooling breakdown and overheating in a sputter deposition experiment.

The simulations of the magnetic field were used as input parameter for and film thickness calculations with the SCALA solver, which are discussed in the next chapter.

6.2 Thickness distribution

In this chapter the thickness of thin Al- or Ti-films calculated by the SCALA solver and profilometric measurements of real deposition experiments are compared and discussed.

6.2.1 Comparison of thickness distribution

The error bars of the measured thicknesses are within the size of the symbols.

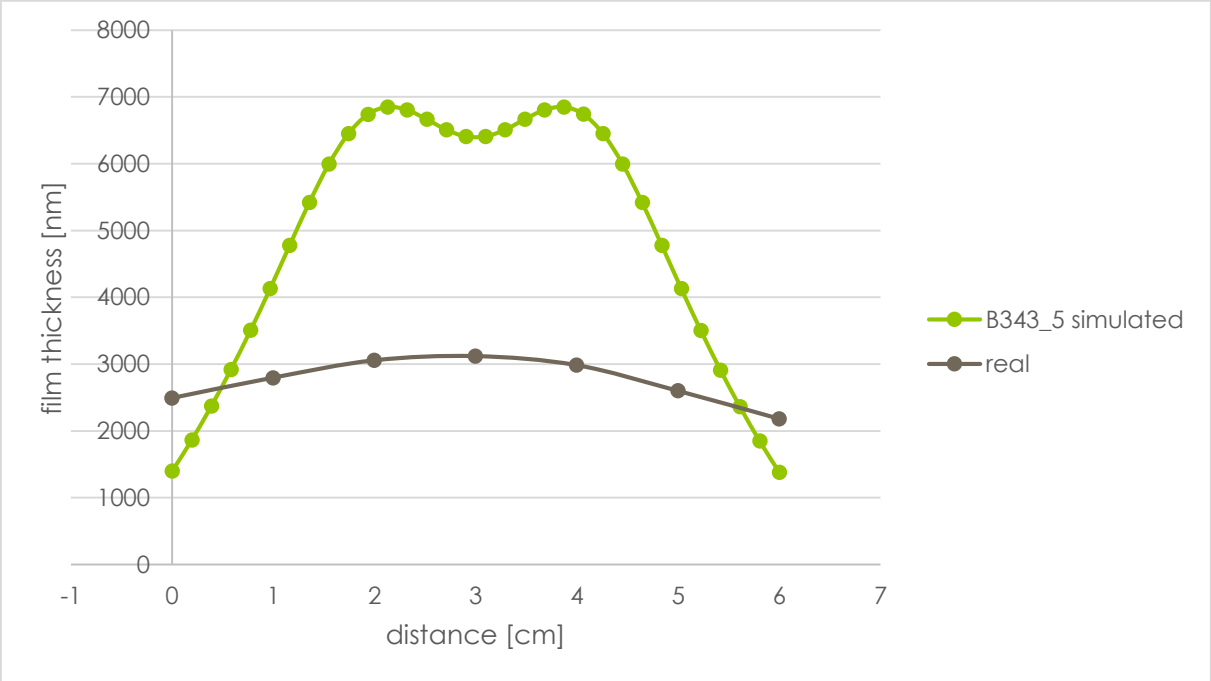

Figure 34: Comparison of simulated and real thickness of a Ti thin film deposited at 200W, 0.014mbar and 5 cm target-substrate distance

Figure 34 shows the comparison of the simulated and measured thickness distribution of a titanium thin film deposited at 5 cm target-substrate distance (experimental run number B343_5). The measured profile increases continuously from 2181nm in the margin to 3120nm in the center. The maximum deposition rate of this experiment is 0.86 nm/s. The simulation in contrast yielded two maxima of 6850 nm and one local minimum of 6409 nm between them. The lowest thickness of the Ti-film in the margin of the silicon wafer was calculated to1381 nm. The maximum deposition rate in the simulation is 1.76 nm/s and differs by a factor of 2

from the measurement. Furthermore, the shape of the thickness distribution is different.

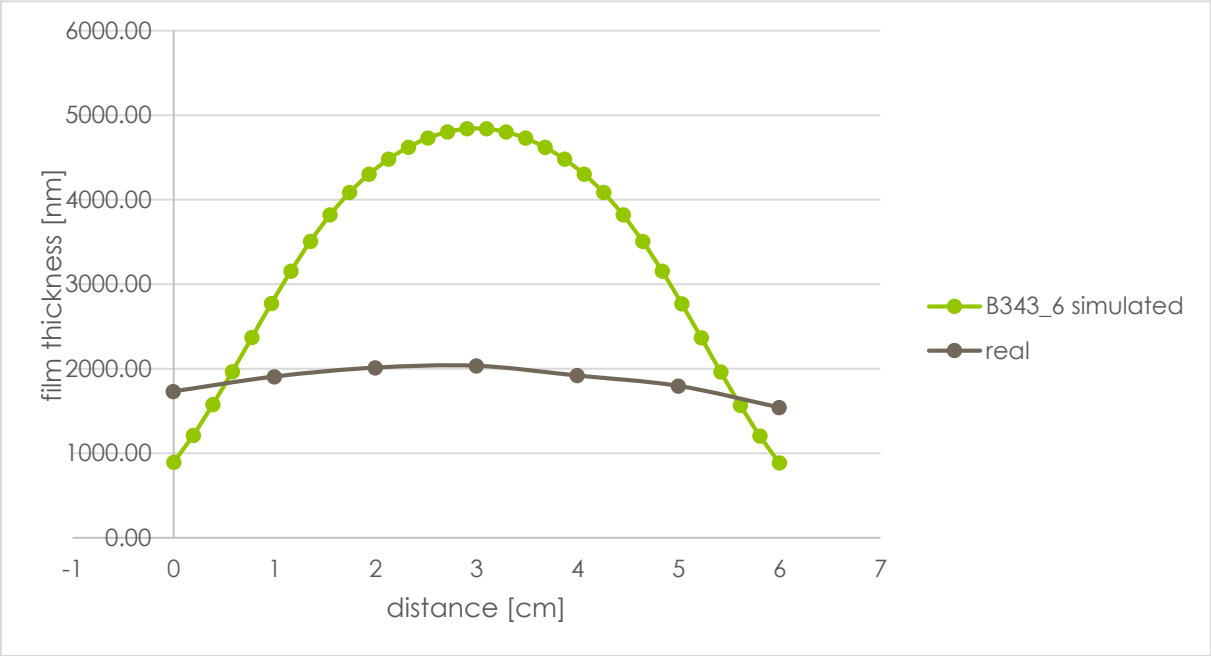

Figure 35: Comparison of simulated and measured thickness of a Ti film deposited at 200 W, 0.014 mbar and 7 cm target-substrate distance

Figure 35 shows the comparison of simulated and measured thickness of a Ti-film deposited at 200 W and 7 cm target-substrate distance (B343_6). The shape of the simulated thickness distribution is similar to the deposition experiment. The thickness has one maximum in the center and then decreases to both sides. The film thickness variation of the simulation from 885 to 4841 nm is much higher than the measured one from 1542 to 2034 nm. The measured and simulated deposition rates are 0.53 and 1,24 nm/s, respectively.

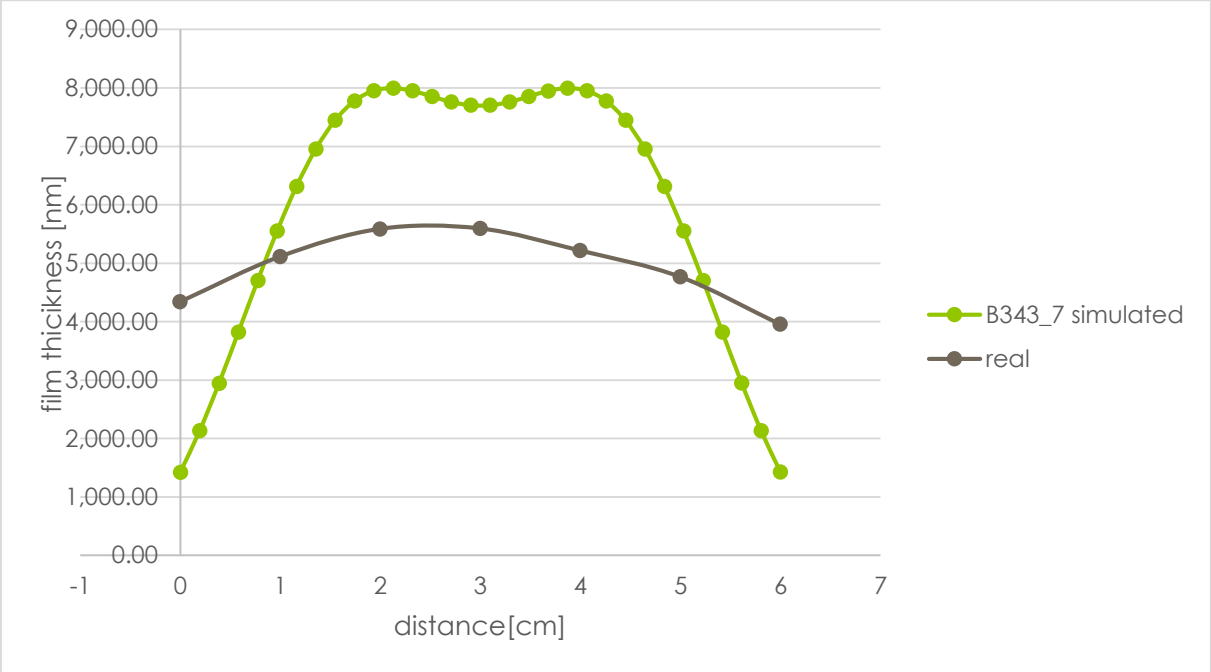

Figure 36: Comparison of simulated and measured thickness of a Ti-film deposited at 300 W, 0.014 mbar and 5 cm target-substrate distance.

Figure 36 Figure 35 shows the comparison of simulated and measured thickness of a Ti-film deposited at 300 W and 5 cm target-substrate distance (B343_7).The measured film thickness shows only one maximum at 5593 nm whereas the simulation yielded two maxima (7996, 7995 nm) and one local minimum in the center between them (7703 nm). However, the difference between the two maxima and the local minimum is not as big as in the samples B343_2 and B343_5. The simulated deposition rate is 2,05 nm/s and measured 1,47 nm/s. The comparison between simulation and reality still strongly overestimates the thickness differences between rim and center of the silicon wafer by a factor of 1.4t in contrast to a factor 2 as it was for the 3 before discussed samples.

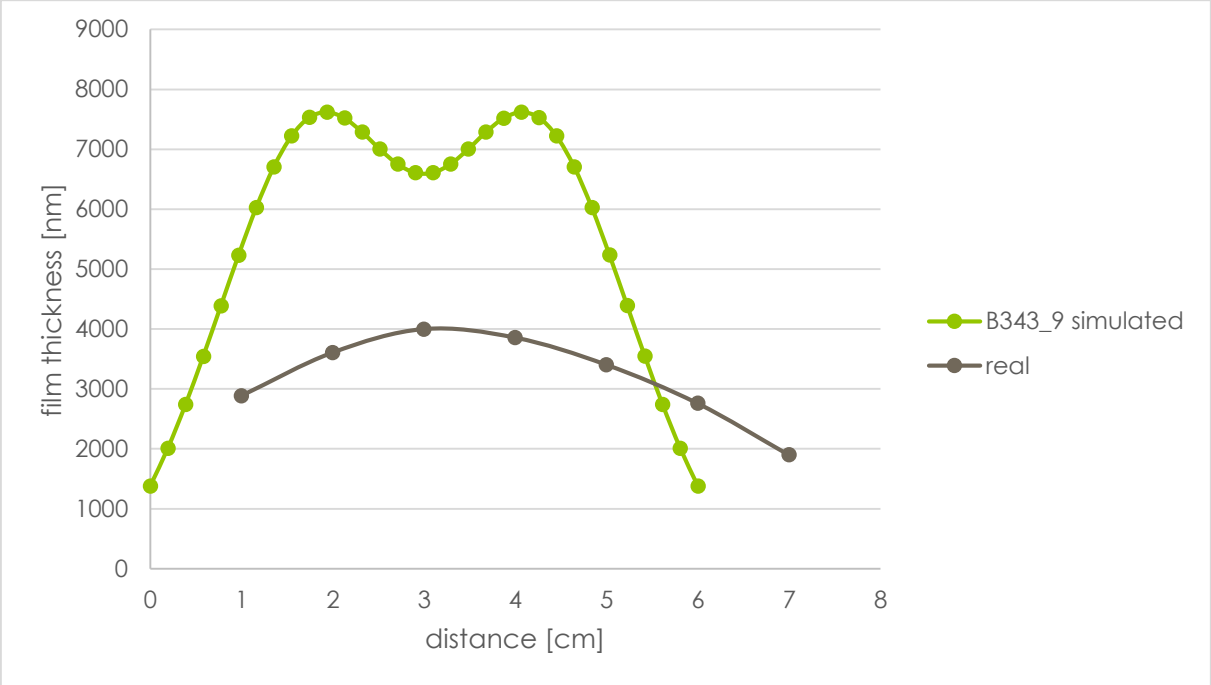

Figure 37: Comparison of simulated and measured thickness of an Al-film deposited at 200 W, 0.016 mbar and 5 cm target-substrate distance.

Figure 37 shows the comparison of simulated and measured thickness of an Al-film deposited at 200 W, 0.016 mbar and 5 cm target-substrate distance (B343_9). In this experiment the deposition of the Al-thin film was done in DC mode. The simulation shows two maxima (7620 nm, 7621 nm) and a local minimum (6609nm), the absolute minimum of the simulated thickness is 1377nm. The simulated deposition rate is 2,31 nm. The measured thickness shows only one maximum at 3997 nm and a continuous decrease towards the rim to 1899 nm. The deposition rate of the experiment is 1,14 nm/

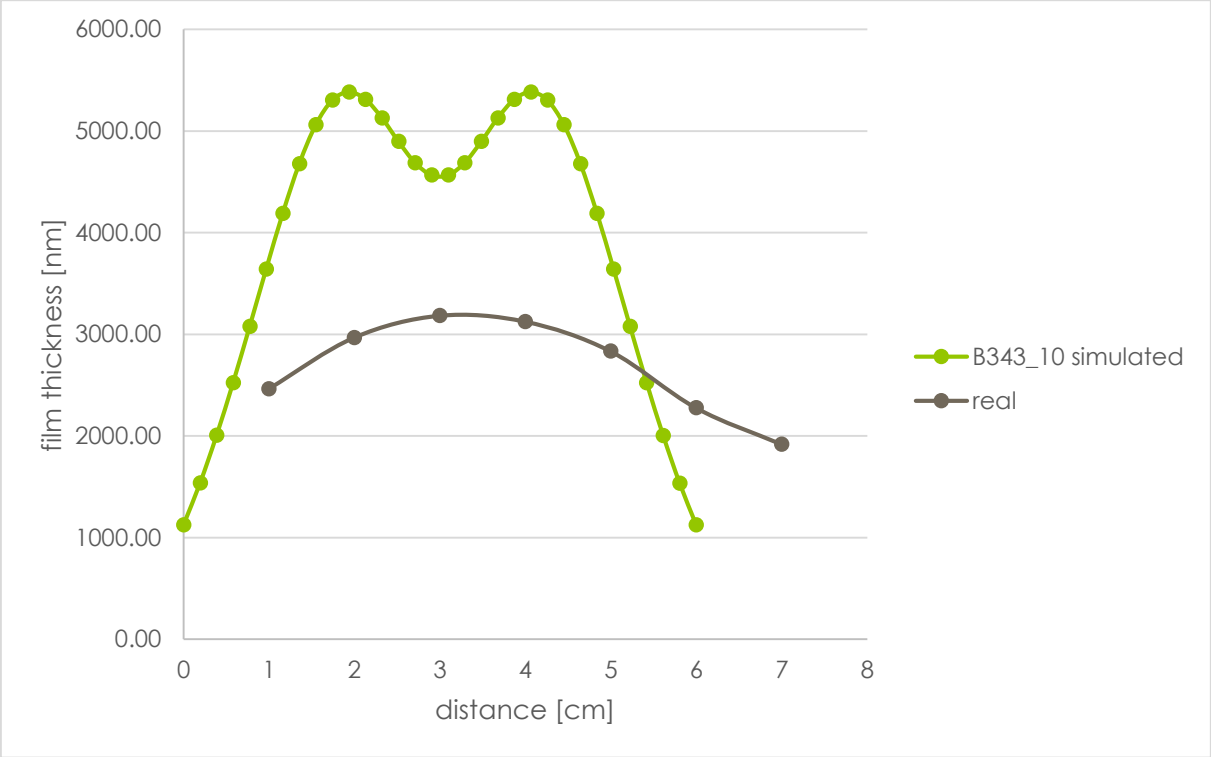

Figure 38: Comparison of simulated and measured thickness of a Ti-film deposited at 200 W, 0.016 mbar and 5 cm target-substrate distance.

Figure 38 shows the comparison of simulated and measured thickness of a Ti-film deposited at 200 W, 0.016 mbar and 5 cm target-substrate distance (B343_10). The shape of the simulated thickness is the same as before with two maxima (5385 nm) and a pronounced local minimum (4567 nm). The minimum thickness in the rim is 1125 nm, the simulated deposition rate is 1,36 nm/s. The measured thickness of the sample varies between 1919 and 3194 nm, the deposition rate is 0.8 nm/s.

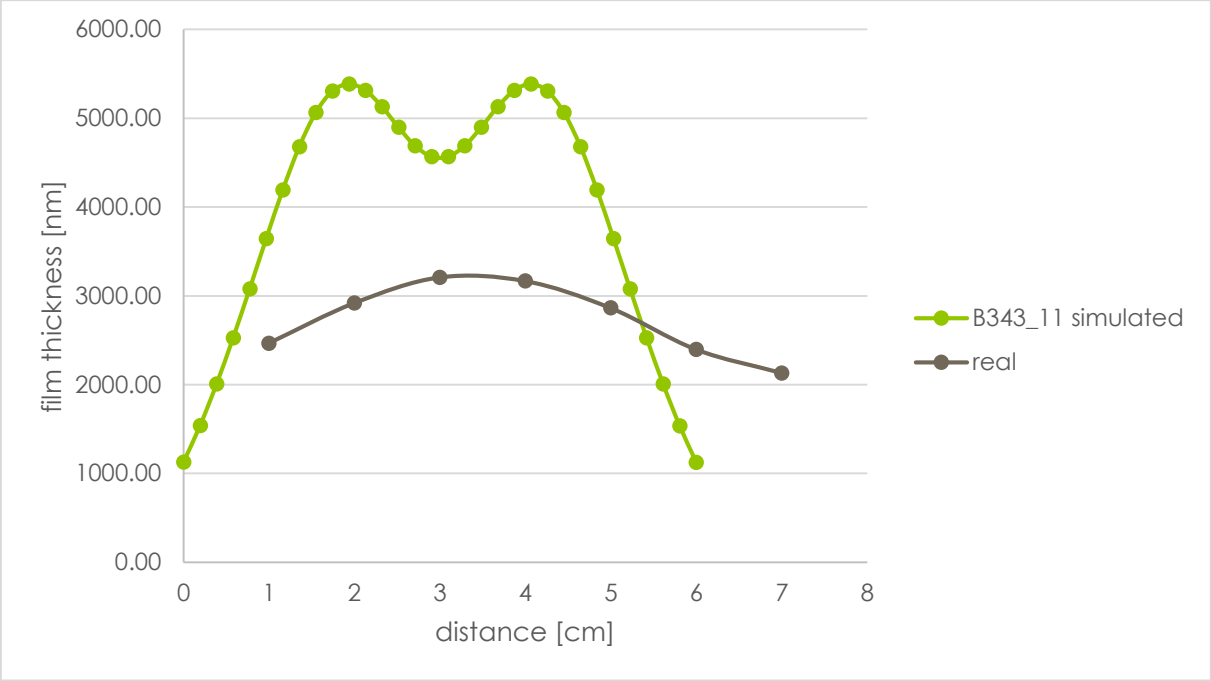

Figure 39: Comparison of simulated and measured thickness of a Ti-film deposited at 200 W, 0.019 mbar and 5 cm target-substrate distance.

Figure 39 shows the comparison of simulated and measured thickness of a Ti-film deposited at 200 W, slightly higher pressure of 0.019 mbar and 5 cm target-substrate distance (B343_11). The simulation shows again two thickness maxima (5385 nm) and one local minimum (4567 nm). The deposition rate calculated from the simulation is 1,38 nm/s. The maximum measured thickness in the center is 3208 nm, the deposition rate of the experiment is 0.8 nm/s.

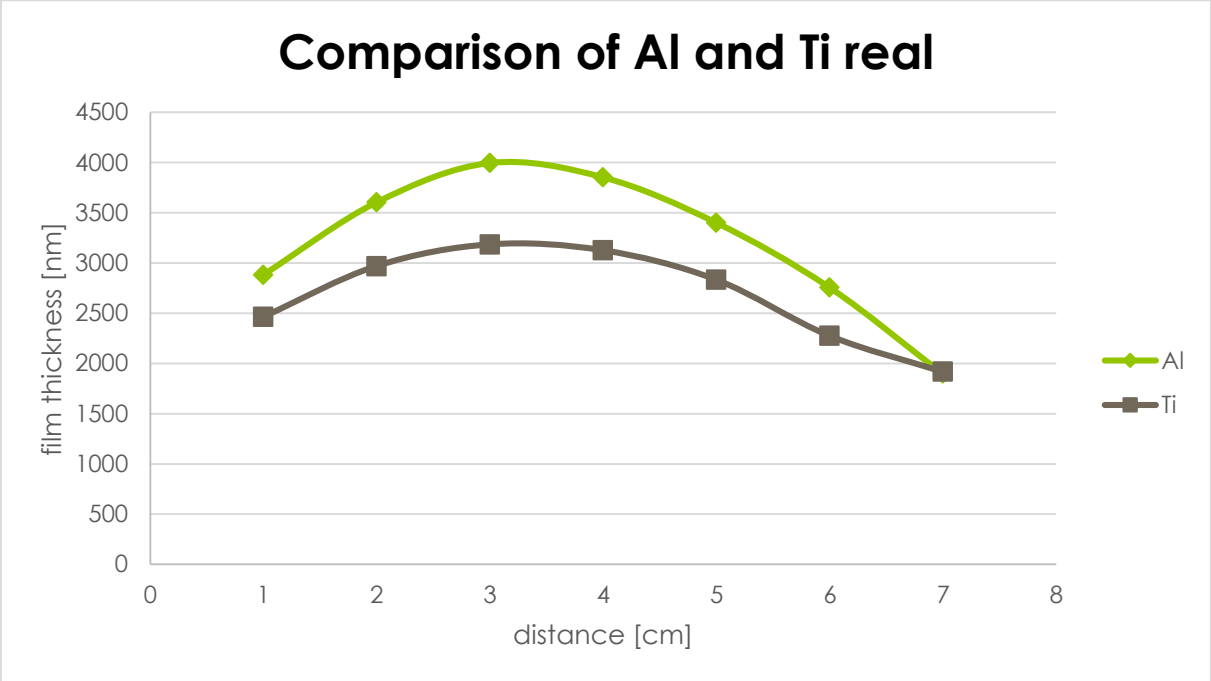

Figure 40: Comparison of the measured thickness distribution of deposition experiments B343_9 and B343_10.

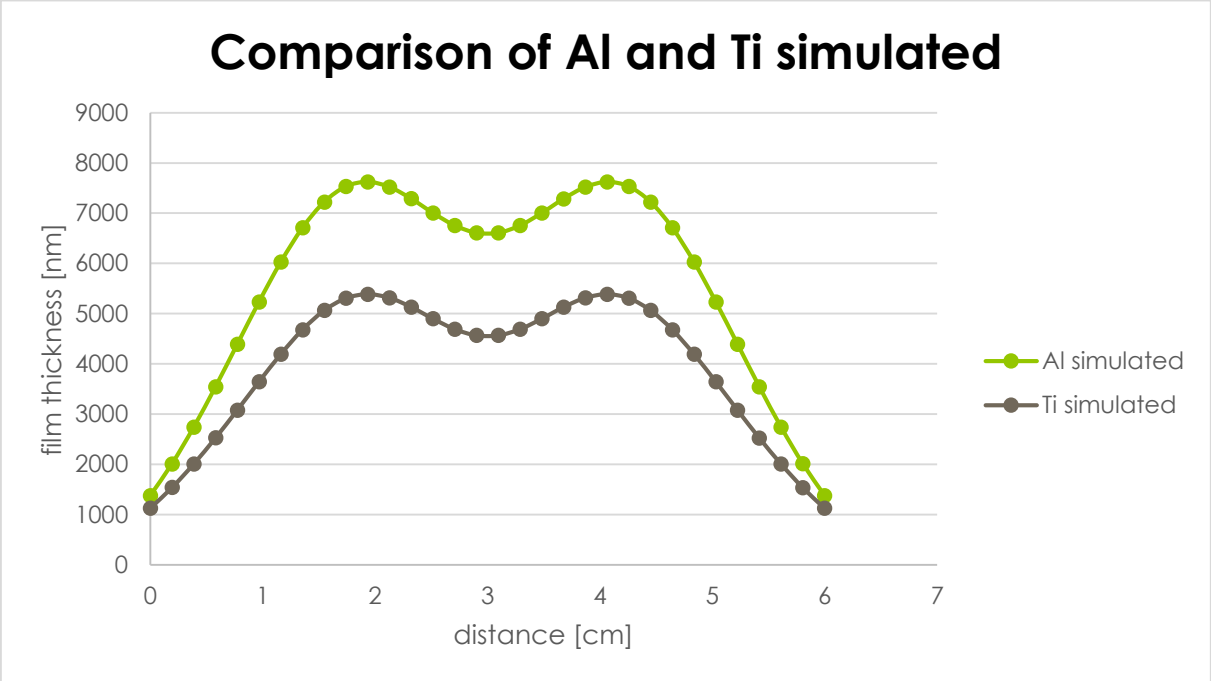

Figure 41: Comparison of simulated thickness distribution of experiments B343_9 and B343_10.

Figure 40 shows the different sputter yield of depositions from an Al- and a Ti-target. The thickness distribution shows the same shape but the thicker Al-film (at identical deposition parameter) indicates the higher sputter yield compared to Ti. The same trend is visible in the

simulated thickness distributions in Figure 41. The lighter and weaker bonded element aluminum is easier to sputter than Ti. Although the simulated and measured thickness data significantly differ, both yield the same trend.

6.2.2 Comparison of deposition rate and particle number in simulation and experiment

Pressure, power and target-substrate distance were varied and trends derived from the simulation and the experiment were verified.

Table 12: Comparison of simulated and measured deposition rate and the number of particles.

		real			simulated	
real		deposition rate[nm/s]	number of particles/scm²	film thickness [nm]	deposition rate[nm/s]	number of particles/scm²
DC	B343_5	0,8554	4,8635E+15	3336,043	1,76	9,99E+15
DC	B343_6	0,5286	3,005E+15	2061,468	1,24	7,06E+15
DC	B343_7	1,4718	8,368E+15	5739,998	2,05	1,17E+16
DC	B343_9	1,136	6,5942E+15	3749,167	2,31	1,34E+16
DC	B343_10	0,7962	4,622E+15	3105,353	1,36	7,85E+15
DC	B343_11	0,7996	4,642E+15	3118,803	1,38	8,2E+15

In Table 12 simulated and measured deposition rate, number of particles and film thickness of several experiments are shown. The measured deposition rate is always lower than the simulated one. The film thickness and deposition rate depends on the number of particles and yield the same trend. B343_9 was a sputter process with an Al-target, the other experiments were deposited from Ti.

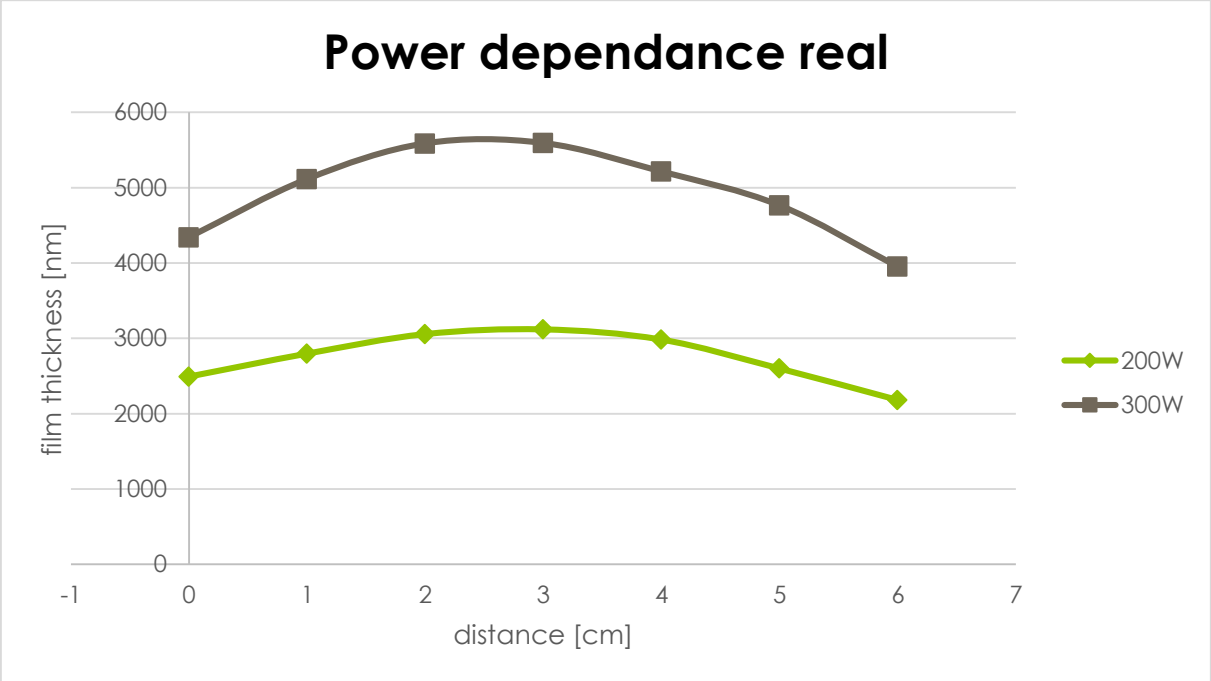

Figure 42: Measured thickness distribution at 200 and 300 W sputter power (experiments B343_5 and B343_7)

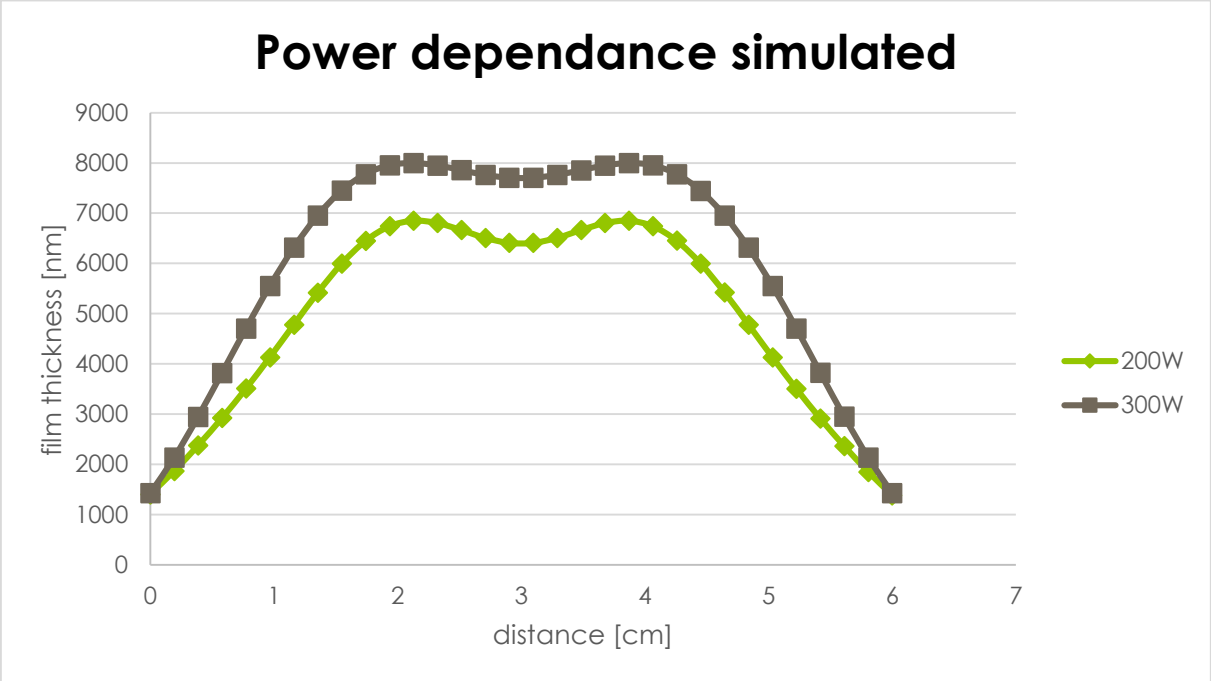

Figure 43: Simulated thickness distribution at 200 and 300 W sputter power (experiments B343_5 and B343_7)

Figure 42 shows how the thickness distribution of a Ti-thin film varies depending on the used sputter power. More power increases film thickness: an enhancement of the power of one third increases the maximum thickness to about 80% from 3120 to 5593 nm. In Figure 43 the thickness distribution of the simulations B343_5 and B343_7 are shown. The simulation shows the same trends as the deposition experiment. At 200 W the maximum thickness is 6850 nm and at 300W 7997 nm, which is an increase of about 16%. In reality the thickness increase with power is much more significant than in the simulation.

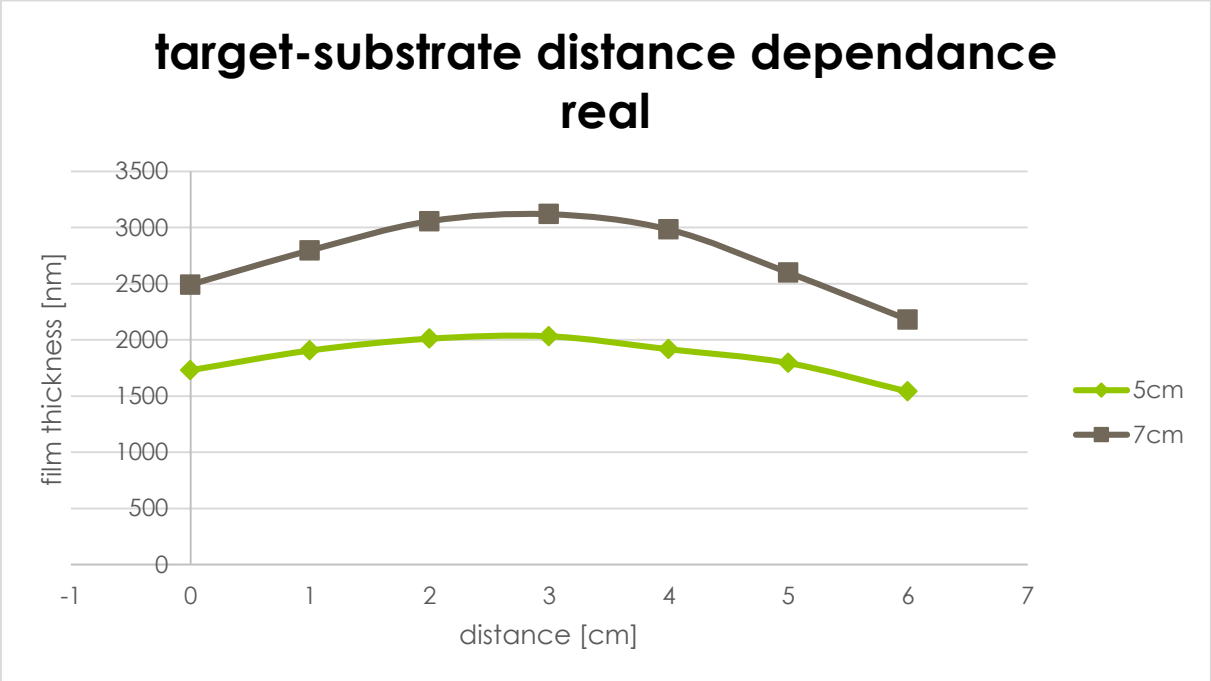

Figure 44: Measured thickness distribution at 5 and 7 cm target-substrate distance (experiments B343_5 and B343_6)

Figure 44 shows the measured thickness distribution of two experiments where the parameter of the target-substrate distance was changed. The shape is the same in both cases. The thickness increases with distance. At 5 cm the maximum thickness is 2034 and at 7 cm 3120 nm. All other parameters of the sputter process were fixed. This demonstrates the importance of an optimized target-substrate distance to obtain the highest possible deposition rate.

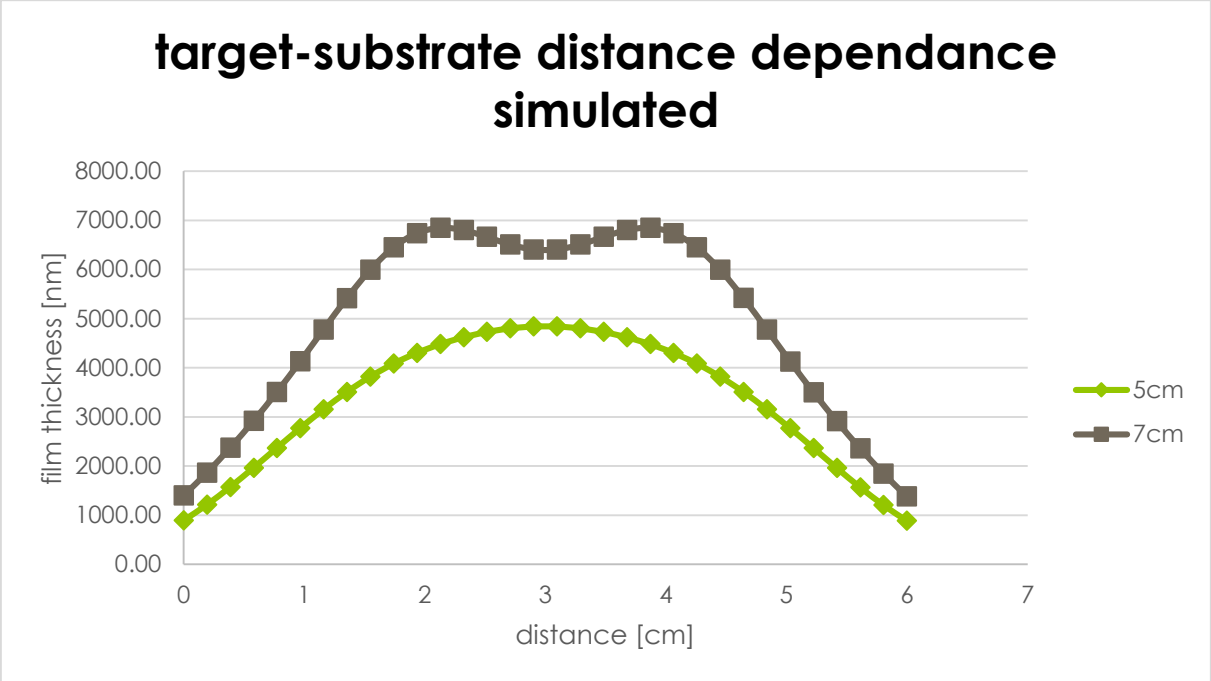

Figure 45: Simulated thickness distribution at 5 and 7 cm target-substrate distance (experiments B343_5 and B343_6)

Figure 45 shows the simulated thickness distribution when the target-substrate distance is changed from 5 to 7 cm. The simulation shows the same trend as the deposition experiment. With increasing the target-substrate distance the thickness also increases. Additionally, the shape of the thickness distribution changes from two maxima and one local minimum at 5 cm to only one maximum in the center at 7 cm, similar the deposition experiment B343_6. Both measured and simulated film thickness distributions confirm the existence of an ideal target-substrate distance to obtain the highest deposition rate. The simulation also suggests that the shape of the thickness distribution changes with the target-substrate distance.

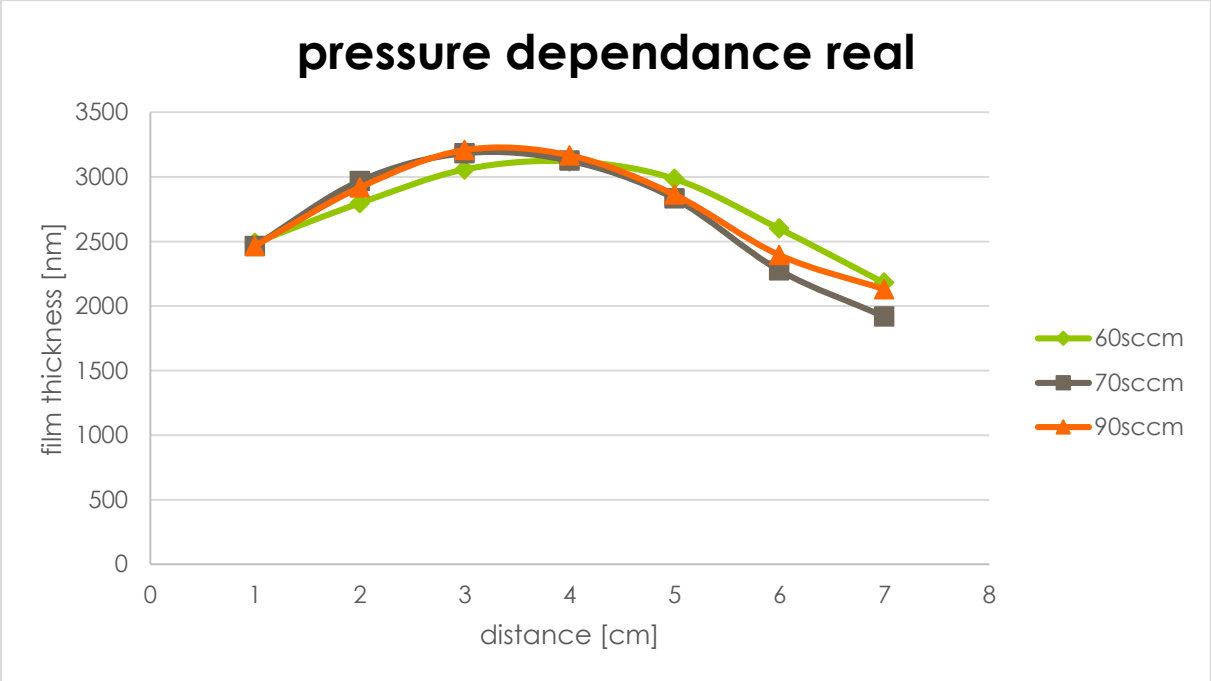

Figure 46: Measured thickness distribution at three different gas-flow rates (experiments B343_5, B343_10 and B343_11).

Figure 46 shows the thickness distribution of a Ti thin film deposited at different gas-flows, respectively chamber pressure. There is no significant difference between 70 and 90 sccm Argon. At a sputter pressure of 60 sccm the thickness distribution shows the same shape but is slightly shifted compared to the other experiments. The maximum thicknesses of the 3 experiments are 3208 nm (90 sccm), 3184 nm (70 sccm) and 3120 nm (60 sccm). Deposition pressure seems to have only small influence on the film thickness.

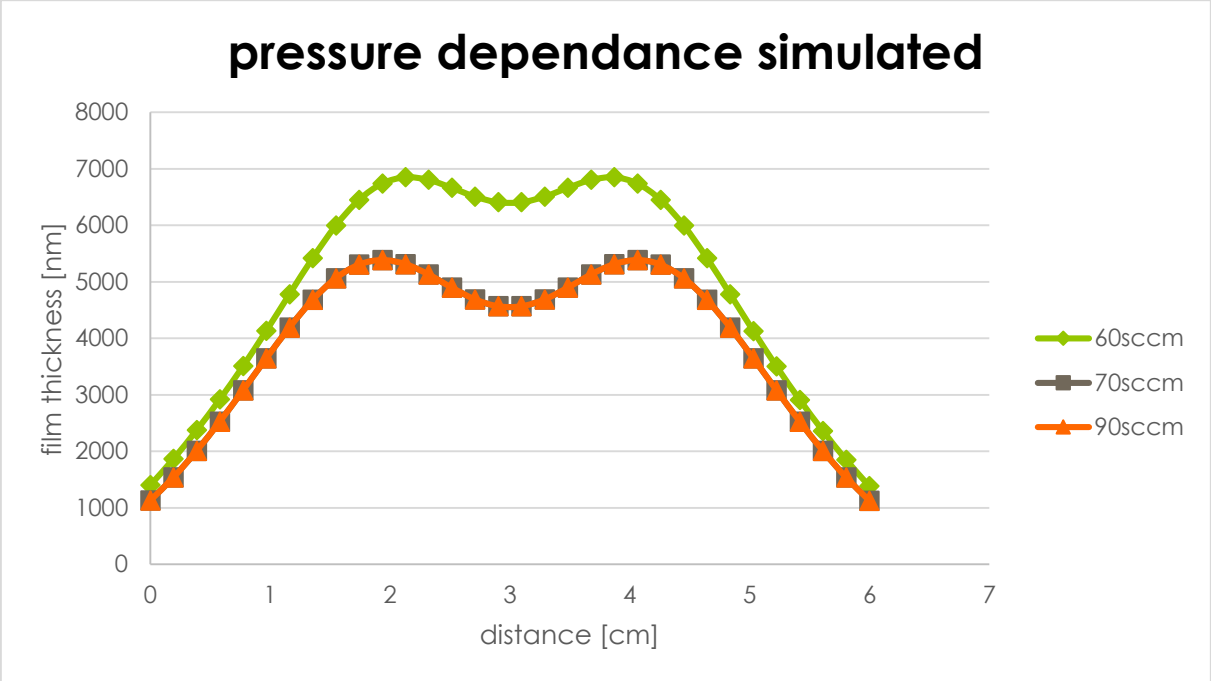

Figure 47: Simulated thickness distribution at three different gas-flow rates (experiments B343_5, B343_10 and B343_11).

Figure 47 shows the simulated thickness distribution changes with gas-flow, pressure change, respectively. The simulation yielded a big decrease from 60 to 70 sccm, but not from 70 to 90 sccm. This is contradictory to the measured film thickness distribution.

7 Conclusion

The aim of this thesis was the comparison of a simulated sputter process using the Software "Opera" with a real sputter process in a commercial PL-600 Sputter Coater from Pfeiffer. The permanent magnetic field in the magnetron Torus 2" cathode was investigated and the thickness of sputtered Al- and Ti- thin films. The magnetic flux density B was:

- directly measured by a Gaussmeter on the permanent magnets and
- in planes directly on top of the copper plate of the cathode and in 2 cm distance.

Though the simulation and the experimental sputter process are not fully comparable, some conclusions can be drawn. There is no significant difference between the measured and simulated-calculated flux density B along a line as well as in planes on top of the copper plate and in 2 cm distance.

The film thickness calculated by the SCALA module shows a significant difference to the measurements from the experiment. By comparing the trends of different parameters during the sputter process it is shown that some of them are observed in the simulation and the experiment. By varying the target substrate distance from 5 to 7 cm the film thickness decreases, as shown both in the experiment and the simulation. Contrary to the measurements the simulation yields a minimum in the center of the substrate, only at 5 cm distance. Both, simulation and measurements suggest an ideal target substrate distance for the sputter process. The thickness distribution is power dependent. As expected the thin film sputtered at 300 W is thicker than at 200 W (other parameter fixed). This dependence is shown by both experiment and simulation.

The results of the magnetic measurement on top of the copper plate of the Torus 2"cathode are not comparable with the simulation. The analysis of the 3D expansion of the magnetic field B shows differences. The simulation result shows a much wider and more symmetric expansion of B and the experiment shows a smaller expansion, but it has the same shape as the simulation. The magnetic simulation is furthermore used to simulate the sputter process. The parameter which was investigated for the sputter process itself is the film thickness.

The absolute simulated thickness of the thin films is not comparable with the experiment. The film thickness which is calculated by the simulation is twice as high as the thickness achieved by the experiment. Also some of the simulations show that there is a minimum above the center

of the target, which does not appear in reality. The simulation and the experiment both show that aluminum exhibits a higher sputter rate than titanium, confirmed by a higher film thickness of aluminum than that of titanium (at identical setting of process parameters).

The measured film thickness of the deposition experiments does not show a significant dependence on the sputter pressure. The simulation instead yields higher film thickness at 60 sccm compared to 70 or 90 sccm.

The conclusion of this thesis is that the program "Opera" is able to simulate real magnetic fields and flux densities. In contrast there is a significant difference in measured and simulated Ti- and Al-thin film thickness. Exact simulations of Ti- or Al-thin films sputtered in the coating plant at JOANNEUM RESEARCH- MATERIALS Niklasdorf at the moment are not possible.

8 Bibliography

1. **Kelly, P.J. and R.D.Arnell.** Magetron sputtering: a review of recent developments and applications. *Vacuum.* 2000, 56, pp. 159-172.

2. **Roth, J. Reece.** *Industrial Plasma Engineering Volume 2.* Cornwall : MPG Books, 2001. 0750305444.

3. **McLeod, P.S. and Hartsough, L.D.** *Vacuum Science Technology.* 1977, 14, pp. 263-265.

4. **Waits, R.K.** *Vacuum Science Technology.* 1978, 15, pp. 179-187.

5. **Window, B. and N.Savvides.** *Vacuum Science Technology A.* 1986, 4, pp. 453-456.

6. **Savvides, N. and B.Window.** *Vacuum ScienceTechnology.* 1986, 4, pp. 504-508.

7. **D.G.Teer.** *Surface Coating Technology.* 1989, 39/40, p. 565.

8. **Sproul, W.D., et al.** *Surface Coating Technology.* 1990, 43/44, pp. 270-278.

9. **S.Schiller, K. Goedicke, J. Reschke, V. Kirchoff, S.Schneider and F.Milde.** *Surface Coating Technology.* 1993, 61, pp. 331-7.

10. **S.M.Rossnagel and Cuomo, J.J.** *Vacuum.* 1988, 38, pp. 73-81.

11. **Collignon, J.S.** *Vacuum Science Technology.* 1995, 13, pp. 1649-1657.

12. **Almond, E.A.** *Vacuum.* 34. 1984. p. 835.

13. **Toth, L. E.** *Transition Metal Carbides and Nitrides.* New York : Academic, 1971.

14. **Mattox, Donald M.** *Handbook of Physical Vapor Deposition (PVD) Processing.* Westwood, New Jersey : Noyes Publication, 1998.

15. **Bunshah, Rointan F.** *Handbook of Hard Coatings.* New York : Noyes Publication, 2001.

16. **Bunshah, R.F.** *Deposition Technologies for Films and Coatings.* Park Ridge, New Jersey : Noyes Publications, 1982. pp. 83-169.

17. **R.F.Bunshah, C.V Deshpandey.** 1985, *J. Vac. Sci. Technol. A*, Vol. 3, p. 553.

18. **Habig, K.H.** 1986, *J. Vac. Sci. Technol. A*, p. 195.

19. **Waldhauser, W.** Abscheidung und Charakterisierung aufgestäubter Hexaboridschichten. 1996.

20. **D.S.Rickerby, P.J.Burnett.** 1988, *Thin film solids*, Vol. 157, p. 195.

21. **S.J.Bull, D.S. Rickerby.** 1988, *Surf. Coat. Technol.*, Vol. 36, p. 743.

22. **M.Chinmulgund, R.B.Inturi and J.A.Barnard.** Effect of Ar gas pressure on growth, structure, and mechanical properties of sputtered Ti,Al,TiAl,Ti3Al film. Thin solid film. 1995, 270, pp. 260-263.

23. **Rossnagel, S.M.** Thin Film Processes II. San Diego : Academic Press, 1991. pp. 12-77.

24. **Y., Pauleau and in W.Gissler, Jehn H.A.(eds).** Advanced Techniques for Surface Engineering. Dordrecht : Kluwer Academic Publisher, 1992. pp. 135-179.

25. **Kahn, Mag.rer.nat. Markus.** Room Temperature Deposition of DLC-Films by an Ion Beam Method,Reactive Magnetron Sputtering and Pulsed Laser Deposition: Process Design, Film Structure and Film Properties. Leoben : s.n., 2009.

26. **Young and D.Hugh.** University Physics. 8, 1992.

27. **Marinescu, Marlene.** Elektrische und Magnetische Felder: Eine Praxisorientierte Einführung. Heidelberg : Springer, 2012. ISBN: 978-3-642-24219-9.

28. **Thomatronik GmbH.** Opera 3 Schulung. Introduction to the Finite Element Method. Rosenheim : s.n., 2014.

29. **Alladin. [Online] IAEA.** [Cited: August 18, 2014.] https://www-amdis.iaea.org/ALADDIN/.

30. A.K.Mukerjee, Nivedita Thkur. Photovoltaic Systems-Analysis and Design. New Delhi : PHILearning Private Limited, 2011. ISBN-978-81-203-4417-4.

31. Fluck, Heumann. Periodensystem der Elemente. Weinheim : WILEY-VCH Verlag GmbH & Co KGaA, 2007. 4. ISBN-978-3-527-31607-6.

32. MIT. 6.777J/2.751J Material Property Database. [Online] Massachusetts Institute of Technology. [Cited: July 15, 2014.] http://www.mit.edu/~6.777/matprops/aluminum.htm. 617-253-1000.

33. Window, B. and Savvides, *N. Vacuum Science Technology A.* 1986, 4, pp. 196-202.

9 Appendix A: Magnetic measurement and simulation

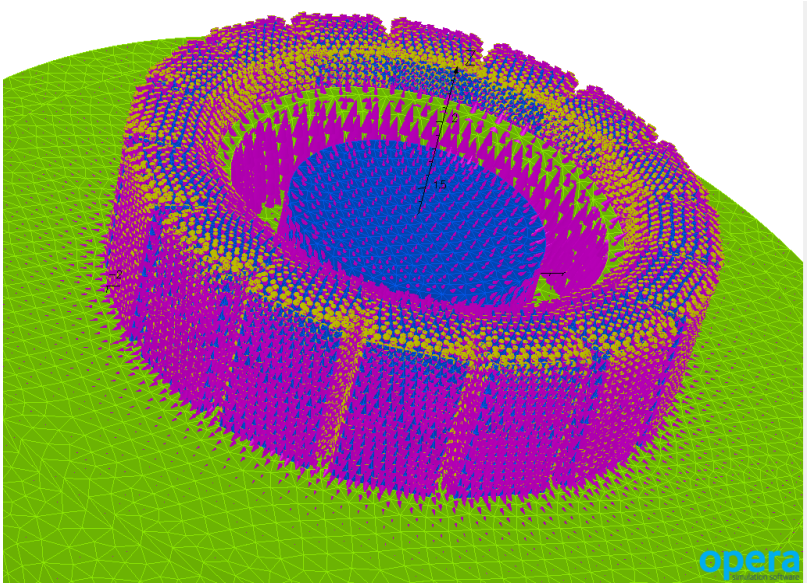

Figure 48: Illustration of the vectors of the permanent magnets in the Opera software

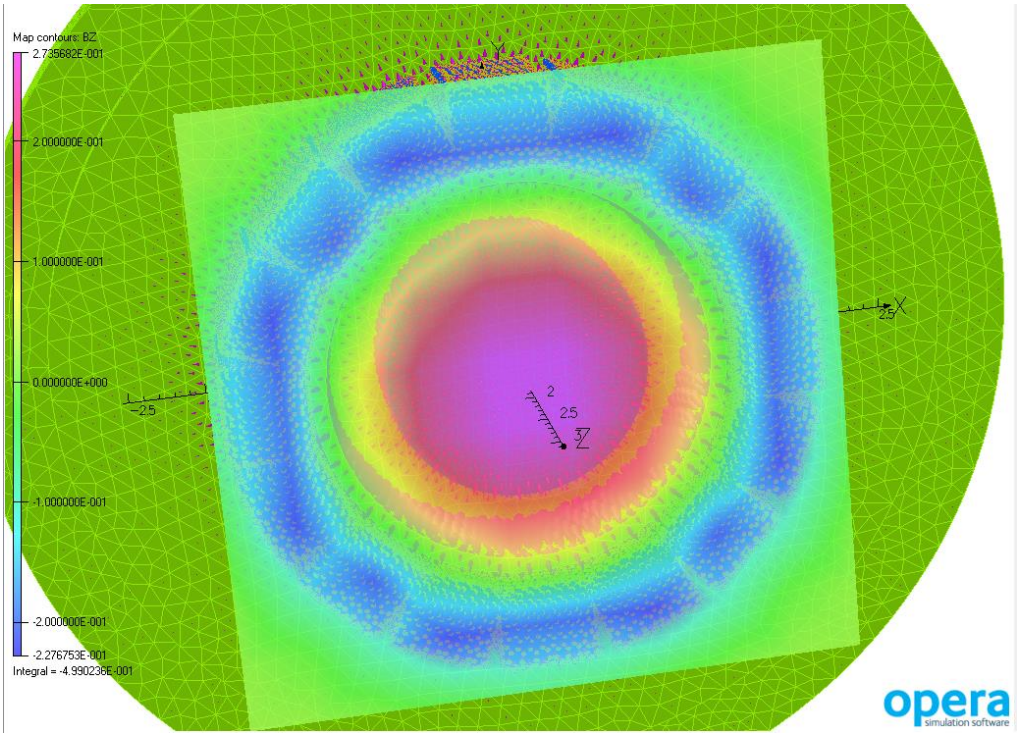

Figure 49: color map of the distribution of the magnetic field B

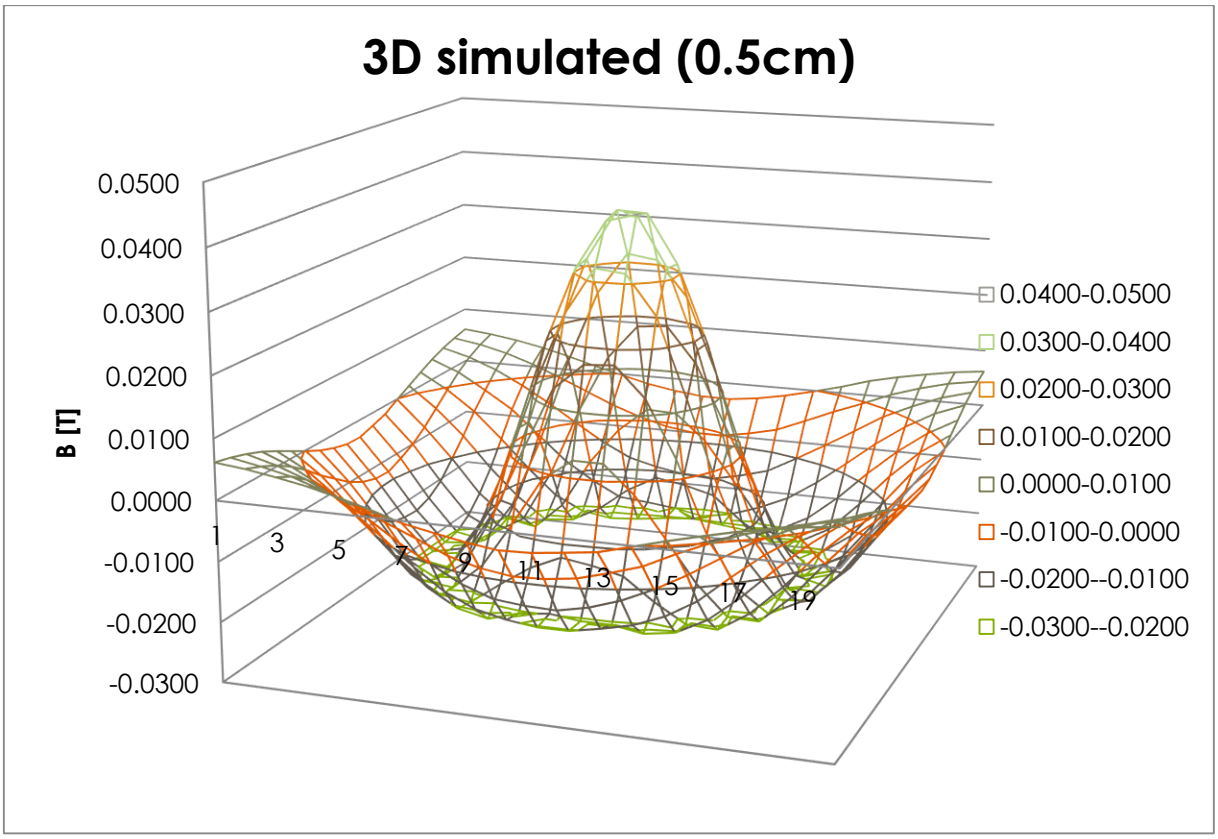

Figure 50: 3D image of simulated B in 0.5cm distance from the magnets

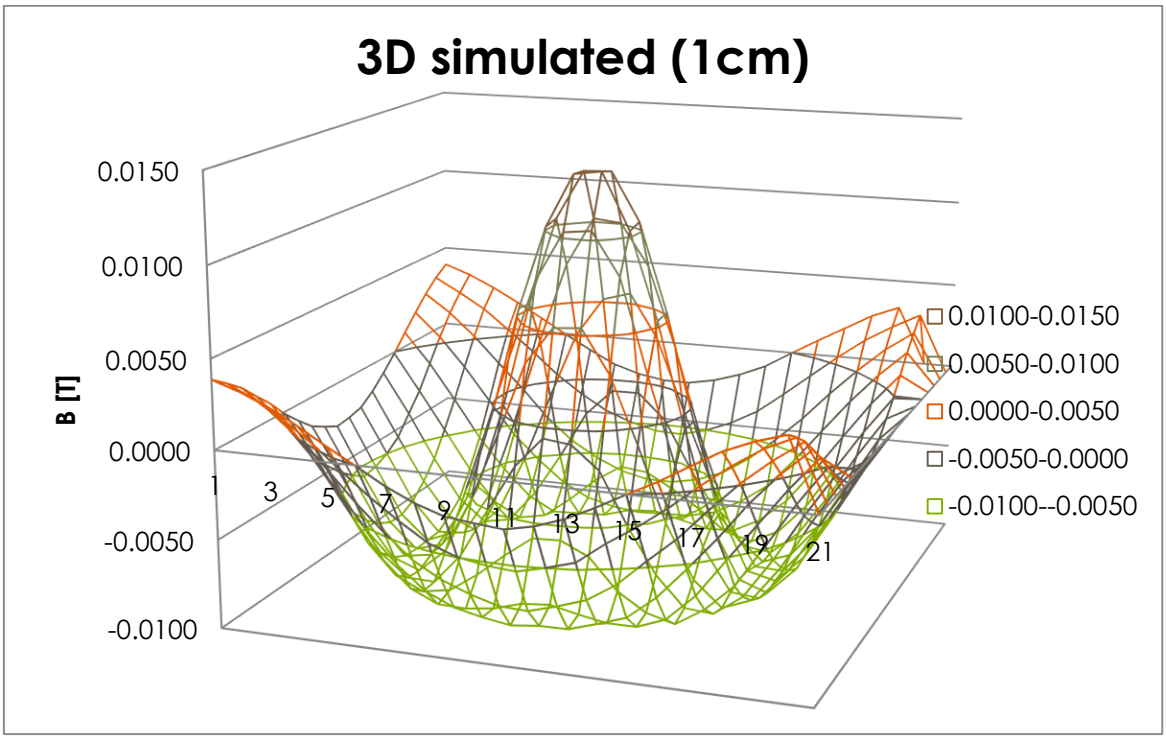

Figure 51: 3D image of simulated B in 1cm distance from the magnets

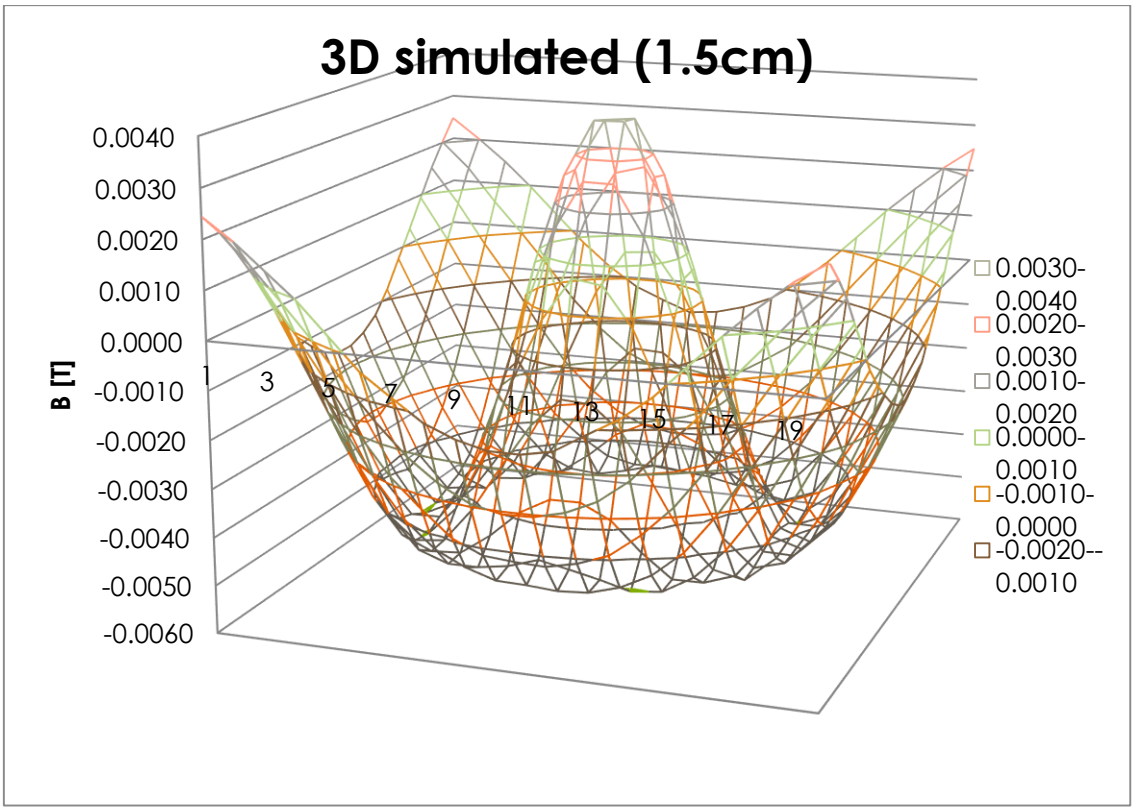

Figure 52: 3D image of simulated B in 1,5cm distance from the magnets

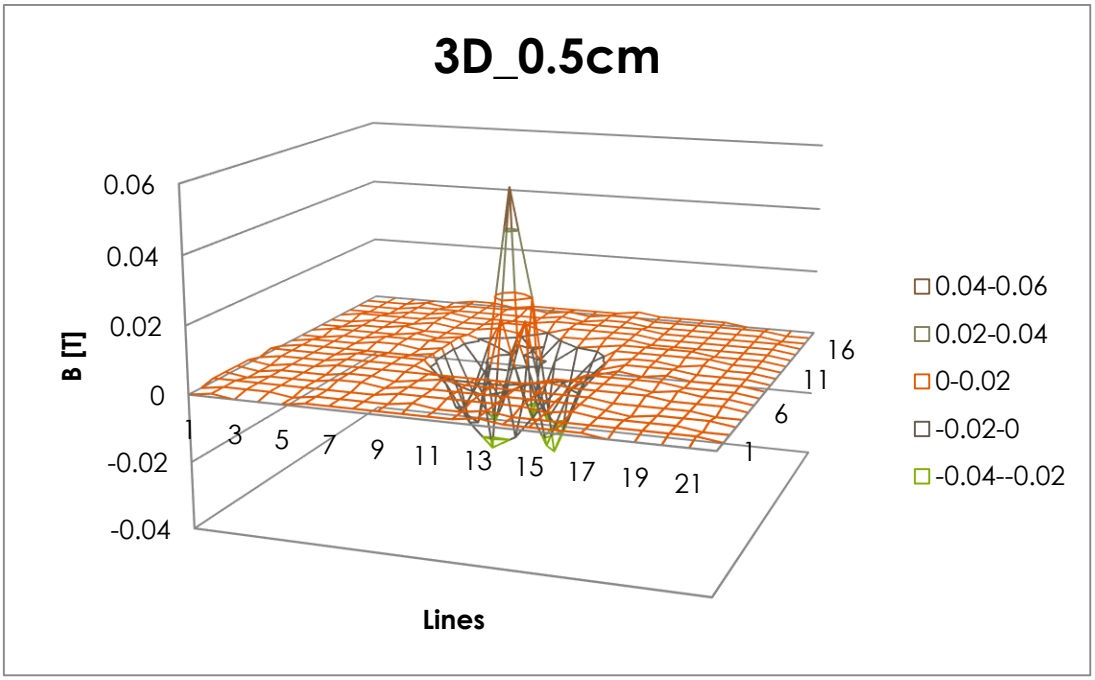

Figure 53: 3D image of B in 0.5cm distance from the magnets

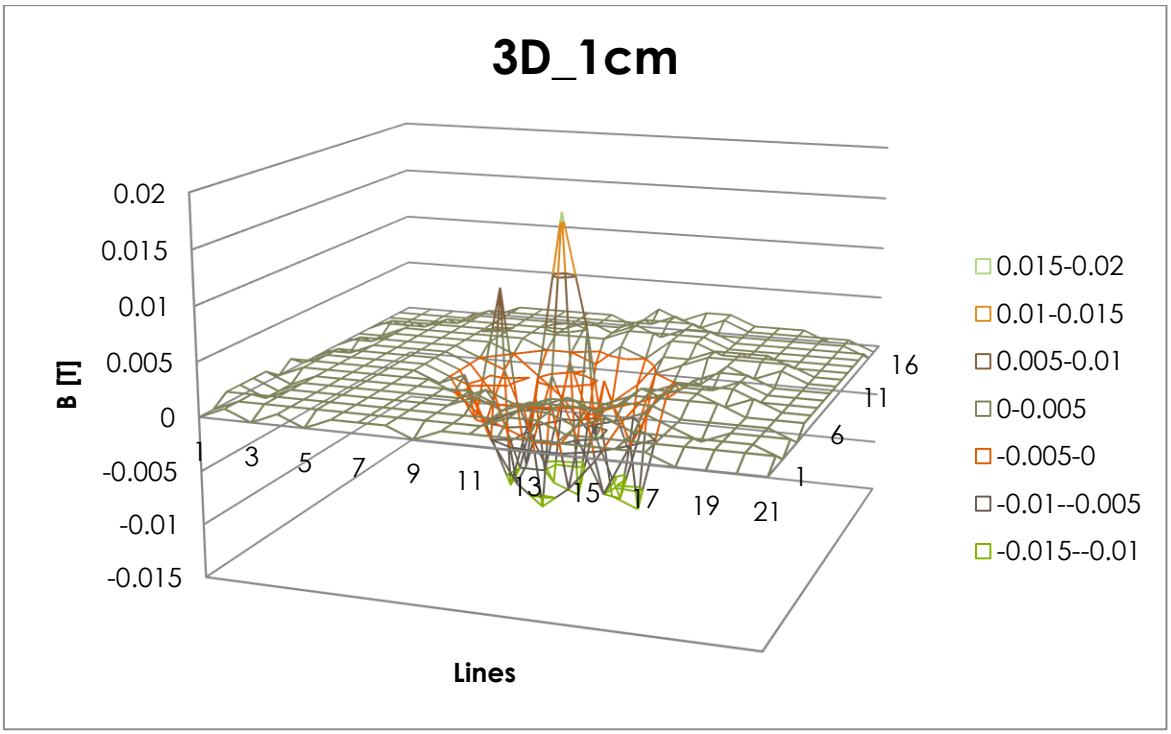

Figure 54: 3D image of B in 1cm distance from the magnets

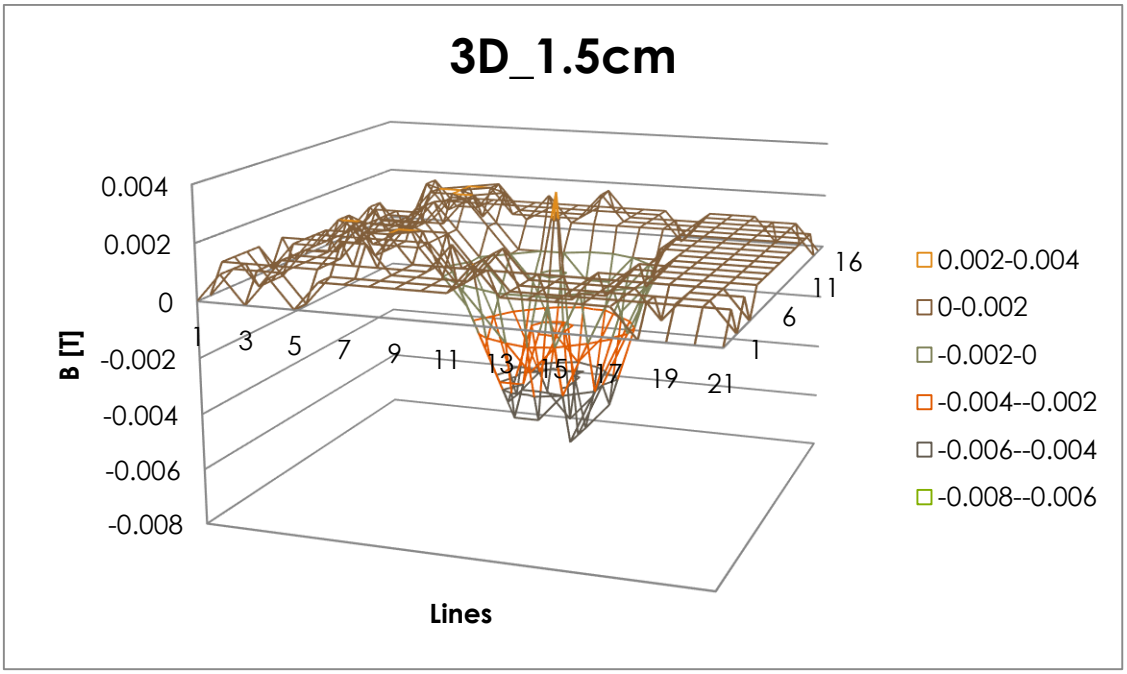

Figure 55: 3D image of B in 1,5cm distance from the magnets

10 Appendix B: Microscope images of deposited thin films and 3D profilometric views used for thickness determinations

.

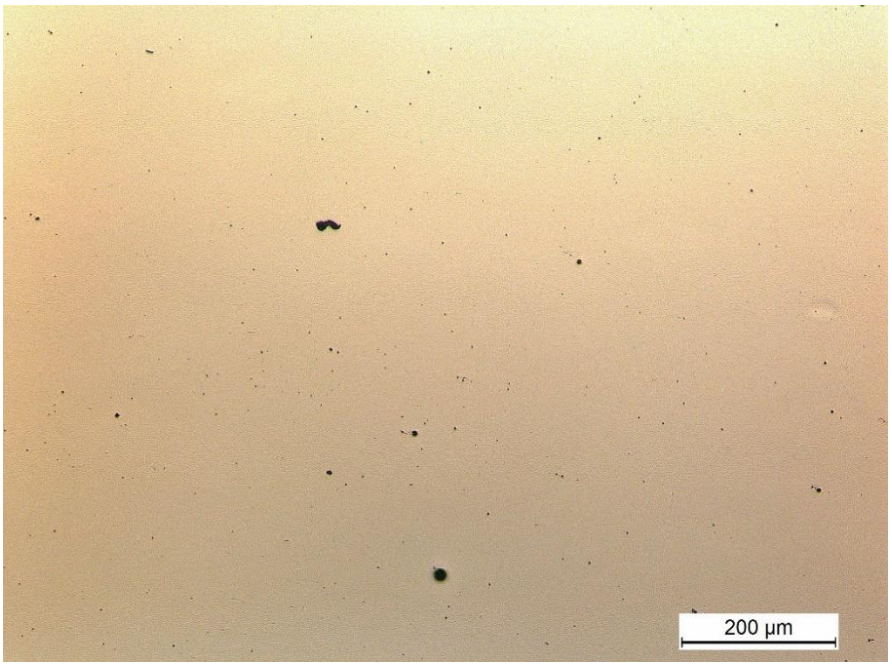

Figure 56: Microscope image of Al-thin film (B343_2) at 10x magnification

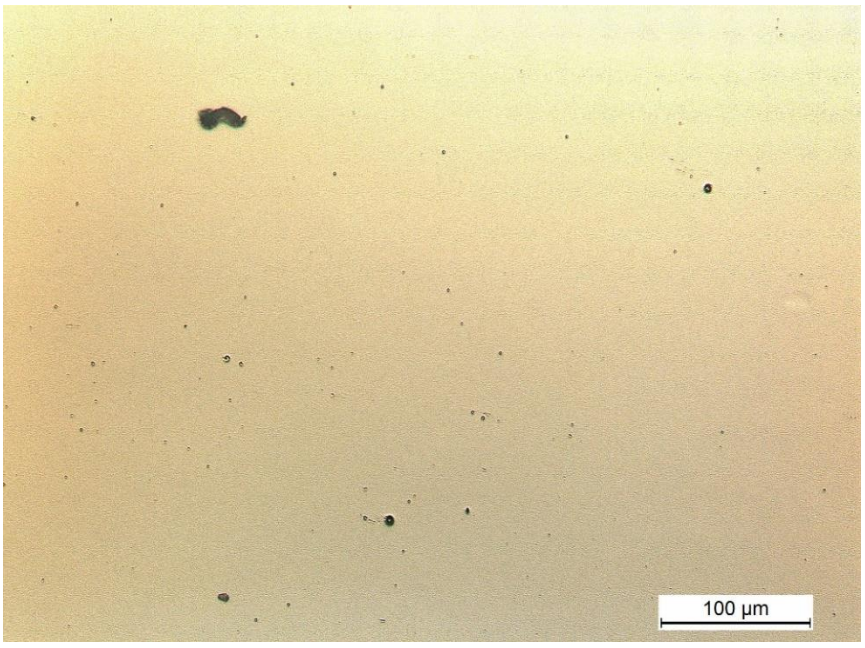

Figure 57: Microscope image of thin Al-film (B343_2) at 20x magnification

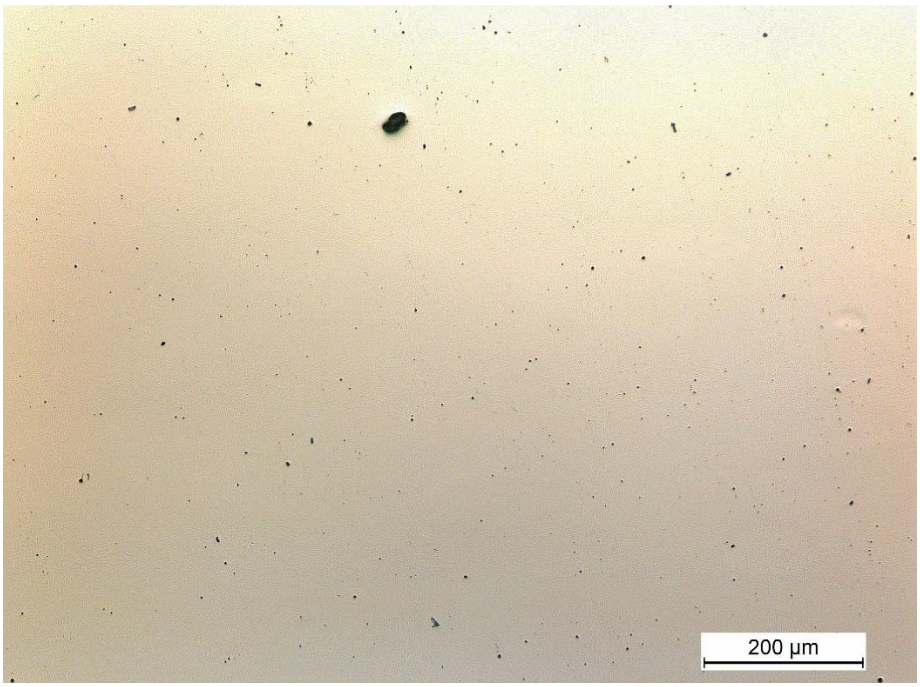

Figure 58: Microscope image of a thin Ti-film (B343_5) at 10x magnification

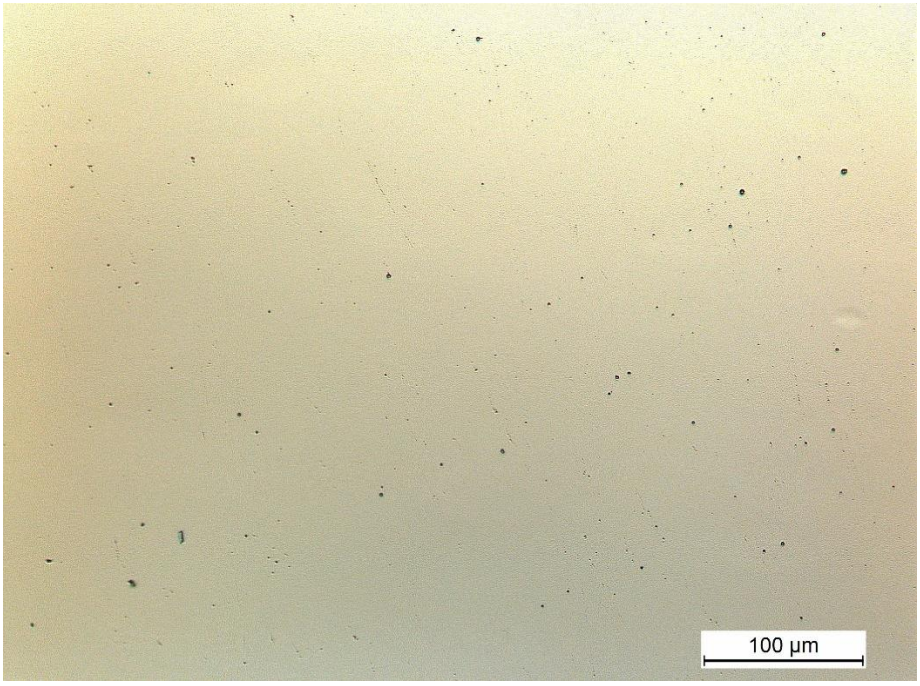

Figure 59: Microscope image of a thin Ti-film (B343_5) at 20x magnification

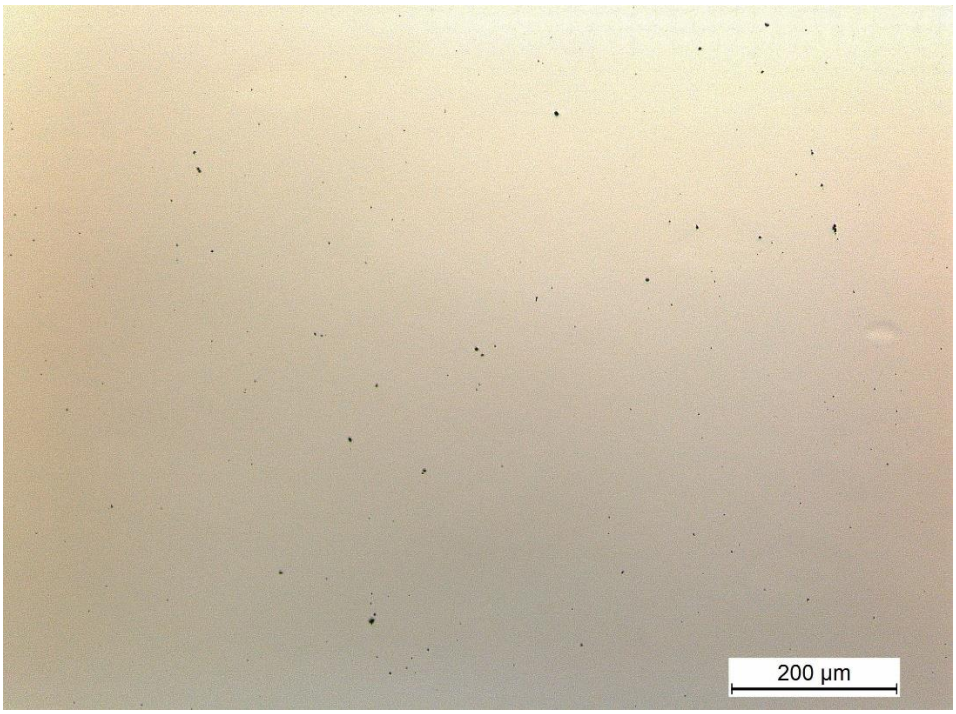

Figure 60: Microscope image of a thin Ti-film (B343_6) at 10x magnification

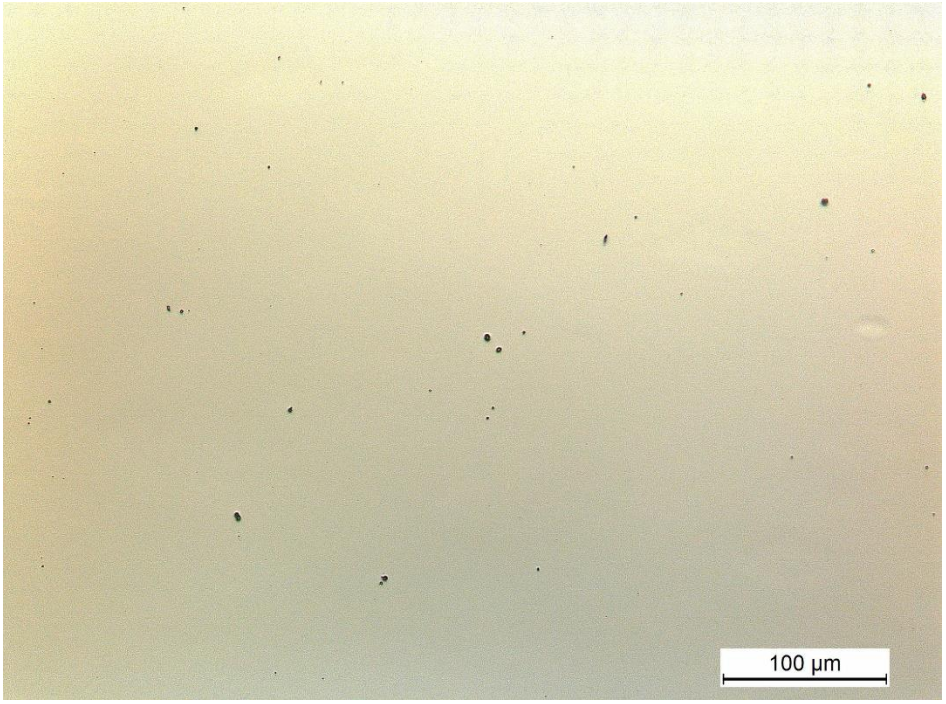

Figure 61: Microscope image of a thin Ti-film (B343_6) at 20x magnification

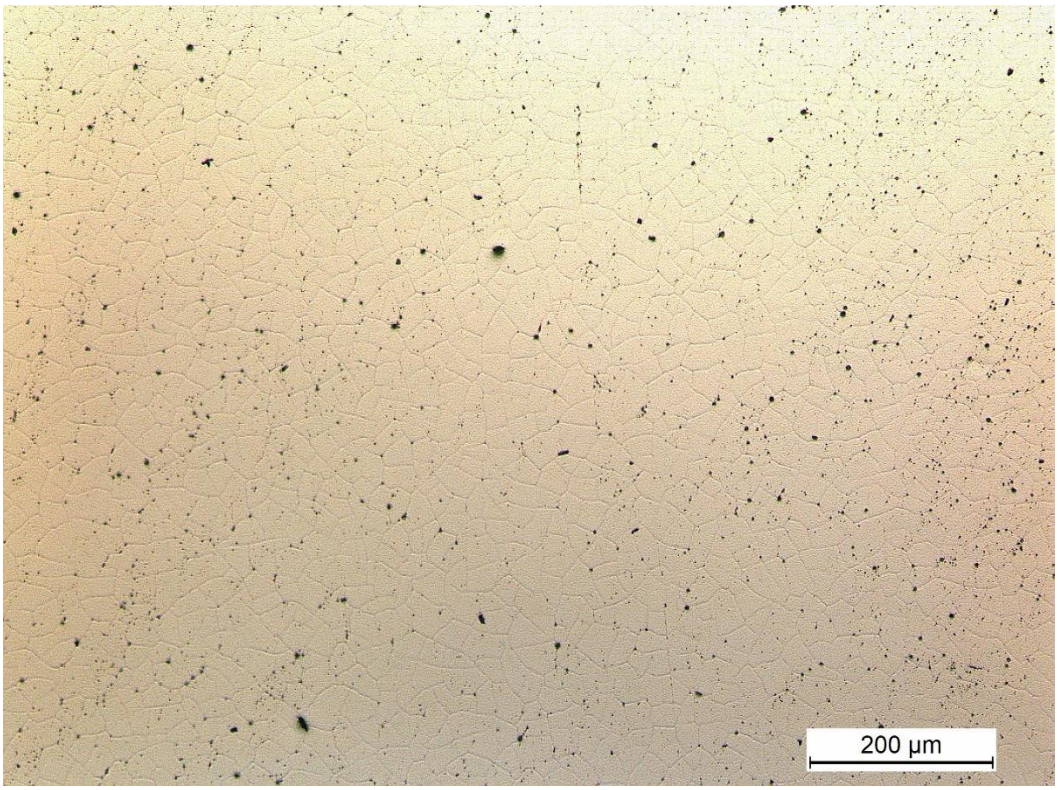

Figure 62: Microscope image of a thin Ti-film (B343_7) at 10x magnification

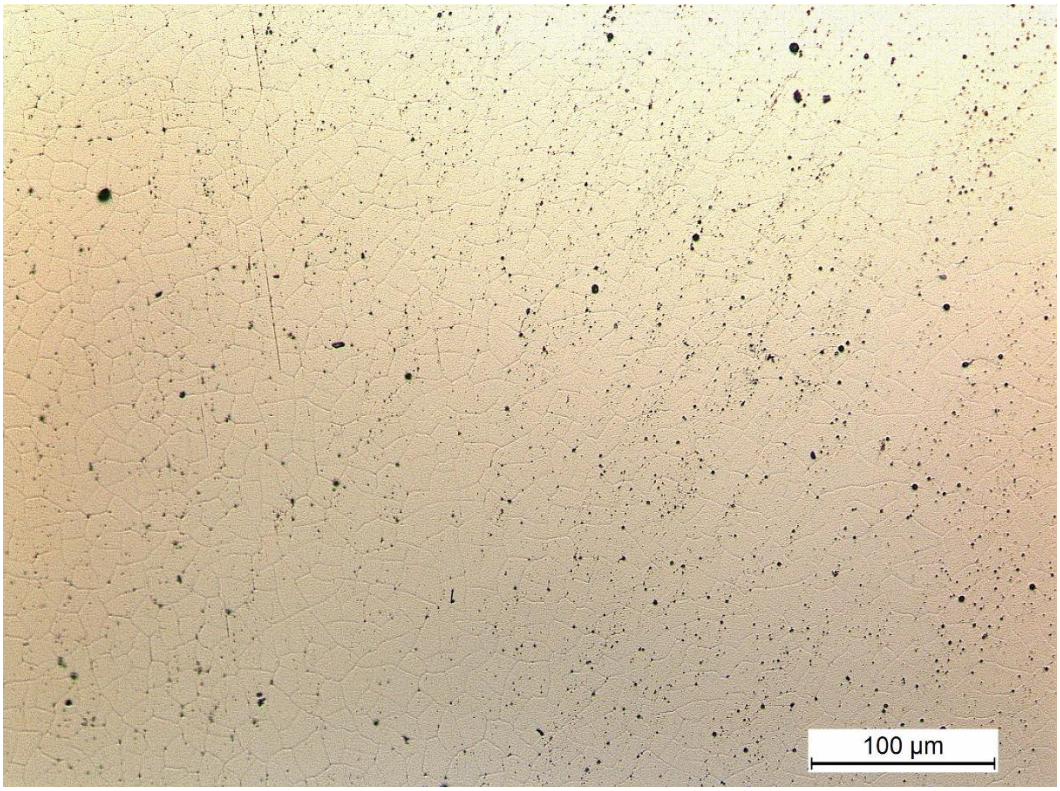

Figure 63: Microscope image of thin Ti-film (B343_7) at 20x magnification

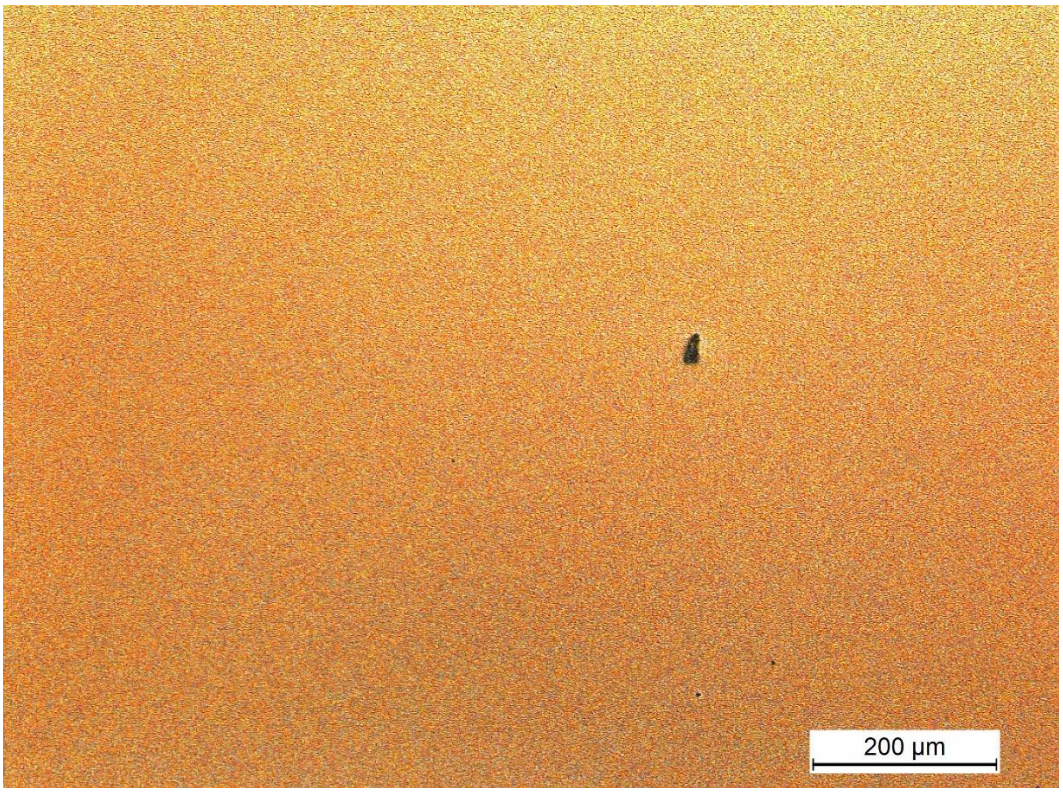

Figure 64: Microscope picture of a thin Al-film (B343_8) at 10x magnification

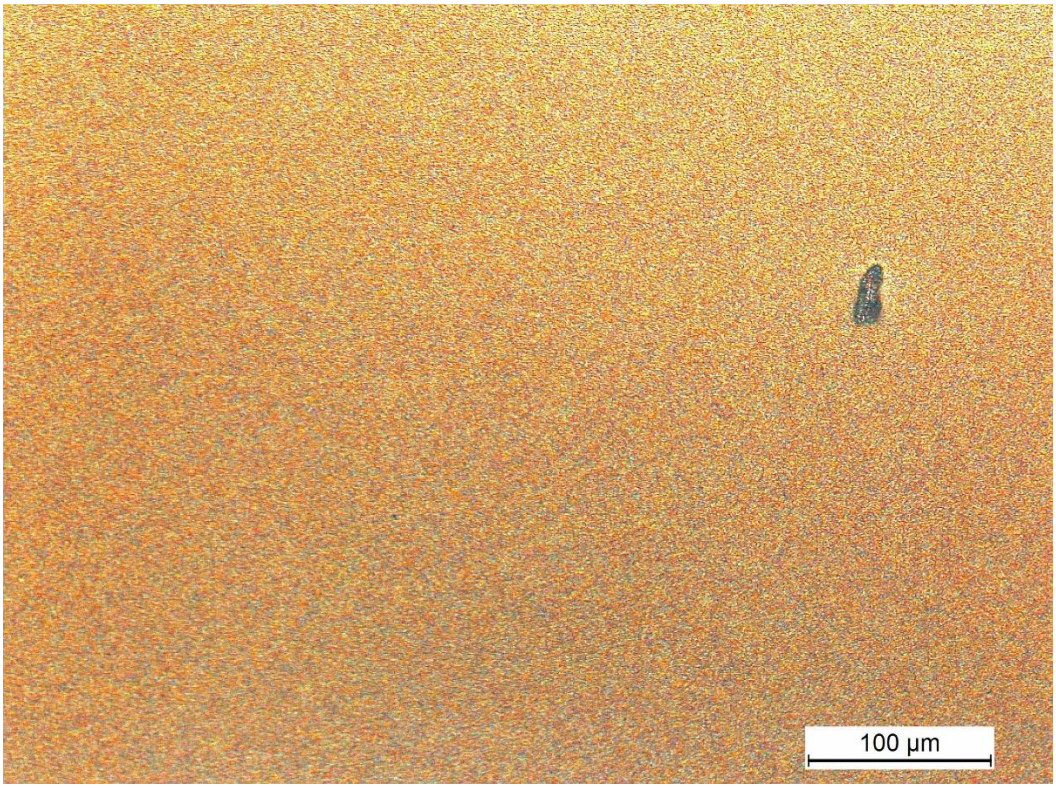

Figure 65: Microscope image of a thin Al-film (B343_8) at 20x magnification

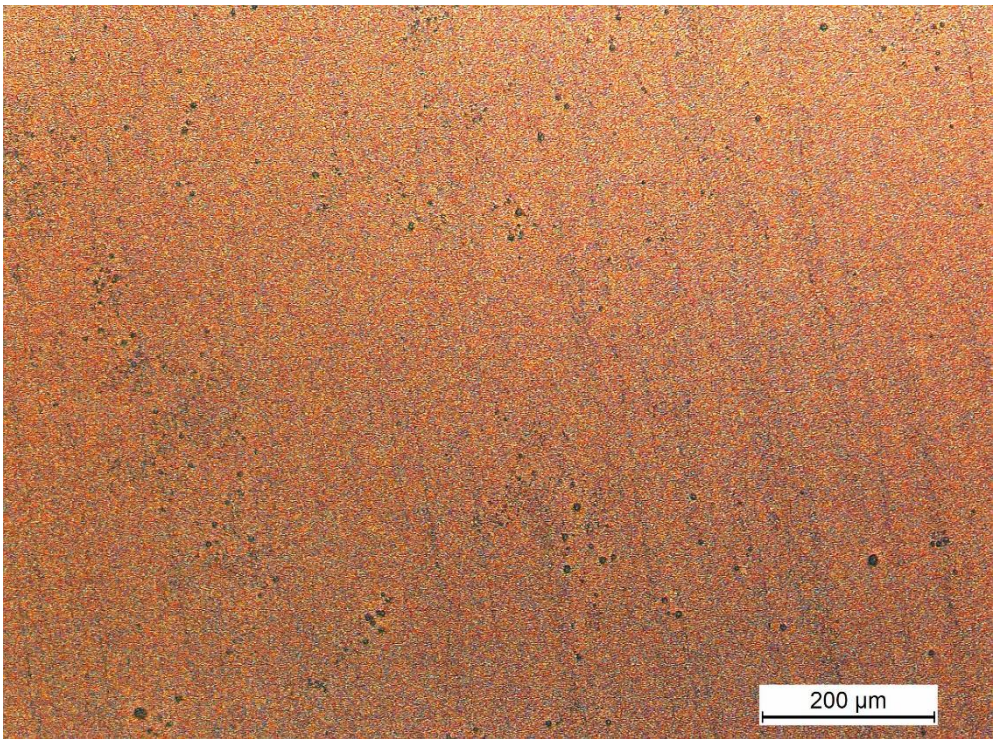

Figure 66: Microscope image of a thin Ti-film (B343_9) at 10x magnification

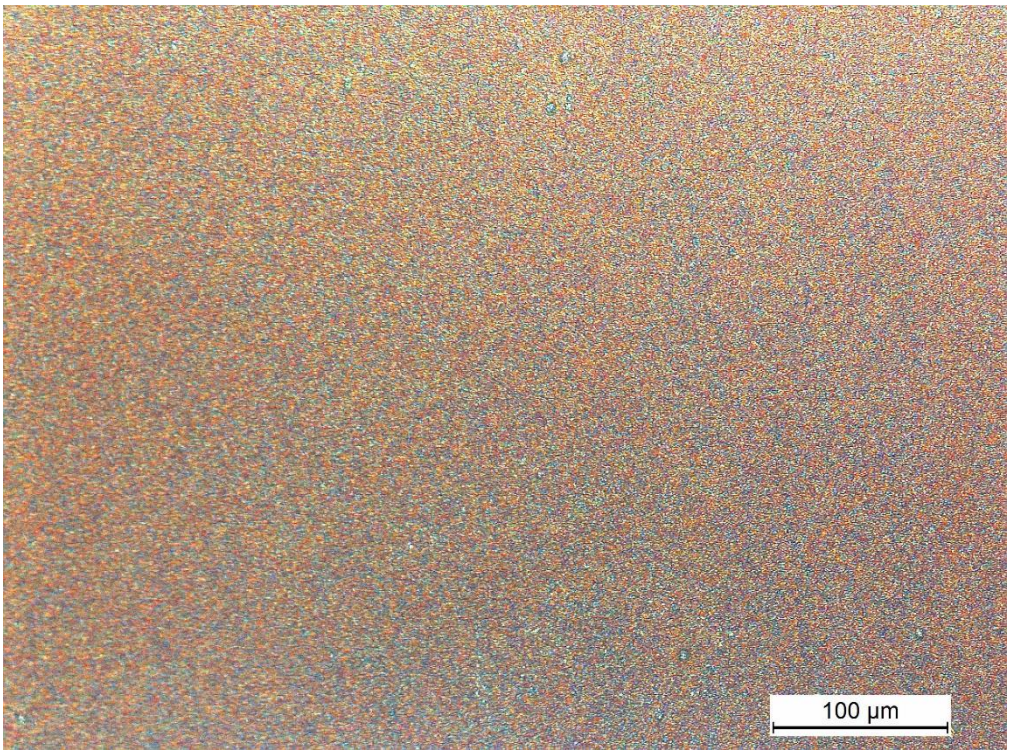

Figure 67: Microscope image of a thin Ti-film (B343_9) 20x magnification

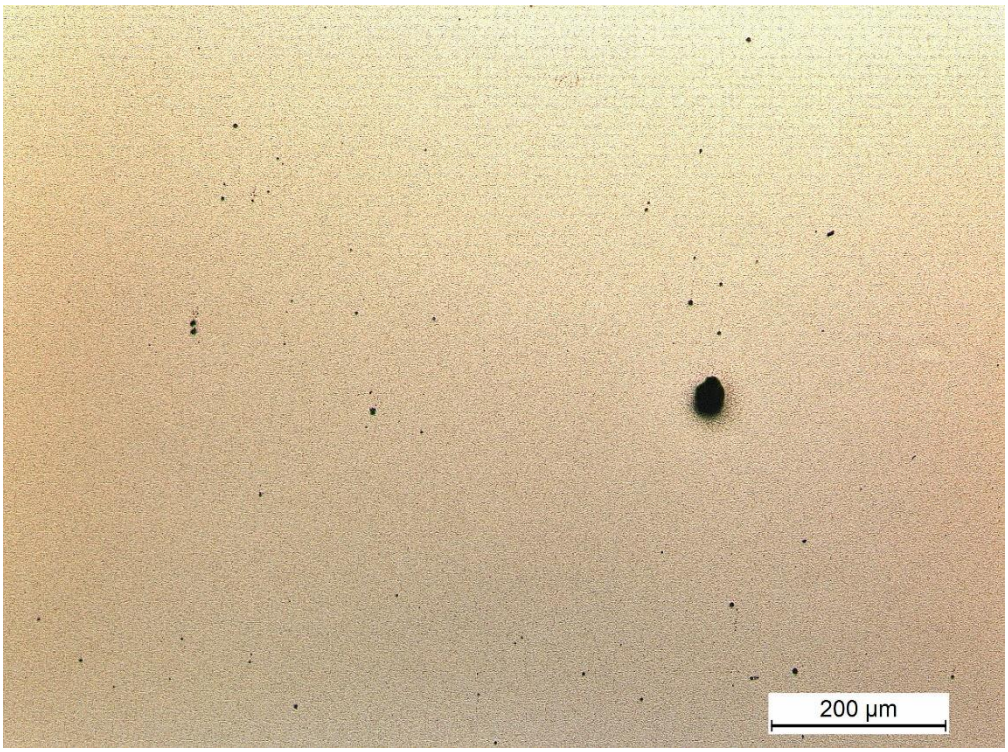

Figure 68: Microscope image of a thin Ti-film (B343_10) at 10x magnification

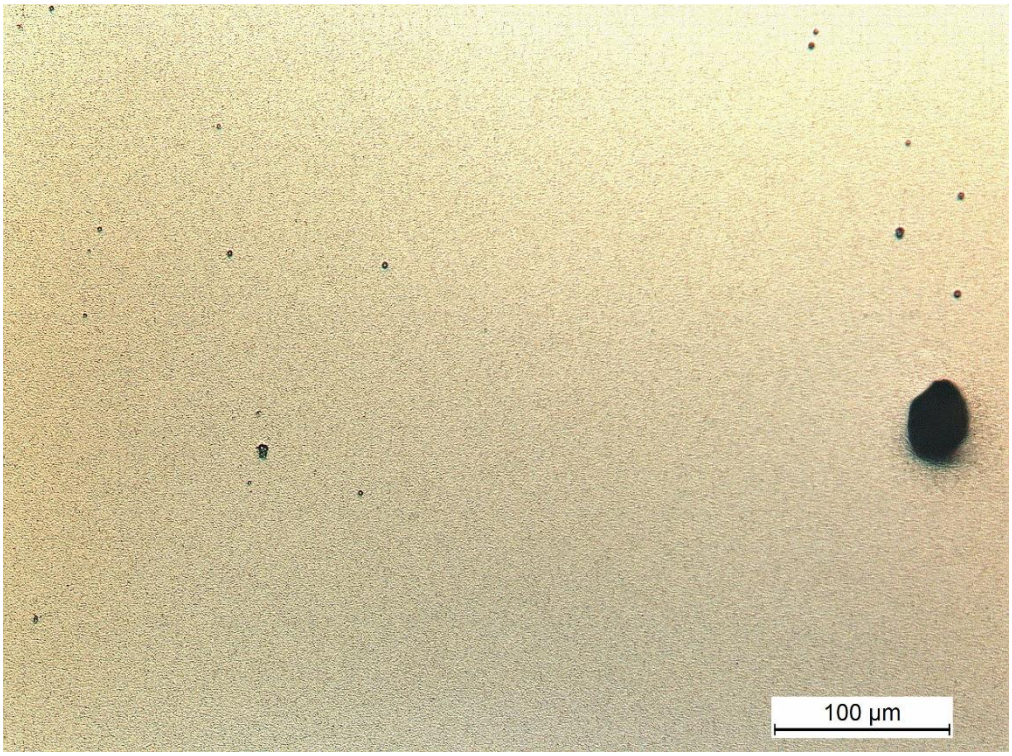

Figure 69: Microscope image of a thin Ti-film (B343_10) 20x magnification

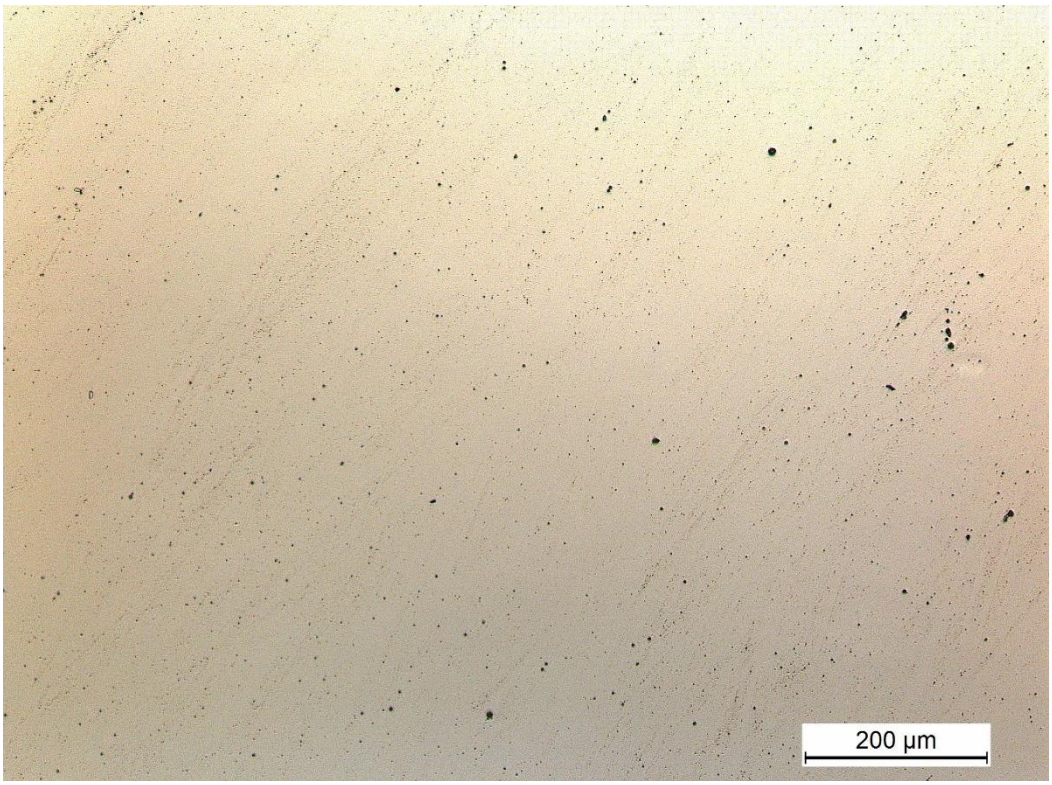

Figure 70: Microscope image of a thin TI-film (B343_11) 10x magnification

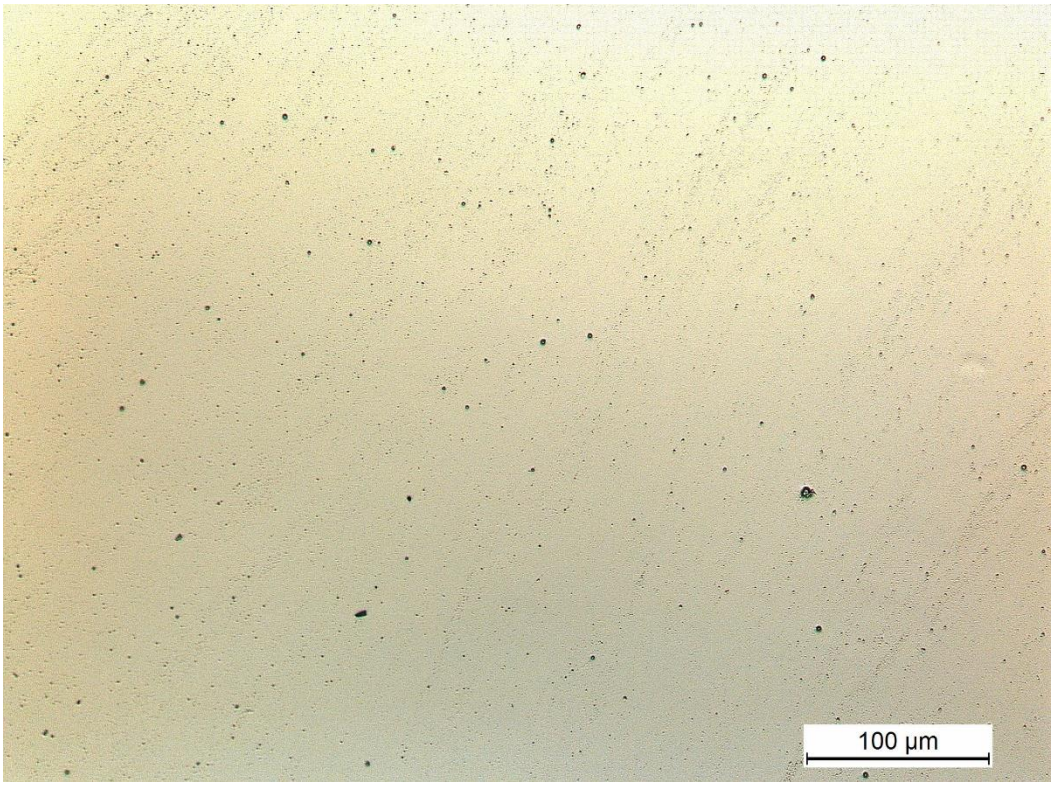

Figure 71: Microscope image of a thin Ti-film (B343_11) at 20x magnification

.

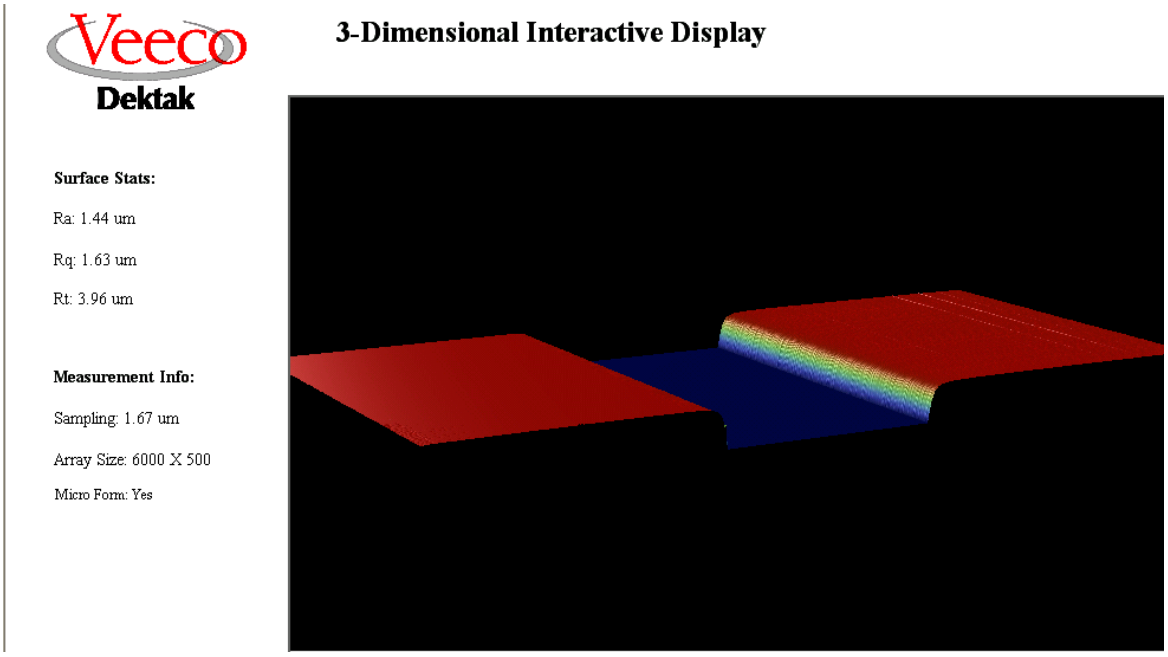

Figure 72: 3D mapping of B343_2

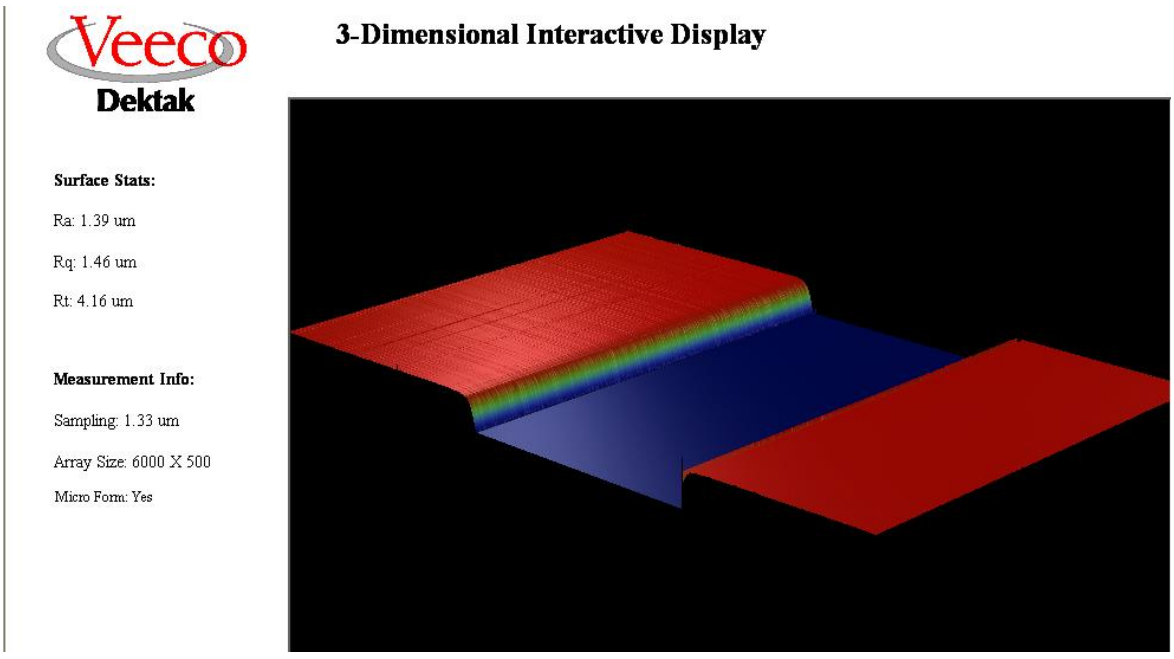

Figure 73: 3D mapping of B343_5

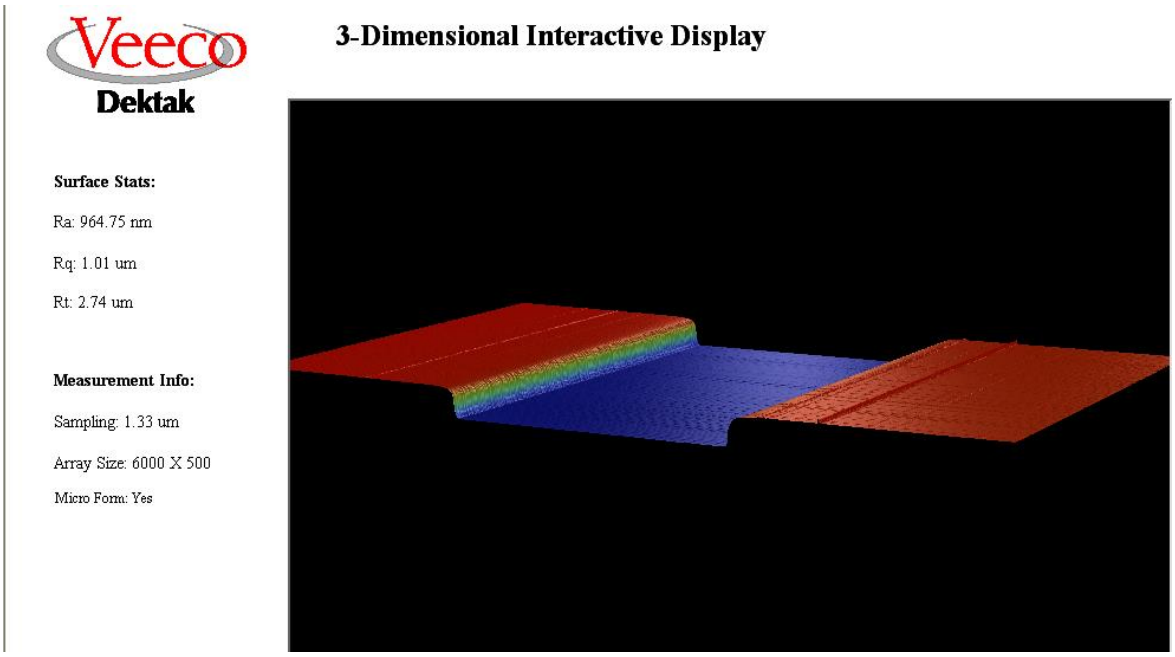

Figure 74: 3D mapping of B343_6

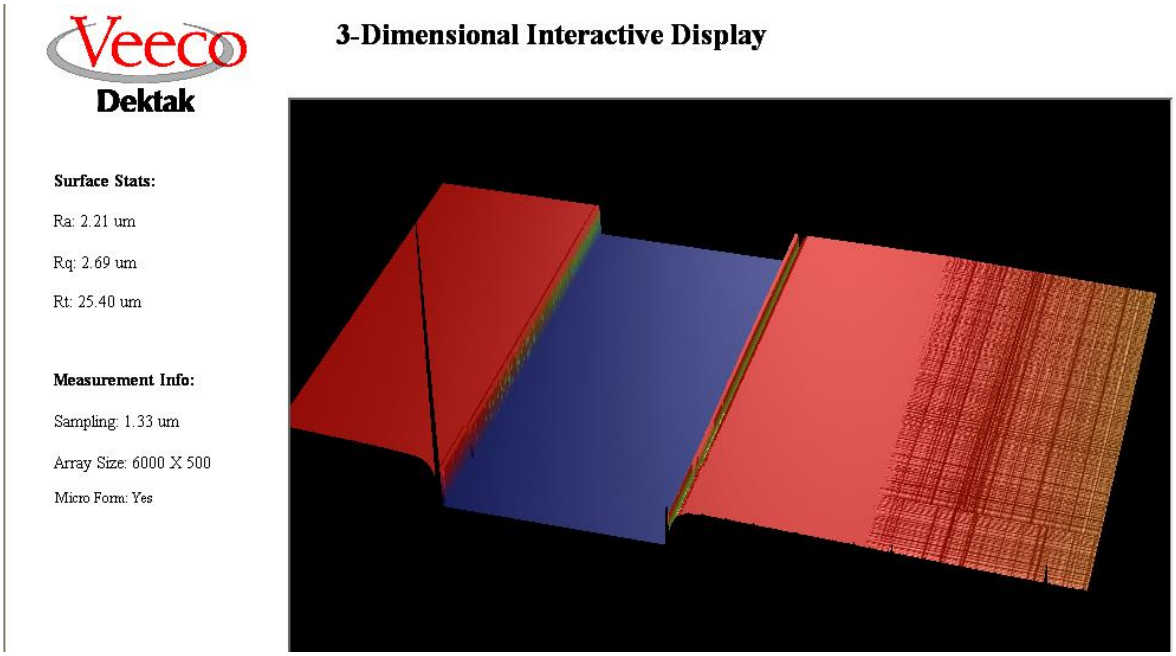

Figure 75: 3D mapping of B343_7

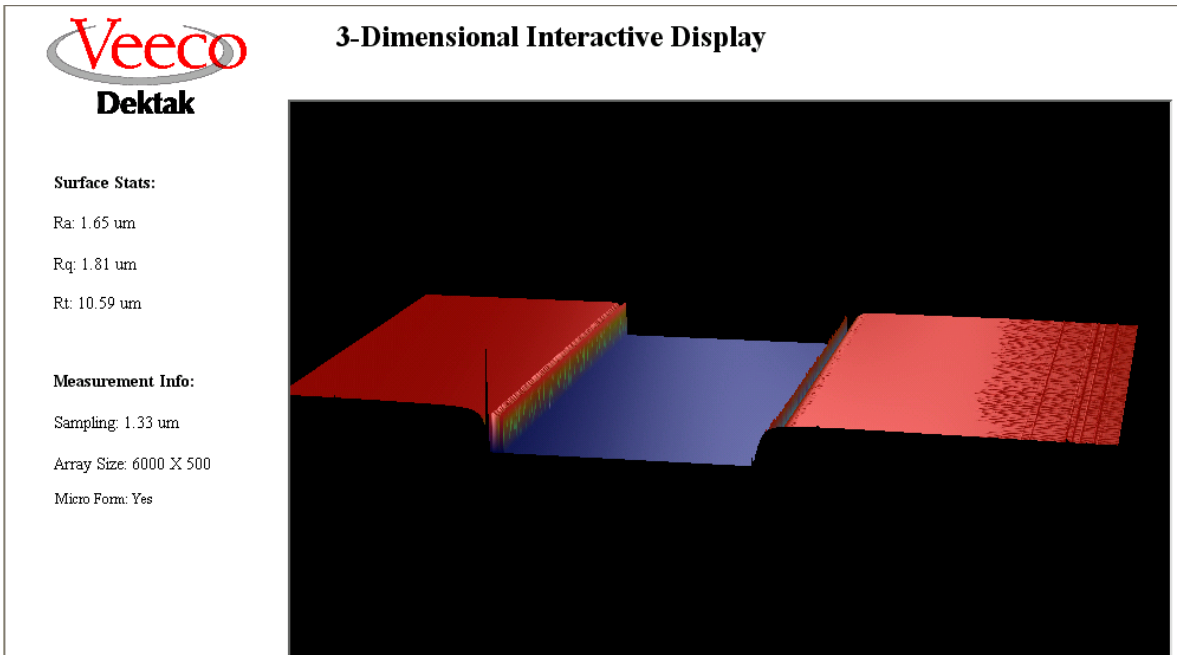

Figure 76: 3D mapping of B343_9

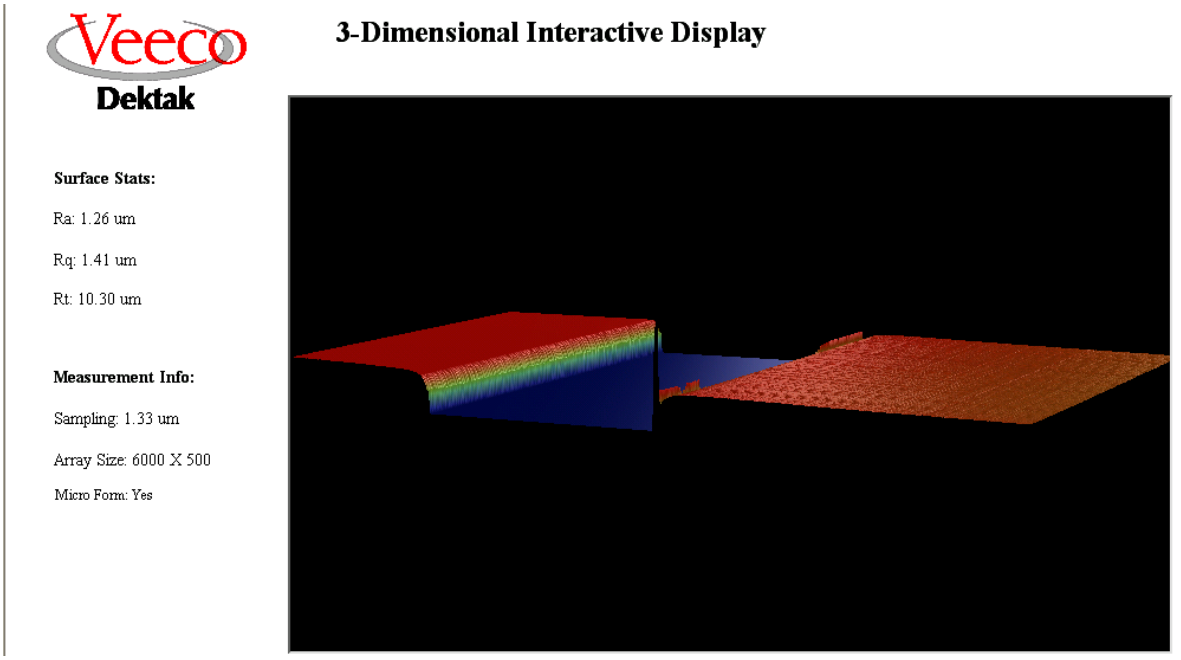

Figure 77:3D mapping of B343_10

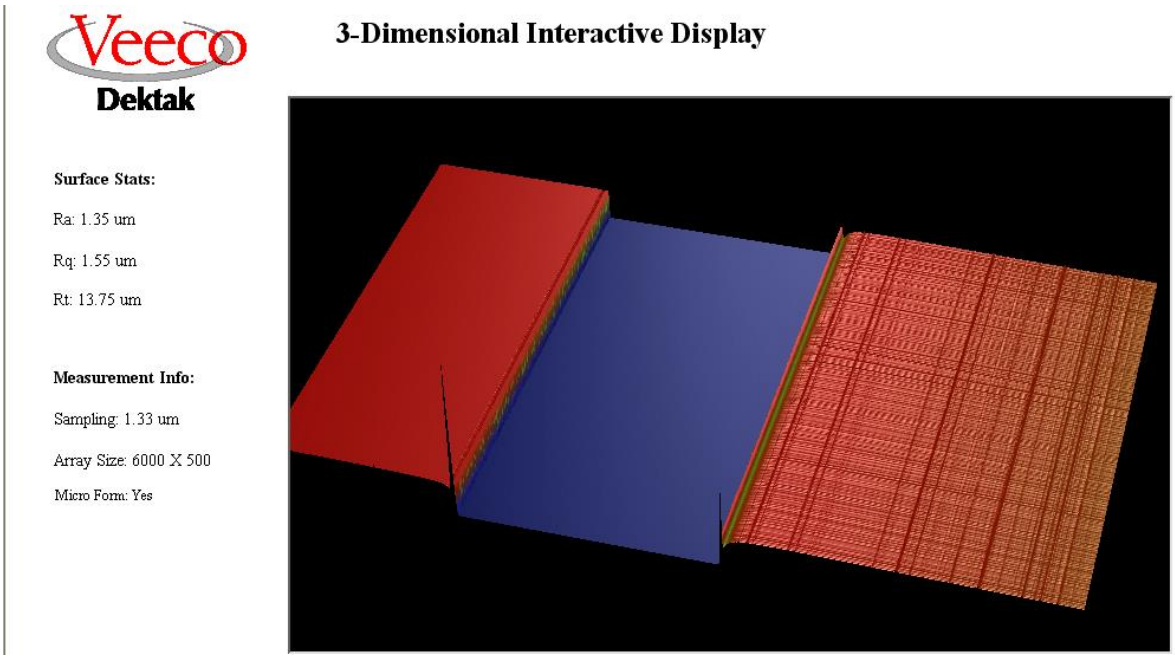

Figure 78:3D mapping of B343_11

11 Appendix C: Results of simulations

The number of sputtered particle on the substrate surface have been discussed in the thesis, but there are also further results of number of secondary particles on the substrate and of sputtered particles on the target.

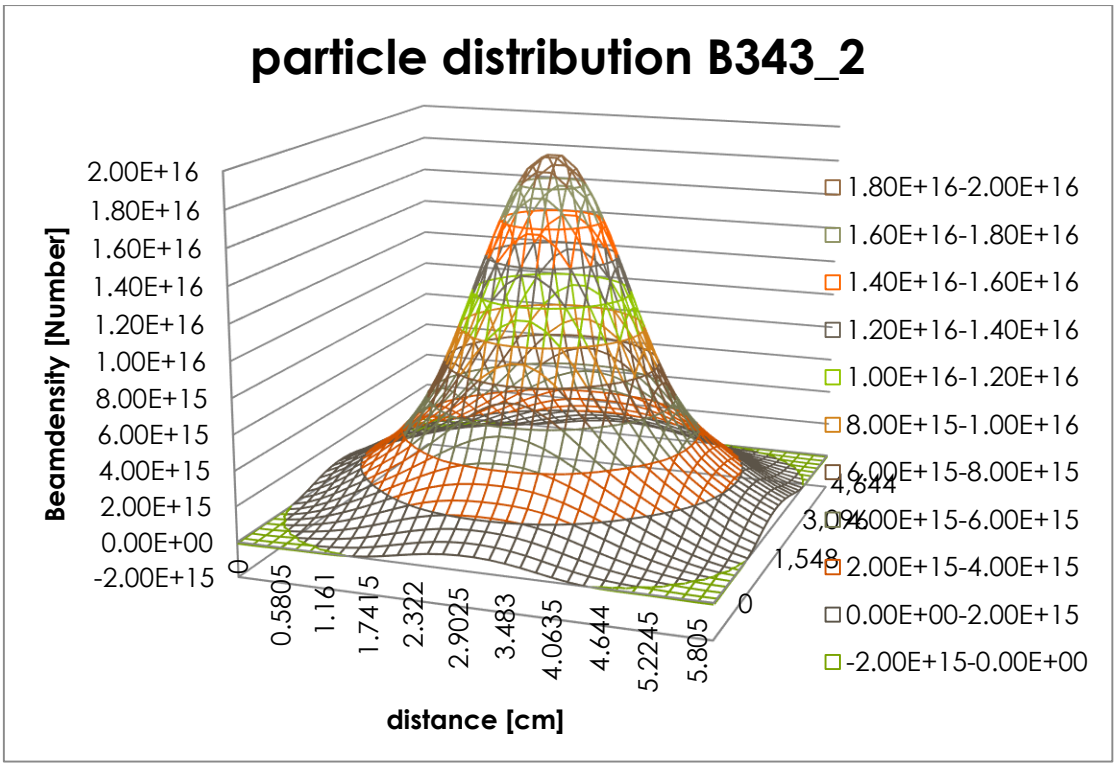

Figure 79: Distribution of secondary particles (calculation for experiment B343_2) on the substrate surface

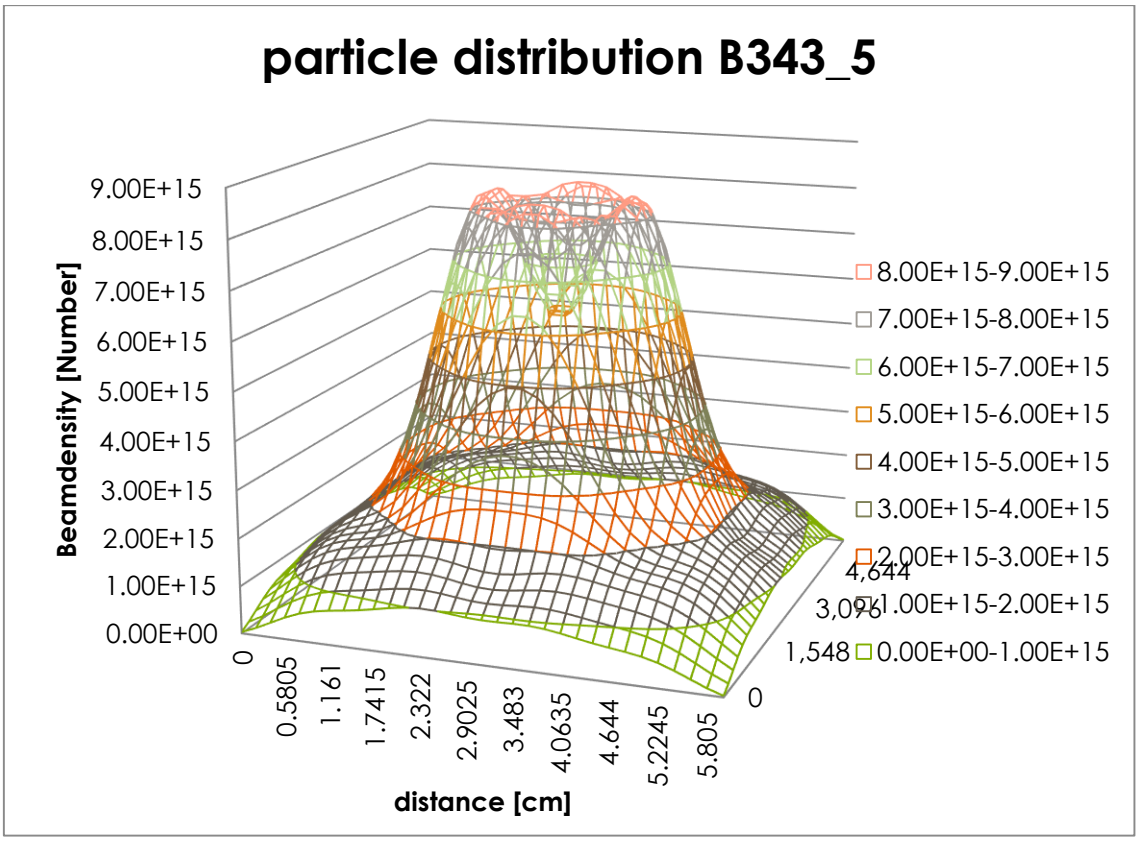

Figure 80: Distribution of secondary particles (calculation for experiment B343_5) on the substrate surface

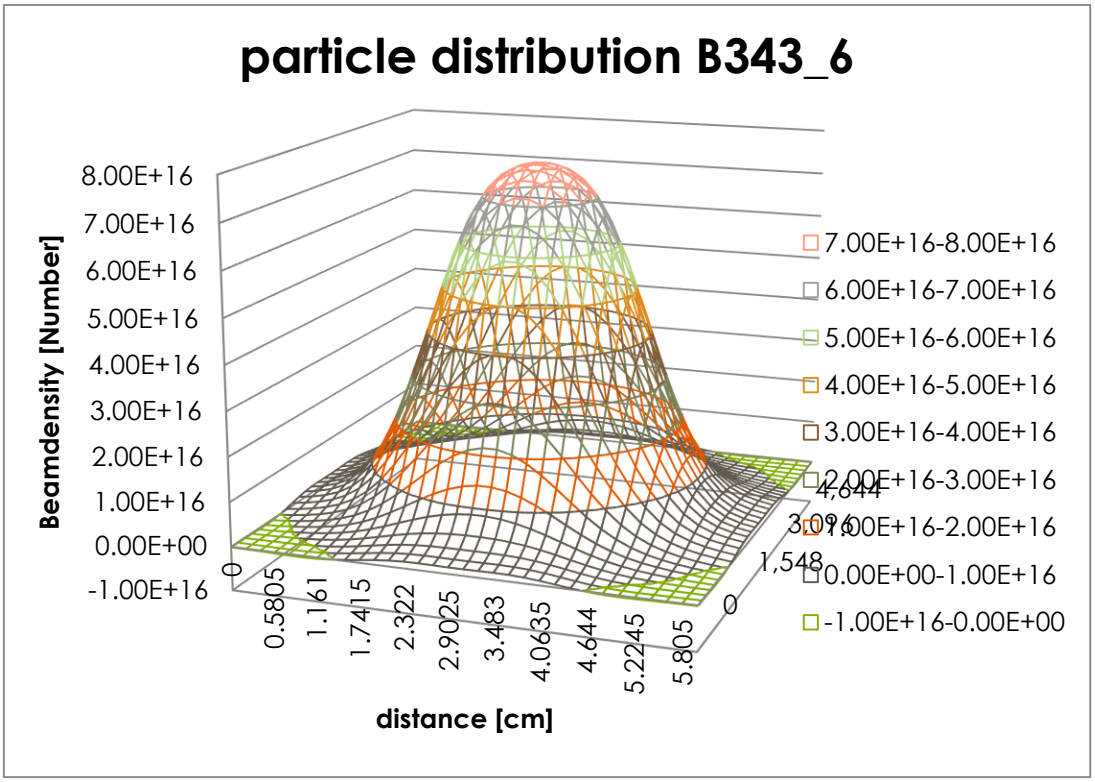

Figure 81: Distribution of secondary particles (calculation for experiment B343_6) on the substrate surface

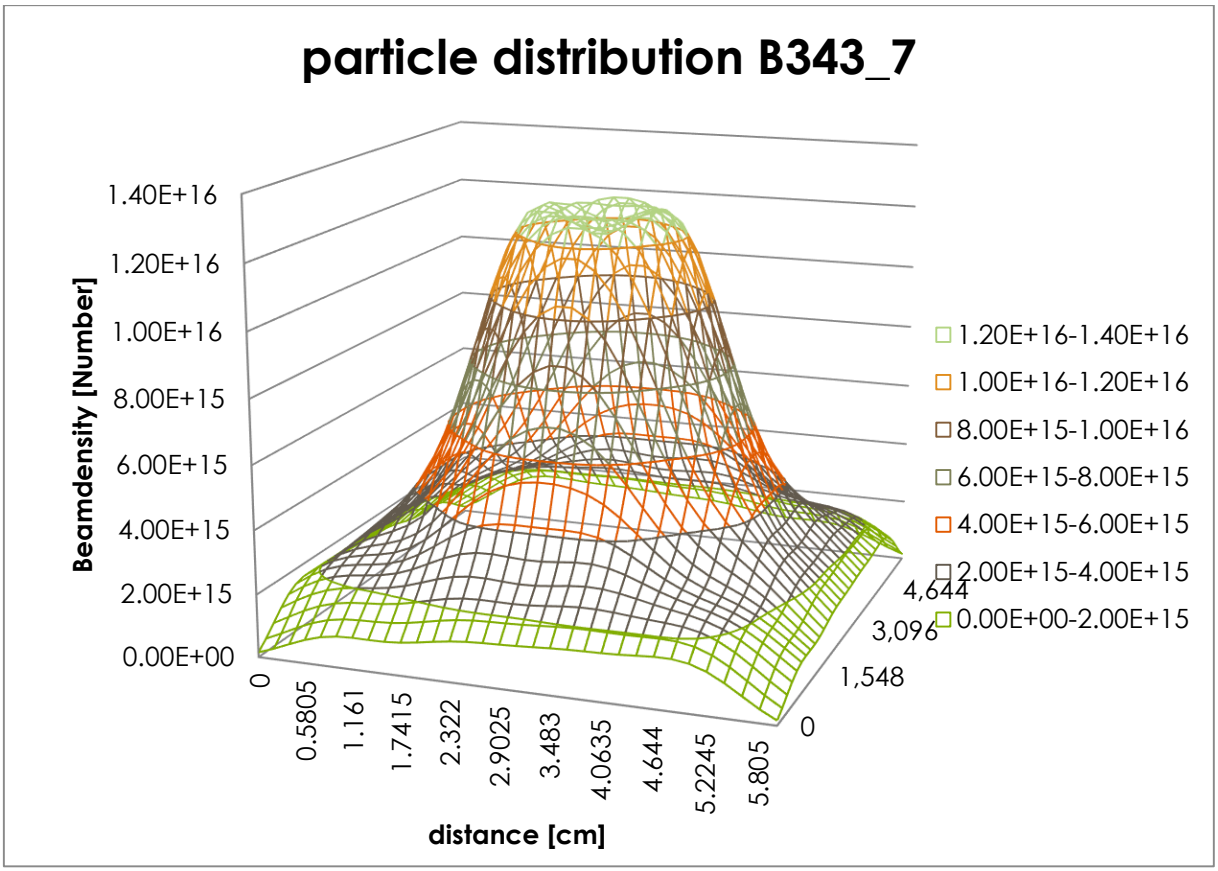

Figure 82: Distribution of secondary particles (calculation for experiment B343_7) on the substrate surface

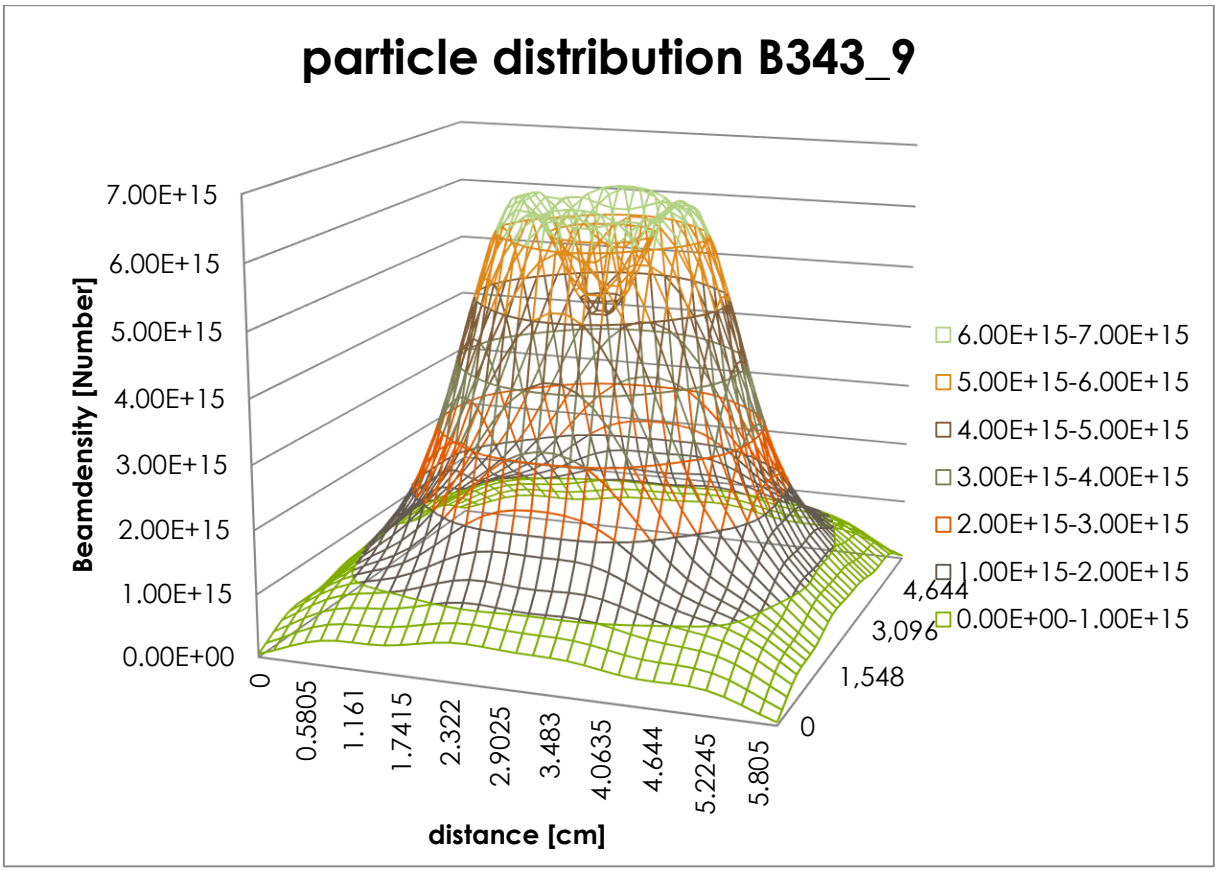

Figure 83: Distribution of secondary particles (calculation for experiment B343_9) on the substrate surface

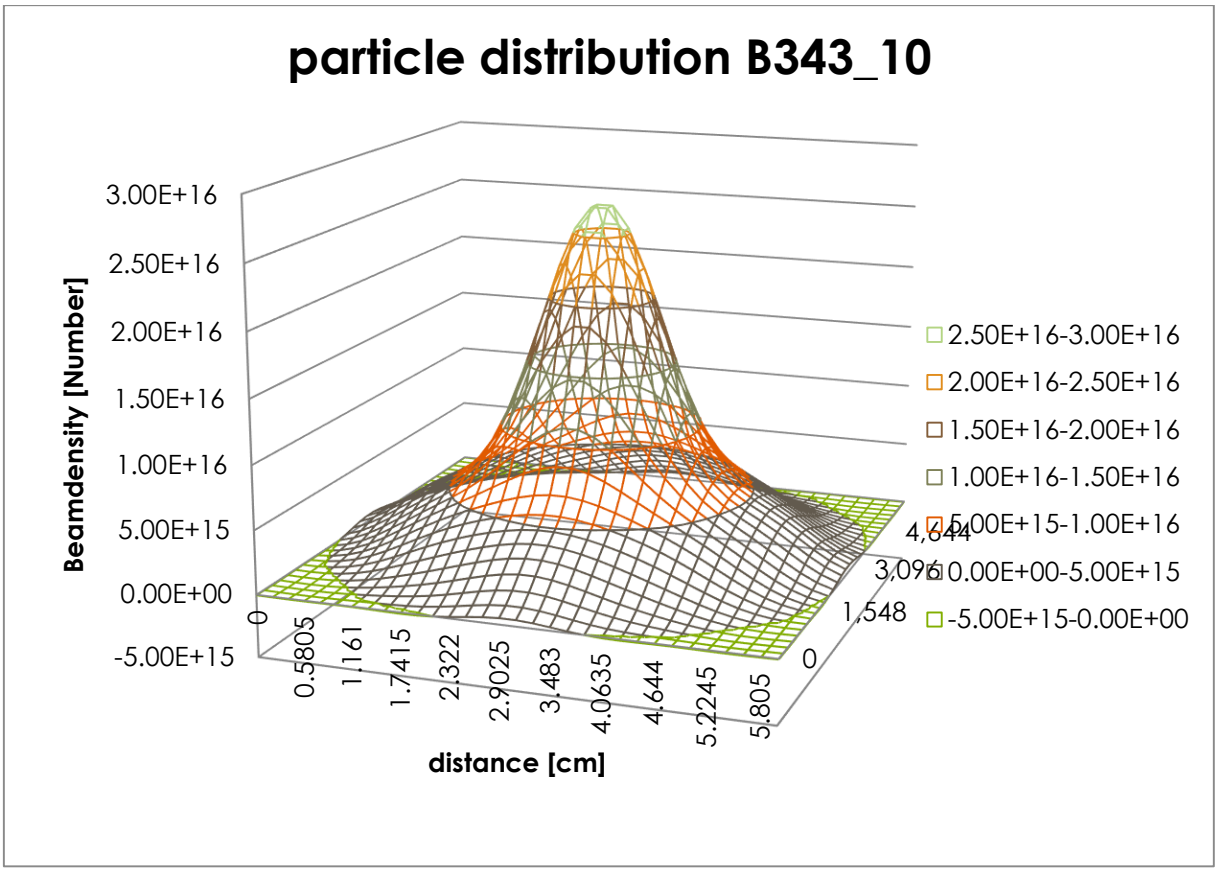

Figure 84: Distribution of secondary particles (calculation for experiment B343_10) on the substrate surface

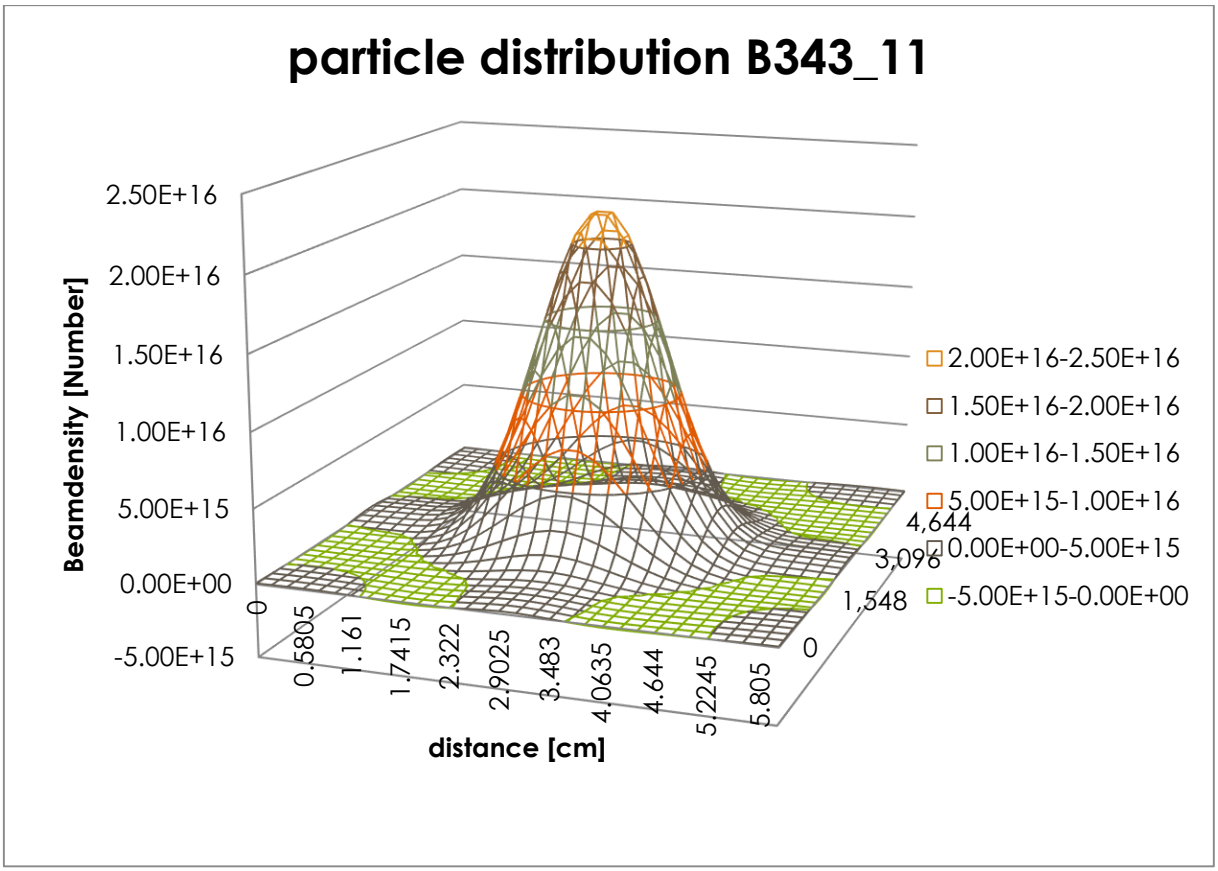

Figure 85: Distribution of secondary particles (calculation for experiment B343_11) on the substrate surface

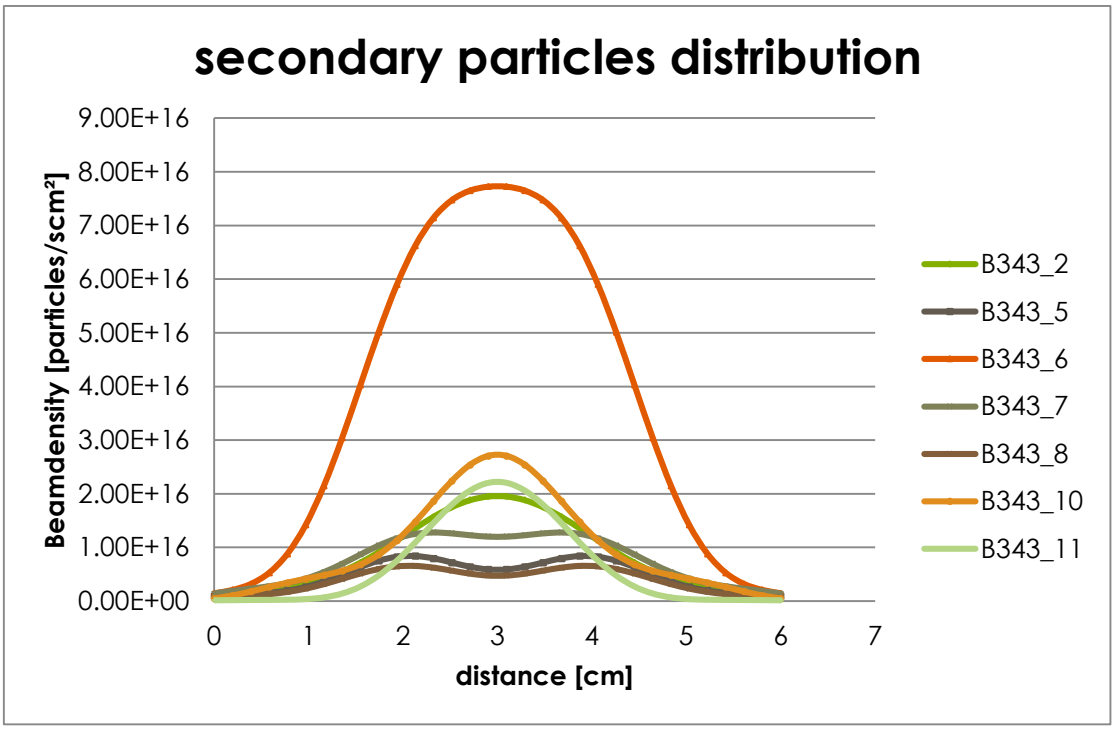

Figure 86: Comparison of the secondary particle distribution of all simulated experiments.

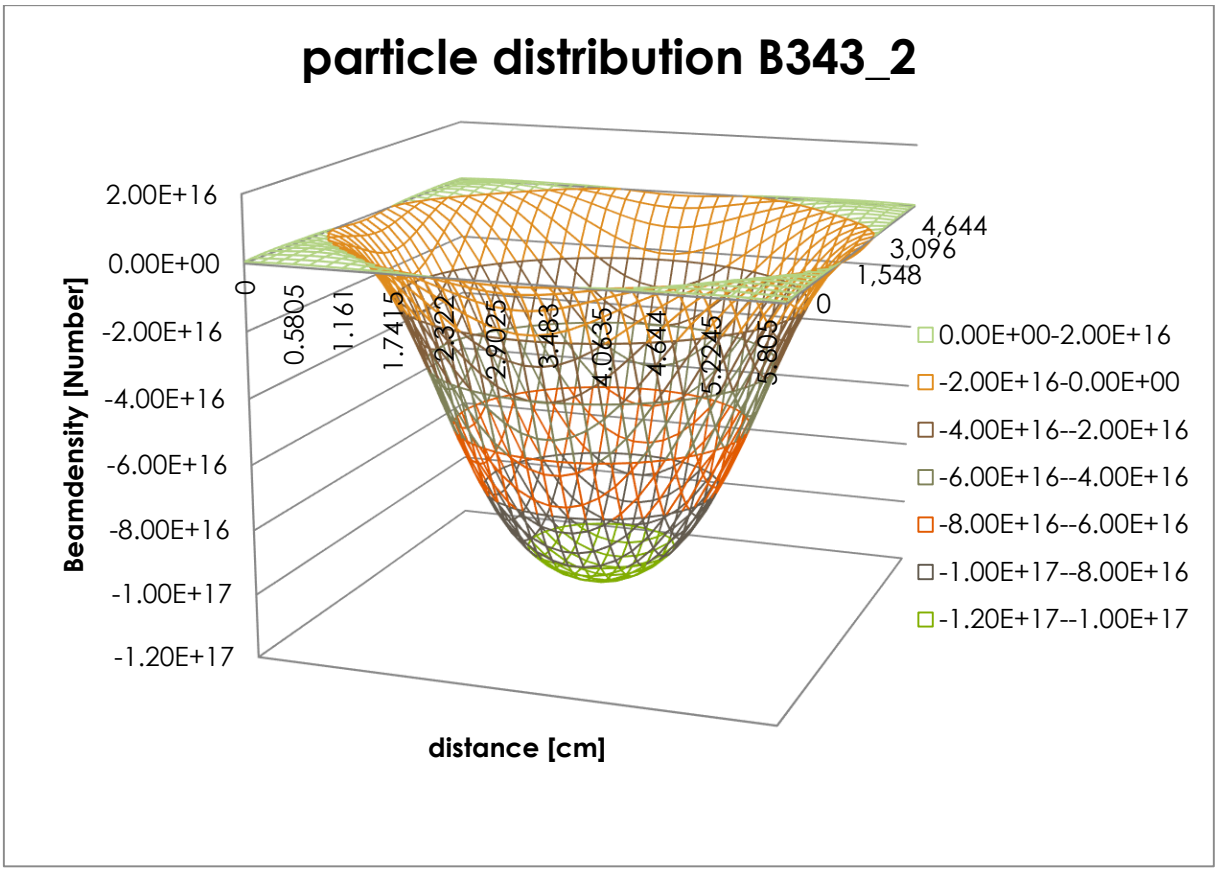

Figure 87: Distribution of sputtered particles (calculation experiment B343_2) on the target surface

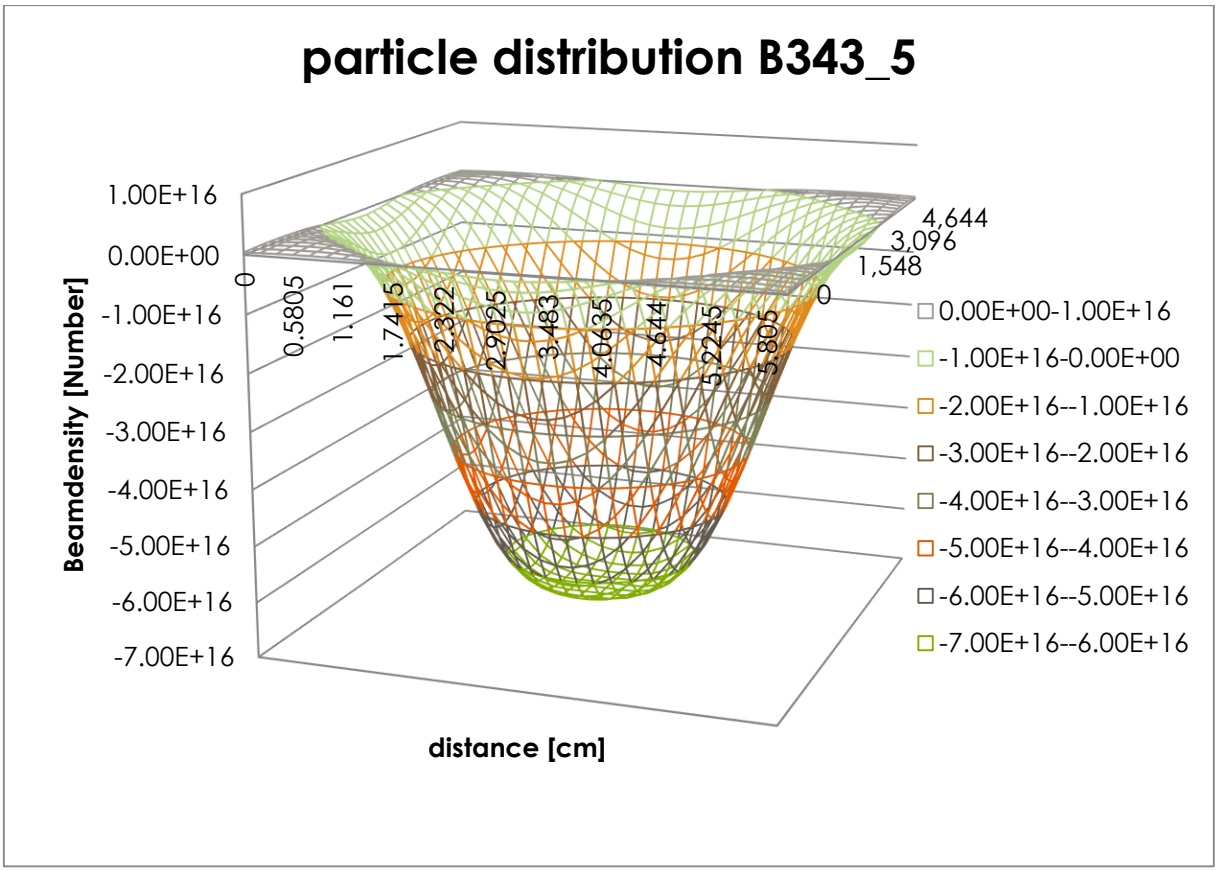

Figure 88: Distribution of sputtered particles (calculation experiment B343_5) on the target surface

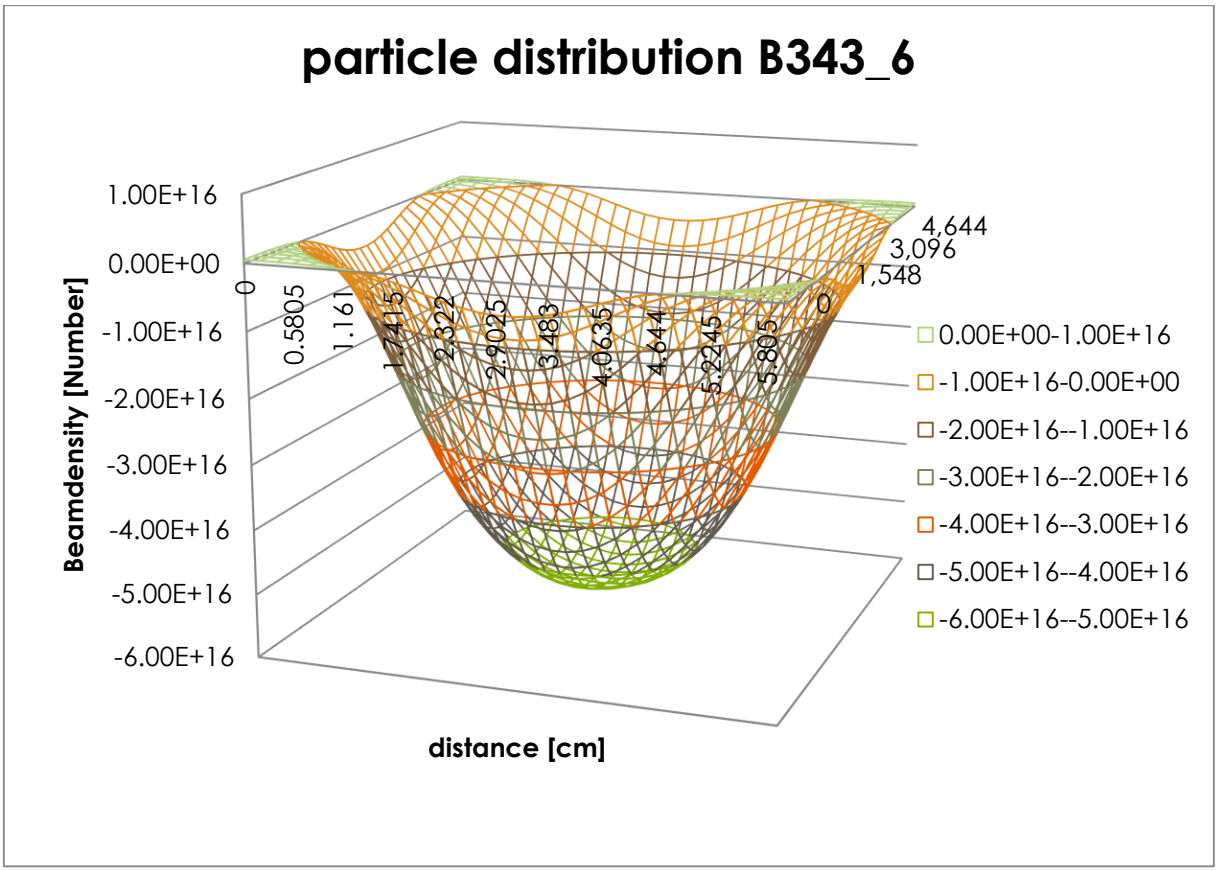

Figure 89: Distribution of sputtered particles (calculation experiment B343_6) on the target surface

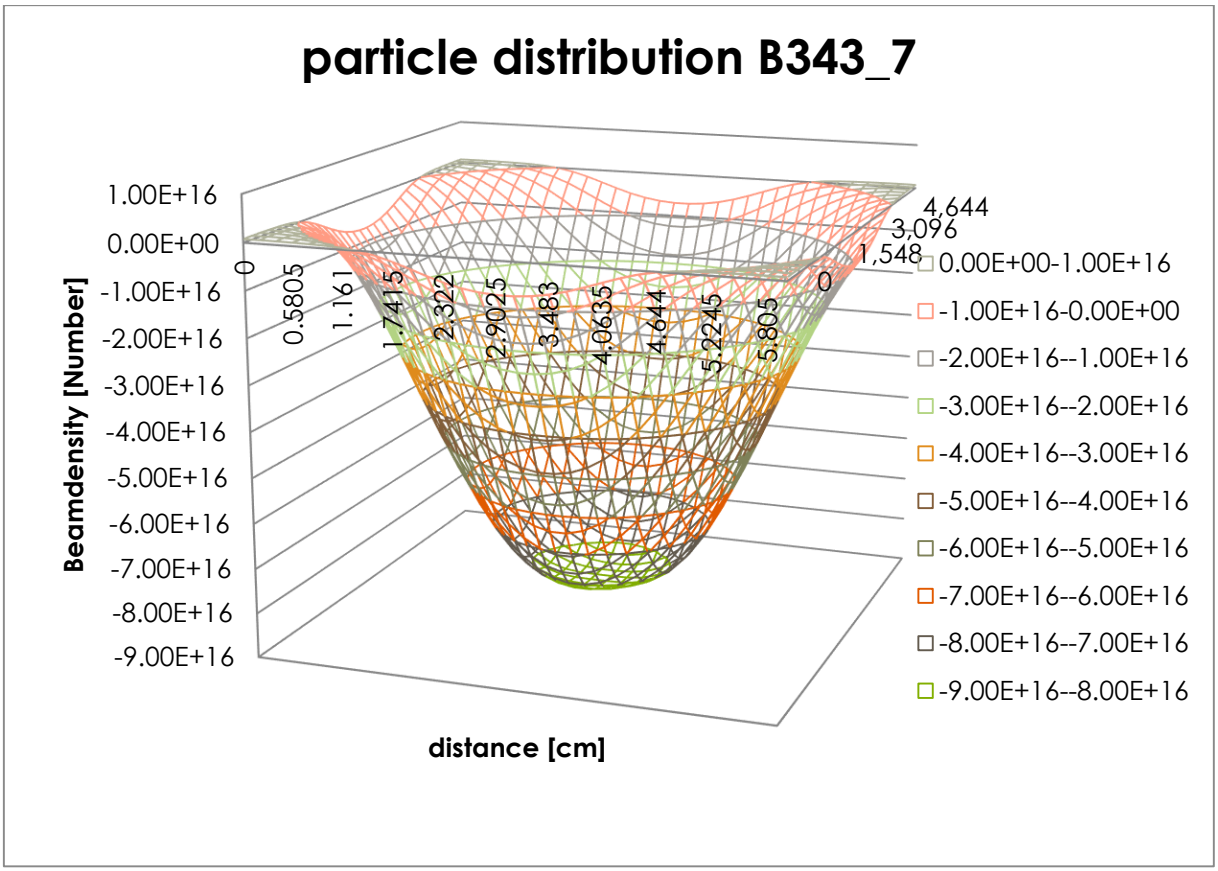

Figure 90: Distribution of sputtered particles (calculation experiment B343_7) on the target surface

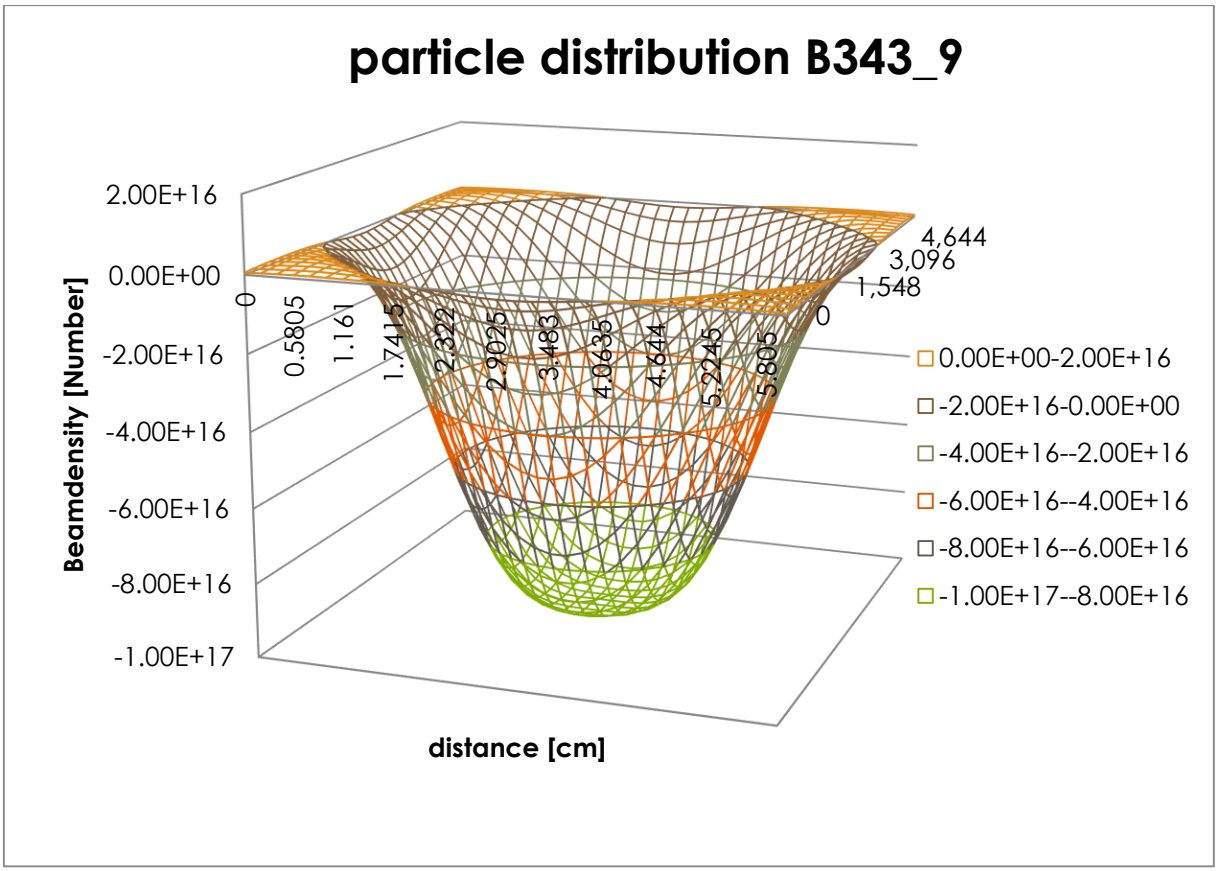

Figure 91: Distribution of sputtered particles (calculation experiment B343_9) on the target surface

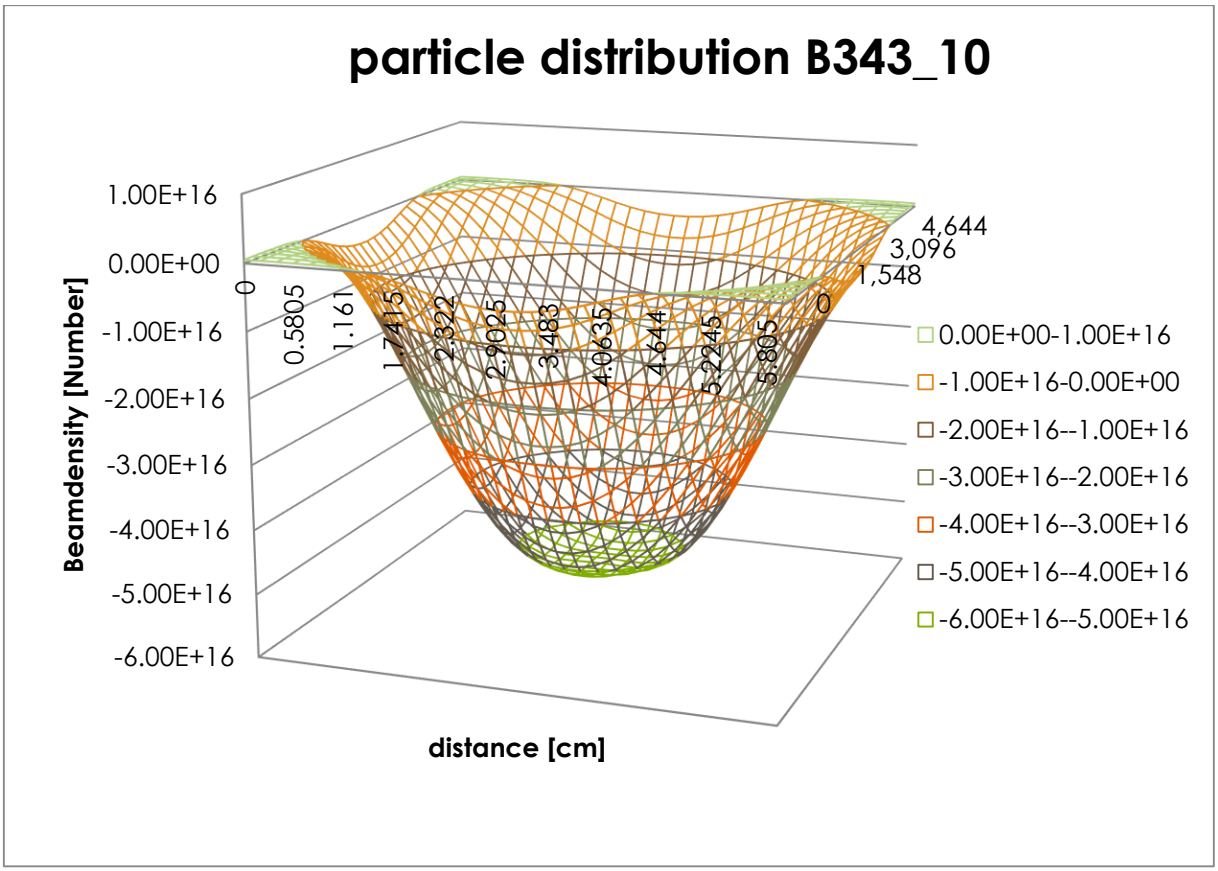

Figure 92: Distribution of sputtered particles (calculation experiment B343_10) on the target surface

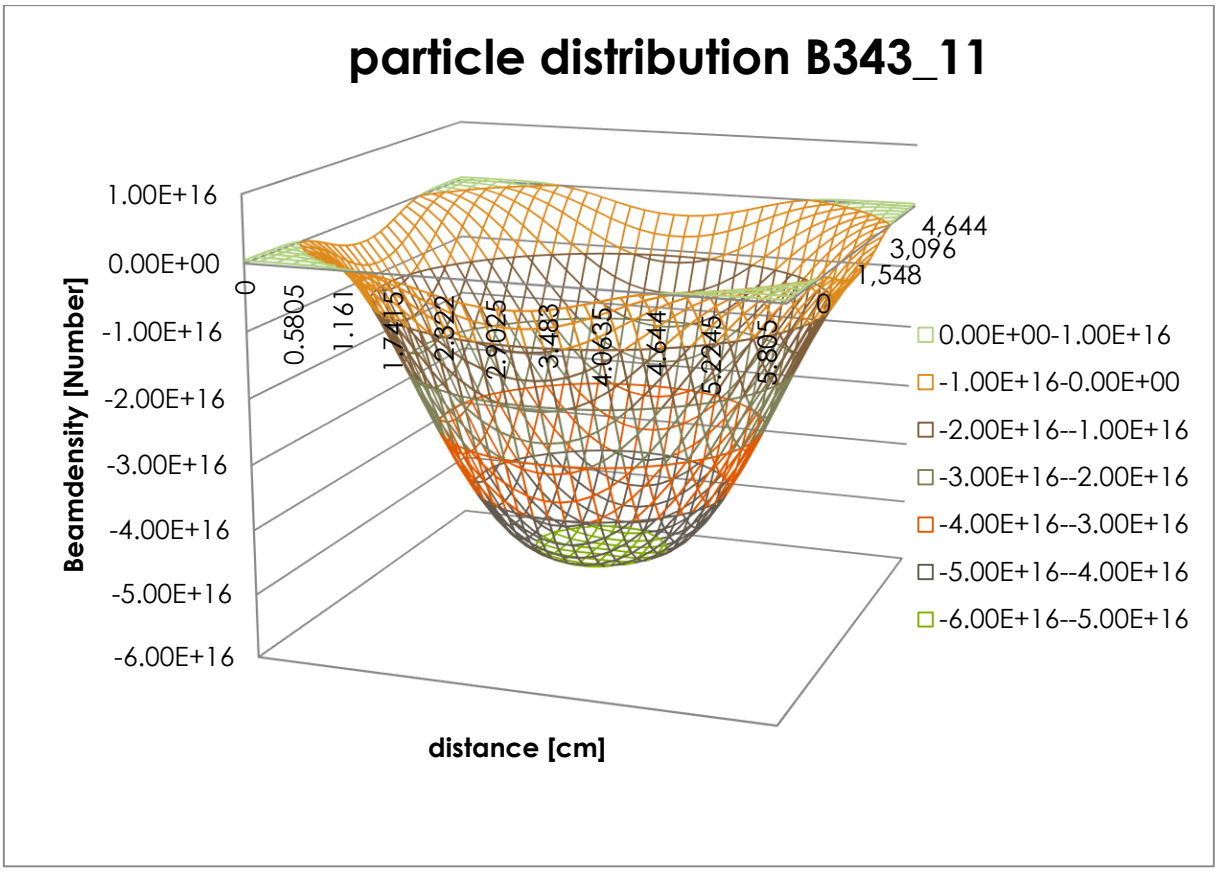

Figure 93: Distribution of sputtered particles (calculation experiment B343_11) on the target surface

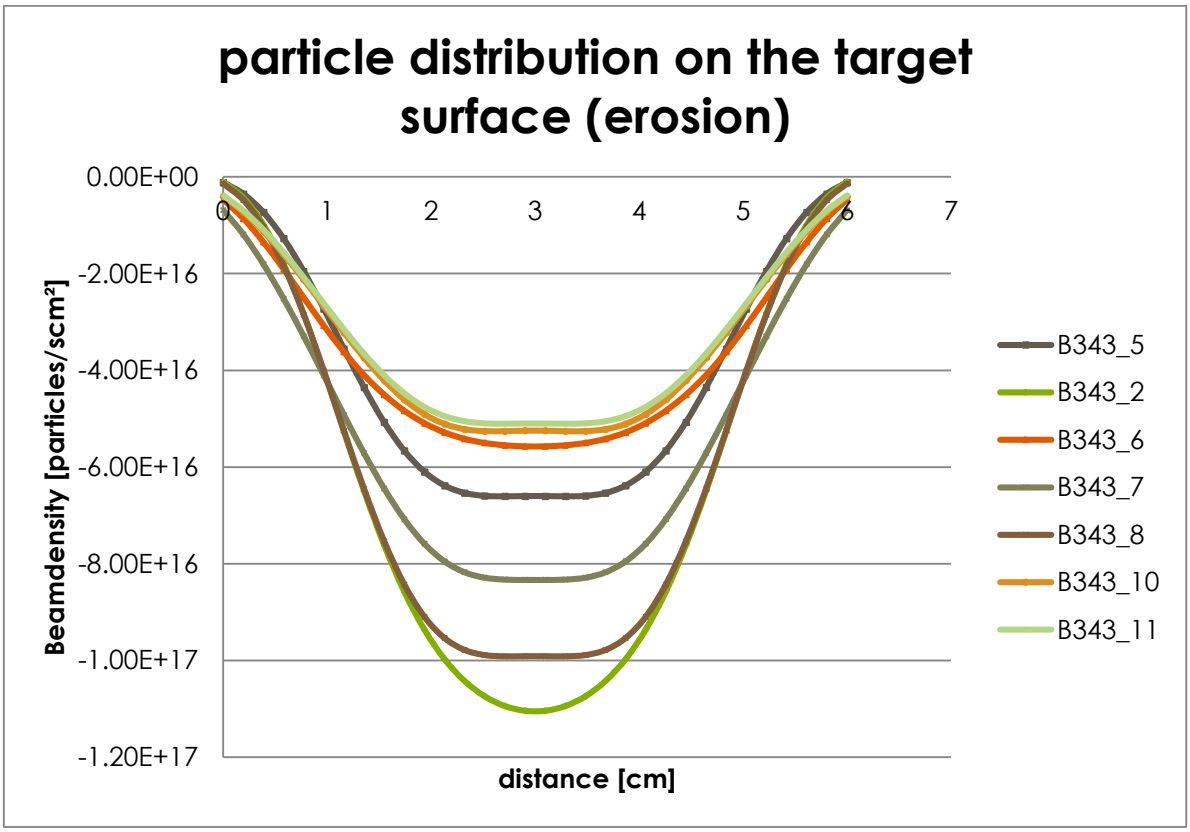

Figure 94: Comparison of the sputtered particle distribution of all experiments

12 Appendix D: Dependences

The next diagrams show the secondary particle distribution in different distances from the substrate surface on different conducting substrates like silicon, rubber, glass, graphite, metal and PET-PTFE. The same results were obtained for the particle power density on the surface and in different distances to the substrate.

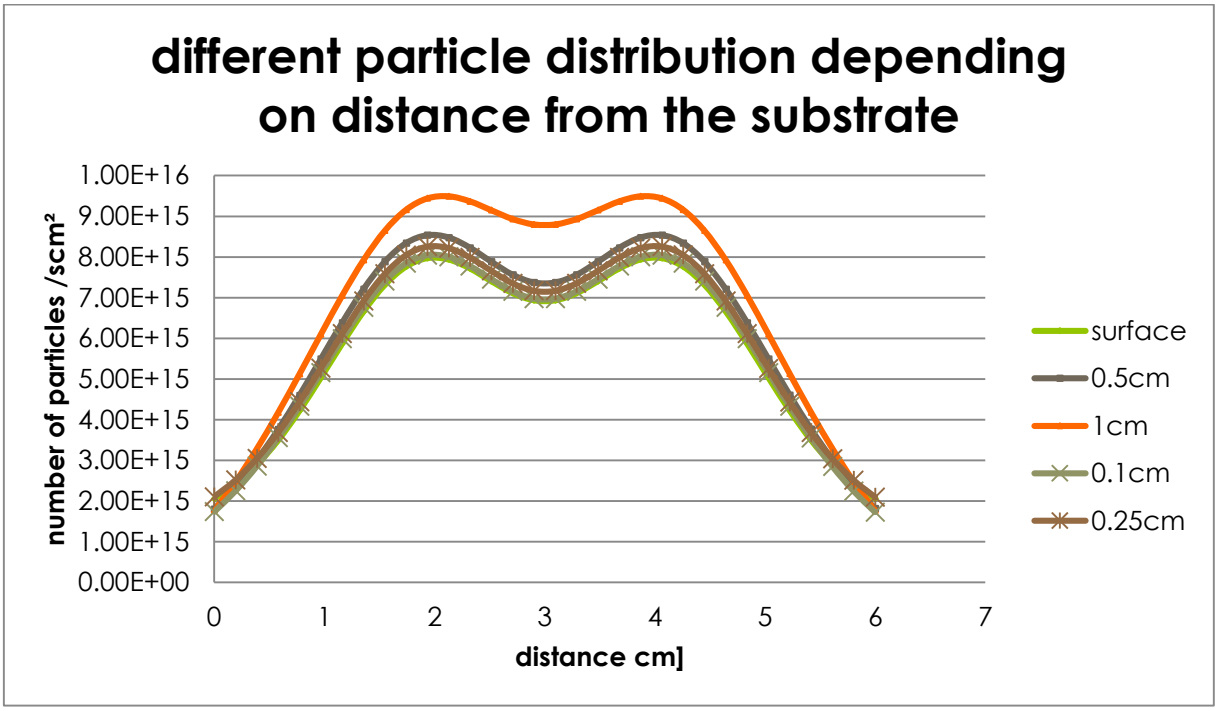

Figure 95: Particle distribution at different distances from a glass substrate.

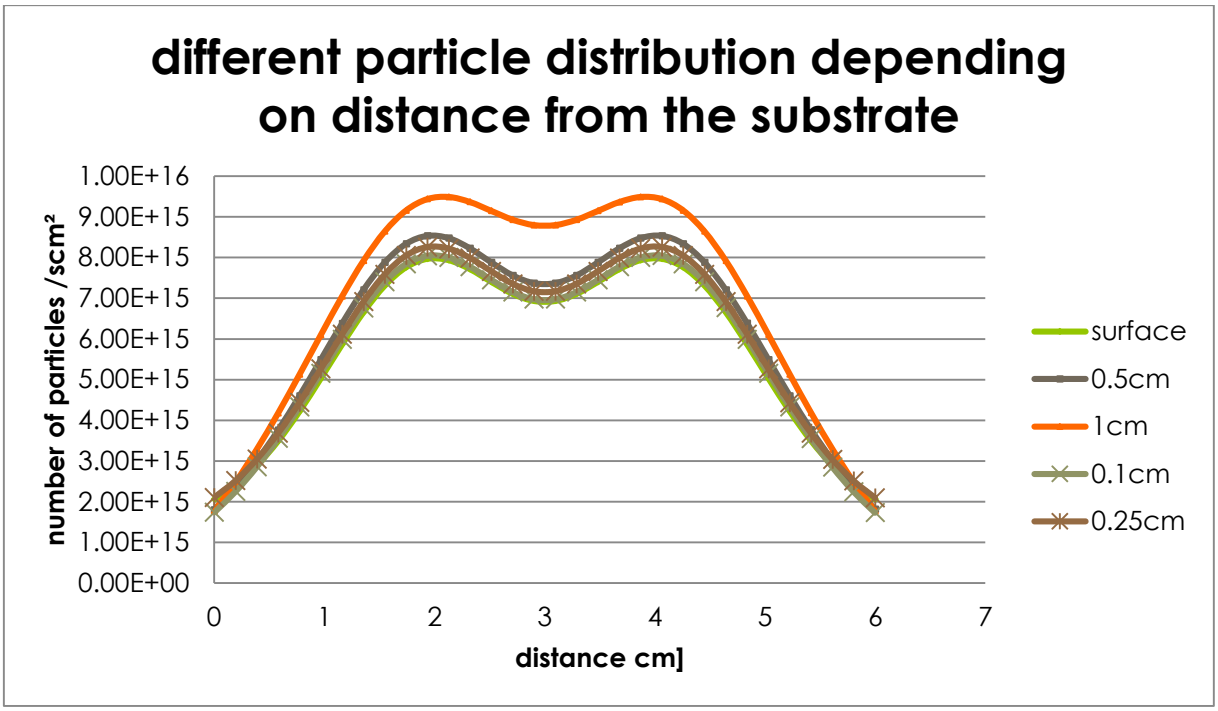

Figure 96: Particle distribution depending on the distance from the substrate which is silicon

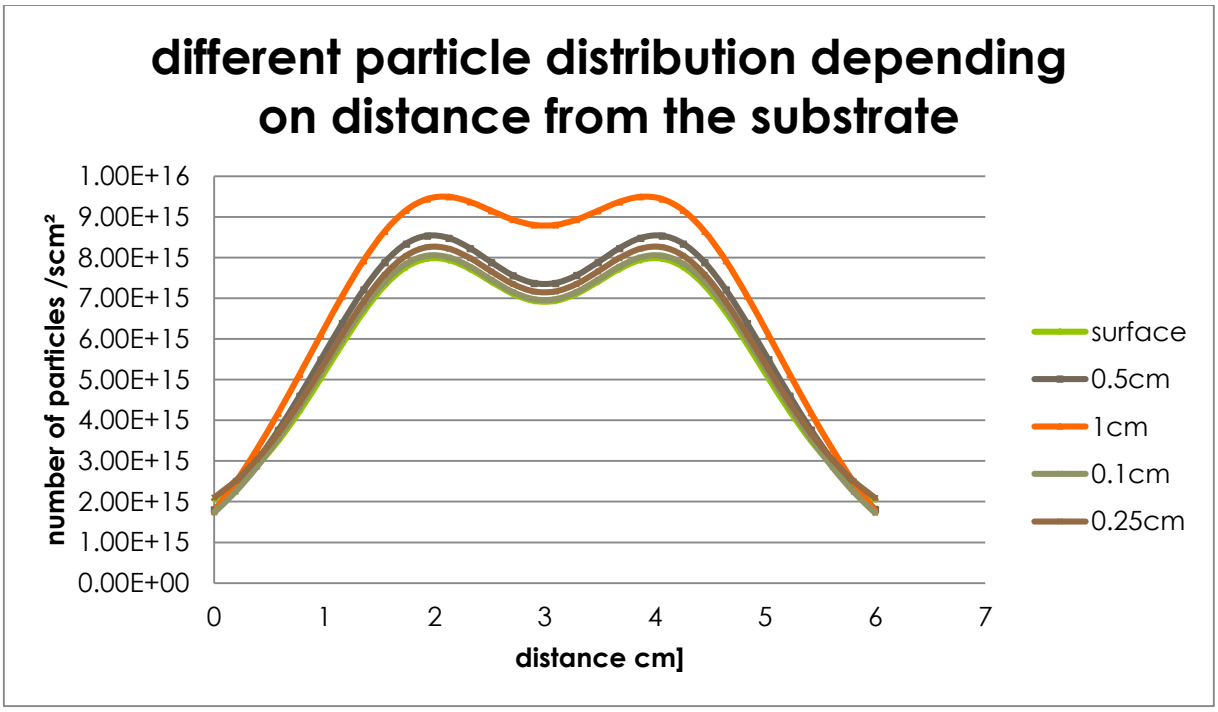

Figure 97: Particle distribution depending on the distance from the substrate which is graphite

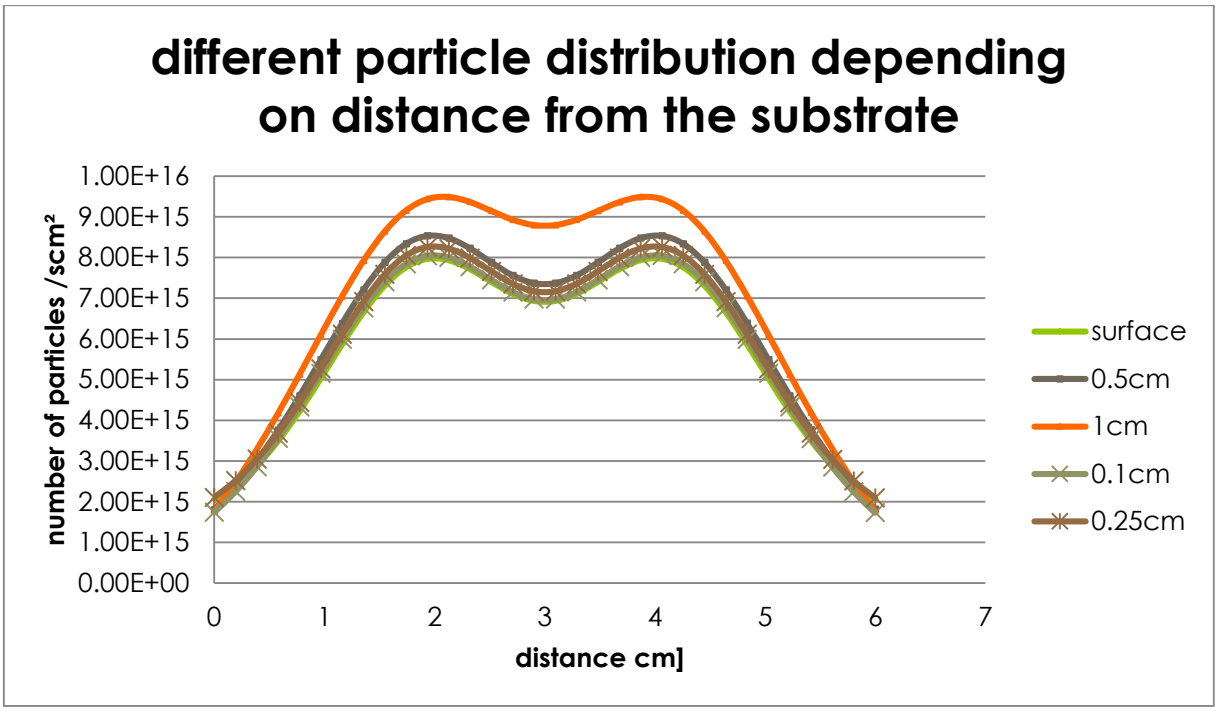

Figure 98: Particle distribution depending on the distance from the substrate which is rubber

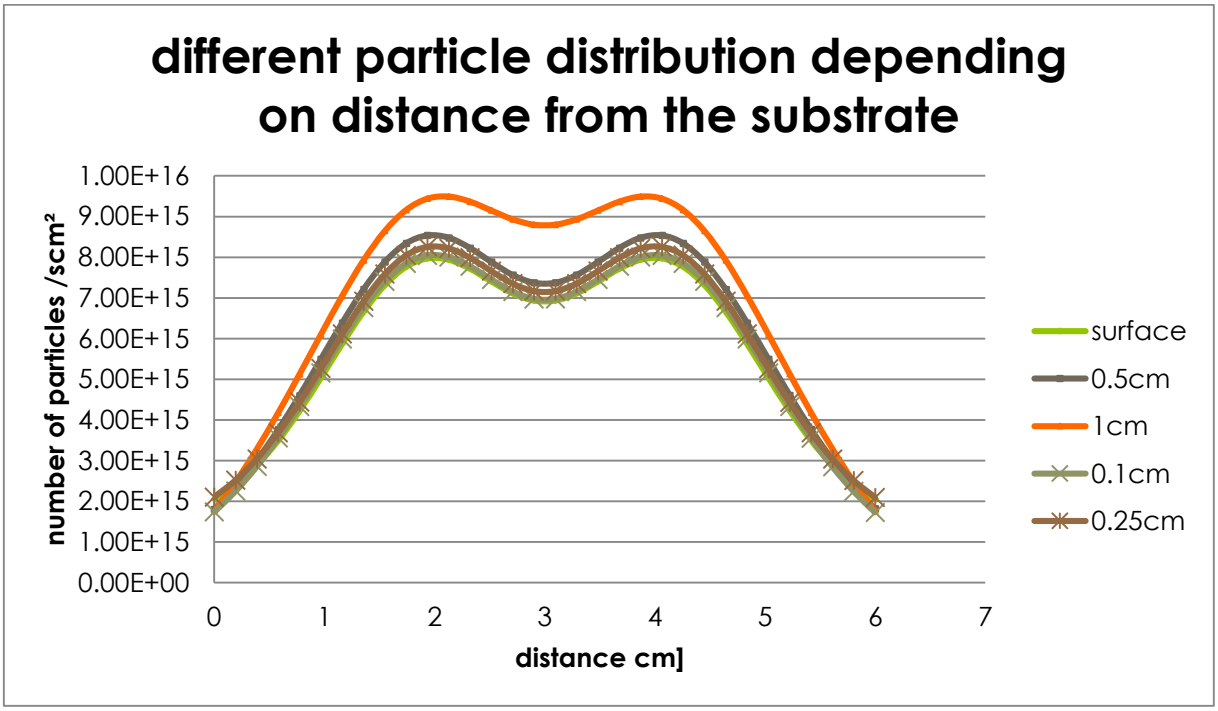

Figure 99: Different particle distribution depending on the distance from the substrate which is metal

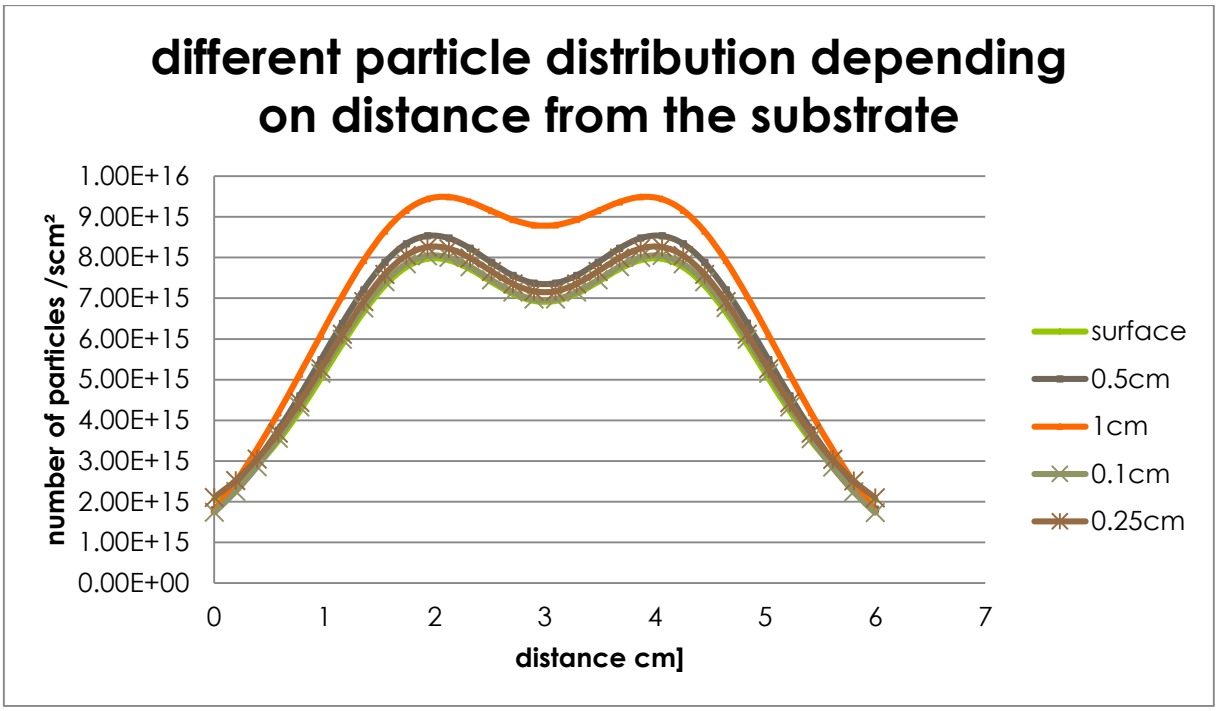

Figure 100: Different particle distribution depending on the distance from the substrate which is PET-PTFE

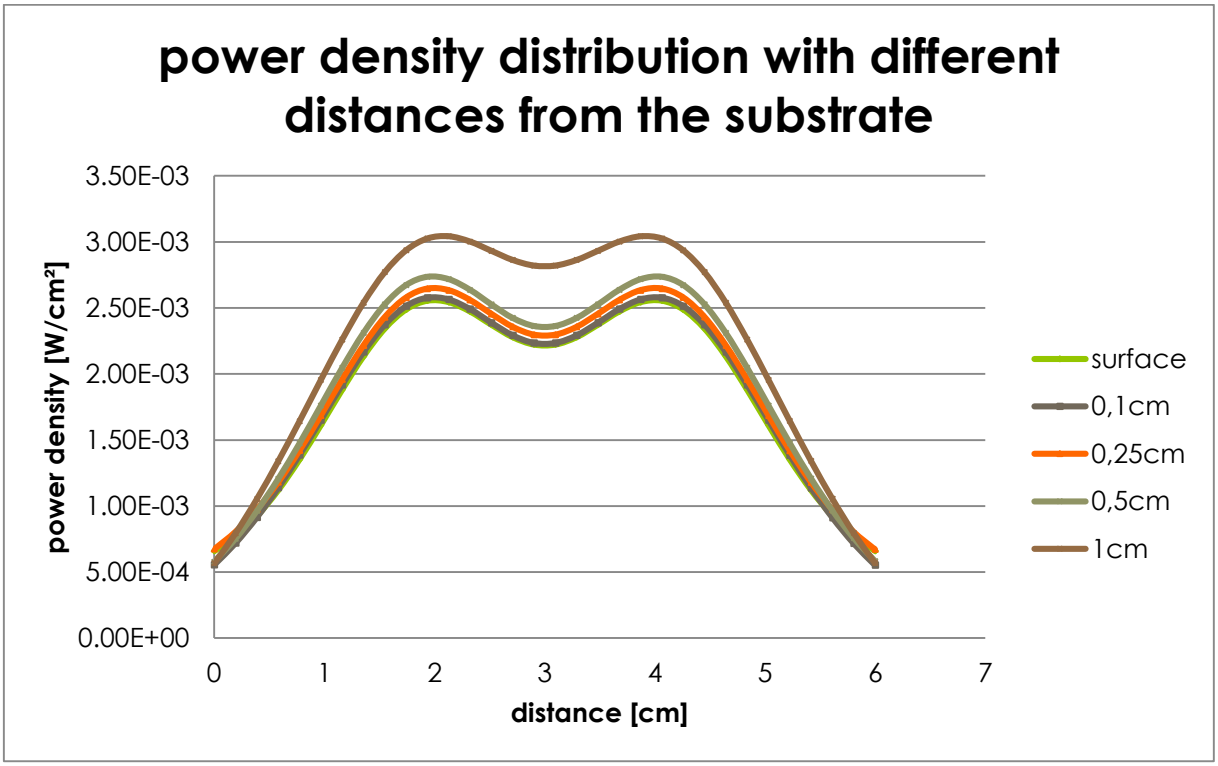

Figure 101: Power density distribution at different distances from the substrate.